Microstructural development and stability in CNT/Ni composites processed by high pressure torsion

Dissertation

zur Erlangung des Grades

des Doktors der Ingenieurwissenschaften

der Naturwissenschaftlich-Technischen Fakultät

der Universität des Saarlandes

Von

Katherine Aristizabal Alvarez

Saarbrücken

2020

Microstructural development and stability in CNT/Ni composites processed by high pressure torsion

Tag des Kolloquiums: 17.06.2020

Dekan: Prof. Dr. Gregor Jung

Berichterstatter: Prof. Dr.-Ing. Frank Mücklich

Prof. Dr. mont. Christian Motz

Vorsitz: Prof. Dr. Martin Müser

Akad. Mitarbeiter: Dr.-Ing. Shiqi Fang

"Curiosity has its own reason for existing...

Once you stop learning, you start dying."

Albert Einstein

Table of Contents

Abstract

In order to overcome the thermal instability in nano-crystalline (NC) and ultrafine-grained (UFG) materials due to a large grain boundary area, the use of reinforcements and alloying elements has been implemented. To this end, multiwall carbon nanotubes (MWCNT) were used in NC and UFG nickel matrix composites (Ni/CNT) processed by severe plastic deformation (SPD) by means of high pressure torsion (HPT). A set of systematic investigations were conducted, aiming to address open questions regarding the microstructural evolution during HPT, the distribution homogenization of CNT, the structural damage induced on the CNT, the strengthening mechanisms and the material performance related to the thermal stability and the tribological behavior.

HPT at room temperature of Ni/CNT composites was found to significantly increase the microstructural inhomogeneity along the radial direction, resulting in the hindrance of the microstructural steady-state. An analytical model to determine the minimum strain for a homogenous distribution of CNT was developed. Results showed that CNT suffer degradation related to the accumulated strain and the variations in composition. Finally, CNT contributed to the microstructural stabilization and improved the wear behavior with respect to the reference material (SPD Ni).

Zusammenfassung

Um die thermische Instabilität bei nanokristallinen (NC) und ultrafeinkörnigen (UFG) Materialien aufgrund einer großen Korngrenzenfläche zu überwinden, wurde der Einsatz von Verstärkungs- und Legierungselementen eingeführt. Zu diesem Zweck wurden mehrwandige Kohlenstoff-Nanoröhrchen (MWCNT) in NC- und UFG-Nickelmatrix-Verbundwerkstoffen (Ni/CNT) eingesetzt, die durch starke plastische Verformung (SPD) mittels Hochdrucktorsion (HPT) verarbeitet wurden. Es wurden eine Reihe systematischer Untersuchungen durchgeführt, um offene Fragen zu beantworten. Speziell wurden Mikrostrukturentwicklung, Verteilung der CNT, strukturelle Schädigung der CNT, Verstärkungsmechanismen und das Materialverhalten im Zusammenhang mit der thermischen Stabilität und dem tribologischen Verhalten untersucht.

Es wurde festgestellt, dass HPT bei Raumtemperatur von Ni/CNT-Verbundwerkstoffen die mikrostrukturelle Inhomogenität entlang der radialen Richtung signifikant erhöht, was zu einer Behinderung des mikrostrukturellen stationären Zustands führt. Zusätzlich wurde ein analytisches Modell zur Bestimmung der notwendigen Mindestdehnung für eine homogene Verteilung von CNT entwickelt. Zudem wurde beobachtet, dass CNT im Zusammenhang mit der akkumulierten Dehnung und den Variationen in der Zusammensetzung eine Schädigung erfahren. Schließlich trugen die CNT zur Stabilisierung gegen

Kornwachstum und zu einem verbesserten Verschleißverhalten gegenüber dem Referenzmaterial (SPD Ni) bei.

Acknowledgements

Among the many people that contributed in one way or another to the development of my thesis, I would like to give special acknowledgement to my colleague Dr. Sebastián Suárez for all his support, scientific contribution and life lessons. It has been a great experience having you as group leader. To my thesis advisor Prof. Dr. Ing. Frank Mücklich, for giving me the opportunity of working at his institute, where I have learned so many important lessons, which helped me grow not only as a scientist but also as a person. To Dr. Flavio Soldera, for the opportunity to work within the framework of the European School of Materials (DocMASE).

I would like to thank my collaborators Dr. Andrea Bachmaier and Dipl. Ing. Andreas Katzensteiner from the ESI, as well as Prof. Matteo Leoni from the University of Trento, for their valuable contribution. I also thank my scientific

supervisor Prof. Dr. Christian Motz, head of Chair of Material Science and Methods, for his continuous support in all matters related to the development of my work and for reviewing my thesis.

To all my colleagues at FUWE, who have made my time at the institute and outside work very enjoyable. I am especially thankful to the "coffee society" ☺ and to those who have contributed with valuable discussion and for reading some of my work.

Lastly, and most importantly, I am grateful to my family for their love, prayers and unconditional support. I am especially, and forever grateful to my husband Diego for his selfless support, for taking care of me and for being a pair of helpful hands when I needed assistance☺. I love you.

Abbreviations and symbols

a-C	Amorphous carbon
AFM	Atomic force microscopy
a-G	Amorphous graphite
APT	Atom probe tomography
ARB	Accumulative roll bonding
ARC	Arc discharge
b	Absolute value of Burgers vector
BCC	Body centered cubic
CNP	Carbon nanoparticles
CNT	Carbon nanotubes
COF	Coefficient of friction
CPS	Cold pressed sintering
CTE	Coefficient of thermal expansion
CVD	Chemical vapor deposition
D	Grain size
D_C	Critical grain size
D-band	A Raman mode
DSC	Differential scanning calorimetry
DWCNT	Double-wall carbon nanotubes
ε	Root mean square microstrain

EBSD	Electron backscattered diffraction
ECAP	Equal channel angular pressing
EG	Ethylene glycol
ε_{VM}	Von Mises equivalent strain
fcc	Face centered cubic
FWHM	Full width at half maximum
γ	Shear strain
G	Shear modulus
GB	Grain boundary/ies
G-band	A Raman mode
G'-band	A Raman mode
GND	Geometrically necessary dislocations
HAGB	High angle grain boundaries
HPT	High pressure torsion
HRTEM	High-resolution transmission electron microscopy
HUP	Hot uniaxial pressing
I_D	Intensity D-band
I_G	Intensity G-band
$I_{G'}$	Intensity of G'-band
k	Arithmetic average of 1 and (1-ν)
LAGB	Low angle grain boundaries
LPA	Line profile analysis

LSR	Laser-evaporation or laser-ablation
MMC	Metal matrix composites
MWCNT	Multi-wall carbon nanotubes
ν	Poisson ratio
NC	Nanocrystalline materials
NC-graphite	Nanocrystalline graphite
θ	Rotation angle
Q	Activation energy
ρ	Dislocation density
r	Radius or distance from sample' center
RBM	Radial breathing mode
SEM	Scanning electron microscopy
SFE	Stacking fault energy
SPD	Severe plastic deformation
STM	Scanning tunneling microscopy
SWCNT	Single-wall carbon nanotube
T	Number of turns
t	Thickness
ta-C	Tetragonal amorphous carbon
TEM	Transmission electron microscopy
TIMs	Thermal interface materials
TK	Tuinstra and Koenig

T_m	Melting temperature
T_p	Peak temperature
TSW	Thrower-Stone-Wales defects
UFG	Ultrafine-grained materials
V	Heating rate
WPPM	Whole powder pattern modelling
XPS	X-ray photoelectron spectroscopy

1. Introduction and Motivation

Ultrafine-grained (UFG) and nanocrystalline (NC) materials usually possess **improved mechanical properties** compared to their coarse grained counterparts. These materials can be obtained not only by traditional bottom-up methods (i.e. electrodeposition, inert gas condensation, chemical and physical deposition among others), but also by top-down techniques, using coarse-grained bulk polycrystalline solids as starting material [1]. Top-down techniques consist of exerting large shear strains inducing severe plastic deformation (SPD) without significantly changing the sample shape.

Notwithstanding the unique physical and mechanical properties in **SPD materials**, they possess a non-equilibrium nature that makes them **thermally unstable**, implying grain growth at low temperatures, which is detrimental for their mechanical performance [2]. In this regard, efforts have been done seeking the stabilization of the microstructure by the addition of reinforcing particles and introduction of oxides [3,4] and alloying elements [5].

Carbon nanotubes **(CNT)** are suited to be used as reinforcement phase in composite materials due to their **outstanding physical properties** (i.e. high thermal conductivity), high specific strength (strength/density), low weight and high aspect ratio. In particular, the use of CNT in MMC can improve electrical, thermal and mechanical properties (Al [6–13], Cu [14–16] and Ni [17–20]).

Recently, CNT were used in composites subjected to severe plastic deformation [21] seeking thermal stabilization of the microstructure. This is related to their ability to pin the grain boundaries (GB) (in coarse-grained materials) when the material is heated, which enables the control of the final microstructure [22] and the mechanical properties [23]. Nevertheless, CNT tend to agglomerate due to strong van der Waals interactions.

High Pressure Torsion (HPT) is an ideal technique to study materials subjected to very large strains and offers the possibility to obtain bulk composites with **uniform second phase distribution** [24], which is of great importance to improve the ductility and to reduce, to a certain degree, the anisotropic behavior during mechanical loading of metal matrix composites (MMC). In this regard, **processing CNT/MMC by HPT represents a possibility not only of stronger and finer microstructures but also of a better distribution homogenization of the CNT within the matrix**.

Nevertheless, the CNT must conserve their microstructural features after processing, in order to retain to some extent their physical properties and to avoid chemical interactions with the metallic matrix, which can be detrimental for the mechanical performance. **Raman spectroscopy** has proven to be a powerful instrument for the characterization of carbon based materials and even though there are numerous reports on the damage analysis of CNT by means of Raman spectroscopy, **by the time of the preparation of the present**

dissertation, there was no thorough study in the literature on the CNT structural state after SPD and in many cases the analysis was limited to the evaluation of the so-called defect index (I_D/I_G) [21,25,26].

In summary, processing CNT/MMC by HPT could lead to composites with microstructures having improved mechanical properties **provided that the CNT are well distributed within the matrix and retain their structural integrity** in order to properly being able to stabilize the microstructure against thermally-activated grain growth.

The present dissertation deals with the processing of CNT/Ni composites by HPT. Several important aspects are addressed in order to understand the limits within which, these composites should be processed by HPT. Specifically, the following aspects are discussed: the structural evolution, the damage suffered by the CNT, the distribution homogeneity of the reinforcement, the composites' performance under heating and tribological testing as well as the strengthening mechanisms involved.

2. State of the art

2.1. Carbon Nanotubes (CNT)

Carbon nanotubes (CNT) are synthetic carbon allotropes, which can be thought of as graphene sheets rolled up into tubes with un/capped ends. Since their discovery in 1991 by Ijima [27], they have been widely used and proposed for a great span of engineering applications due to their outstanding mechanical, thermal and electrical properties (mainly along the tubes' axial direction). Carbon nanotubes possess a sp^2-hybridization, in which the carbon atoms form σ-bonds with other three other carbon atoms (see Fig. 1a), whose bonds are oriented 120° from one another, and form a set of hexagonal structures (see Fig. 1b). Moreover, orthogonal p orbitals form π-bonds (see Fig. 1a), which are free delocalized electrons and are highly mobile along the planar direction [28]. Fig. 2 shows some representative sp^2 hybridized materials. In contrast, for sp^3-hybridization, the σ-bonds are oriented 109.5° from one another (see Fig. 1c).
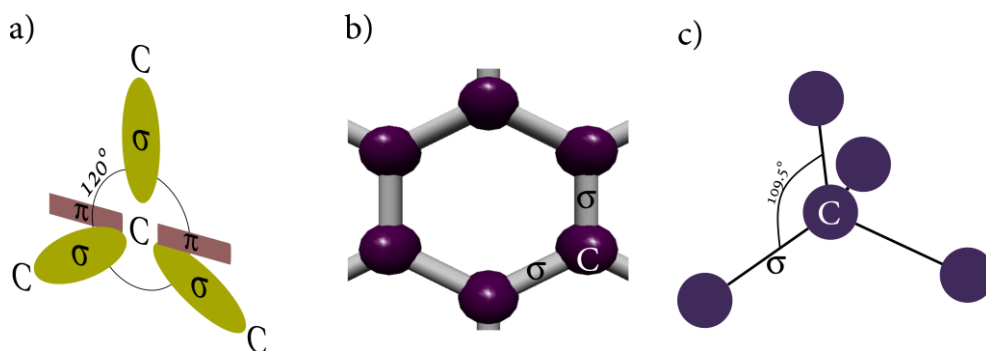

Fig. 1 a) Bonding structure of sp^2 hybridized materials showing the configuration of both σ and π bonds, b) hexagonal carbon ring and c) sp^3 diamond structure.

0D : Buckyball 1D : Nanotube

2D : Graphene Sheet 3D : Graphite
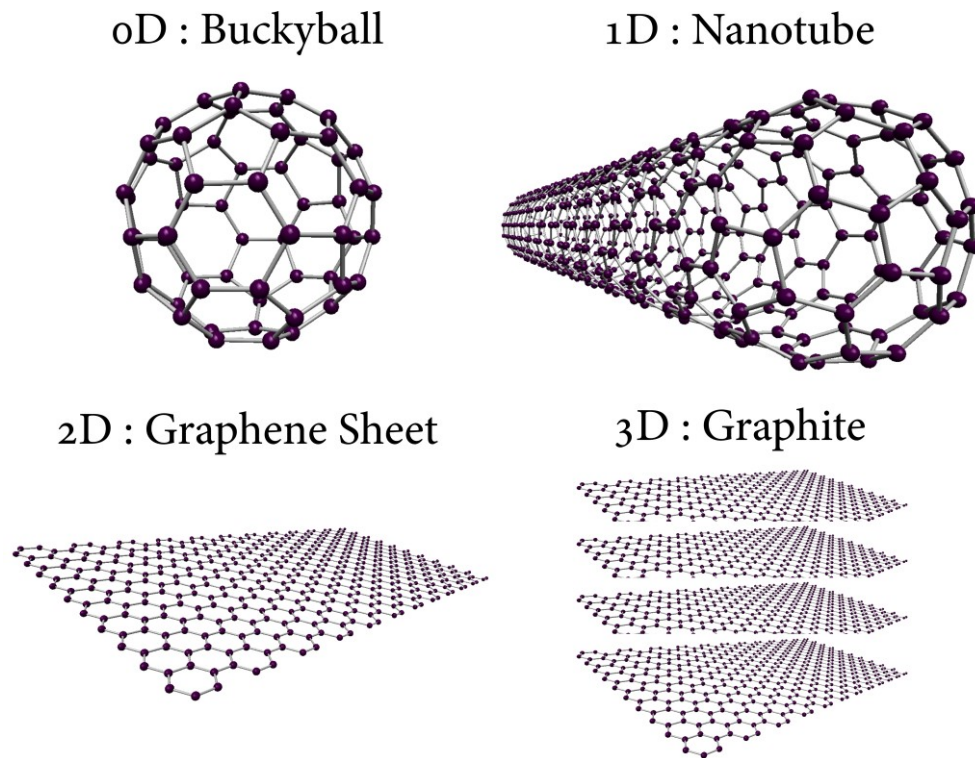
Fig. 2 Main carbon sp² hybridized nanomaterials.

CNT can have one, two or more rolled-up graphene sheets to form a single wall CNT (SWCNT), a double-wall CNT (DWCNT) or a multi-wall CNT (MWCNT). The separation of the concentric tubes in a MWCNT ranges between 0.32-0.35 Å, similar to the interplanar separation of graphite (0.34 Å) [29]. Moreover, MWCNT are significantly heavier than SWCNT, which makes the mass production of SWCNT more arduous compared to MWCNT.

Furthermore, the physical properties of CNT are affected by the presence of structural defects and impurities stemming from the synthesis process or appearing during post-processing steps. Common defects can be vacancies, di-

vacancies (missing carbon atoms), polygonal distortions such as pentagons, heptagons, etc., and bond rotations (the so-called Thrower-Stone-Wales (TSW) defects [30,31]), which give curvature to the CNT reducing the strain energy. Some of these defects are shown in Fig. 3. Moreover, non-carbon atoms (e.g. Ni and B) can be embedded in the lattice, and non-sp^2 carbon defects can be present due to dangling bonds, carbon chains, interstitials, open-ended tubes, which increase the CNT reactivity [32].

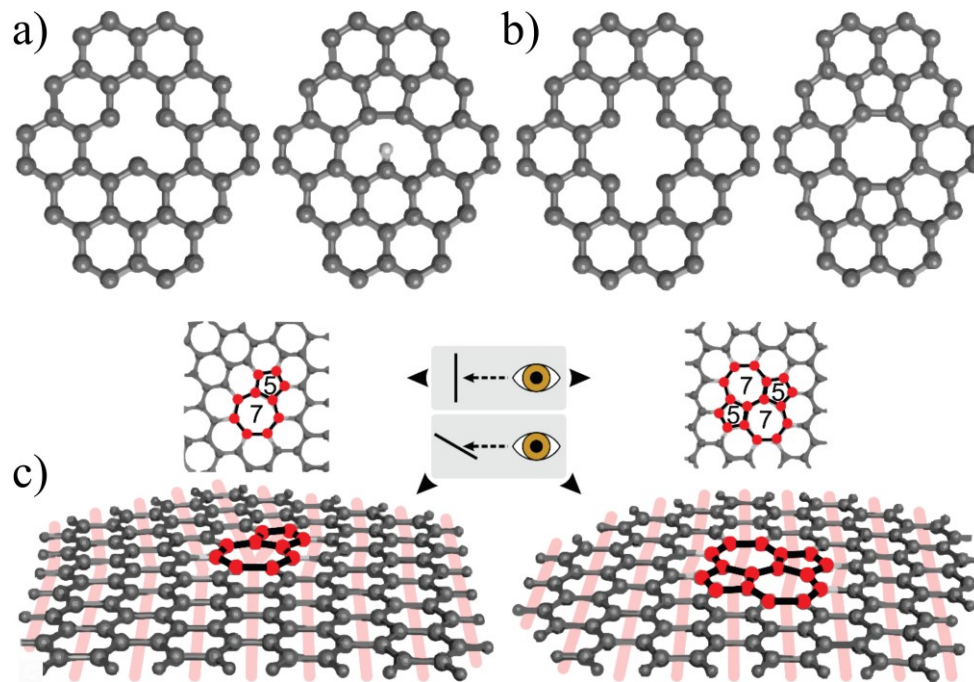**Fig. 3 Some defects present in CNT. a) Mono-vacancy (left) and reconstruction showing a dangling bond with an H–termination (right), b) di-vacancy (left) and respective reconstruction (right), c) single 5-7 defect and a 5-7-7-5 TSW configuration and respective perpendicular views showing the nucleation of a dislocation in the former and the absence of long-range disorder in the latter [33].**

2.1.1. Physical properties of CNT

SWCNT can be metallic, semi-metallic and semi-conducting, depending on how the sides of the honeycomb lattice structure are joined together (chirality). MWCNT, on the other hand, possess an arbitrary number of concentric sheets with different chiralities and have been found to be always metallic, but possess a decreased electronic coupling between the layers relative to graphite mainly due to the interplanar stacking disorder [34,35].

According to theoretical simulations and experimental studies, thermal conductivity of individual tubes in the case of SWCNT can be as high as 6600 W/m·K and in MWCNT, as high as 3000 W/m·K [36,37]. Nevertheless, CNT thermal conductivity strongly depends on the structure and morphology [38]. Furthermore, CNT have a strong tendency to agglomerate due to attractive van der Waals forces, which makes their alignment in CNT composites a challenging task. Entanglement of CNT in composites increases the heat diffusion (with increasing CNT-CNT contact) and involves simpler manufacture techniques. However, it is detrimental for the thermal conductivity, which can limit certain applications in which a remarkably high thermal conductivity (avoidance of CNT-CNT contact) is required as in thermal interface materials (TIMs) [38].

CNT microstructural characteristics differ significantly from those of crystalline solids and, since there is no spatial uniformity of the material in the radial direction, CNT response to applied stresses and fracture behavior diverge

significantly in the axial and radial direction. CNT are significantly stiff in the axial direction but are also flexible and can undergo large nonlinear deformations [39]. Despite the technical difficulties regarding the manipulation of CNT for their mechanical testing, the measurement of the mechanical properties and fracture of CNT has been a very attractive topic in the scientific community. Regarding tensile strength and Young's modulus, the experimentally determined values vary significantly depending on factors such as the type of CNT (SWCNT or MWCNT), the number of walls and the amount of structural defects. Table 1 shows some experimentally obtained values on the tensile strength and Young's modulus of CNT.

Table 1. Tensile strength and Young's modulus for different CNT. Adapted from [40].

Tensile Strength in TPa	Young's modulus in TPa	Type	Method used	References
	1.8	$MWCNT_{ARC}$	Thermal vibrations (TEM)	[41]
	1.25	$SWCNT_{LSR}$	Thermal vibrations (TEM)	[42]
	1.28	$MWCNT_{ARC}$	AFM	[43]
	0.81	$MWCNT_{ARC}$	AFM	[44]
	0.01-0.05	$MWCNT_{CVD}$	AFM	[45]
0.01-0.06	0.27-0.95	$MWCNT_{ARC}$	AFM (dual cantilevers)	[13]
0.15	0.8	$MWCNT_{ARC}$	TEM (tension)	[46]

Owing to their outstanding physical properties, CNT have been used as reinforcement phase in CNT composites, as will be discussed in chapter 2.2.2. In the present dissertation, MWCNT were used as reinforcement material in metal matrix composites (MMC), mainly because the presence of multiple walls in CNT composites is of advantage, since it enables the possibility to functionalize the CNT for a more efficient load transfer and to sacrifice some layers during mechanical processing, while retaining the integrity of the inner tubes.

Furthermore, MWCNT have been extensively used for anti-wear enhancement and friction reduction due to their intrinsic lubrication properties. In this regard, many studies have been conducted on the tribological behavior of CNT-reinforced MMC (Al, Cu, Cr, Mg and Ni/CNT [47–57]). The reduction in the steady state coefficient of friction (COF) has been attributed to CNT being continuously provided to the contact zone where they can roll and slide [49], but also to the formation of a lubricating carbon film on the surface as a result of CNT degradation [50,51]. In recent work performed by Reinert et al., the tribo-mechanisms of CNT in CNT/Ni matrix composites and CNT-coated bulk Ni were compared [58]. In the coating, it was observed that the decrease in COF holds, provided that the CNT are present at the contact zone and the COF increased after the coating is removed. In the composites, on the other hand, the COF reduction was attributed to a continuous supply of CNT to the contact zone. Additionally, when the CNT coatings were combined with laser patterned surfaces they showed a long-lasting solid lubrication because the laser textures

served as lubricant reservoirs entrapping CNT, which can be provided to the contact zone [59]. Furthermore, the surface lubrication mechanism of CNT was attributed to the compression and elastic restoration of CNT agglomerates and their continuous supply to the contact area and tribologically induced CNT degradation with the formation of nanocrystalline graphite allowing the incoming CNT to slide and roll on the graphitic surfaces [60].

2.1.2. Structural Characterization of CNT

There are multiple techniques by which the CNT microstructure and properties can be characterized [61], the most common being electron microscopy (SEM, TEM, HRTEM, etc.), atomic force microscopy (AFM), scanning tunneling microscopy (STM), X-ray photoelectron spectroscopy (XPS) and Raman spectroscopy [62]. The latter is the fastest and most user-friendly technique for the characterization of sp^2-hybridized carbon nano-materials, as well as it is accurate and reliable. It does not require laborious sample preparation (non-destructive), enables to differentiate among the present phases (and polymorphism) and to detect and estimate defects and impurities by analyzing the different Raman modes.

Raman spectroscopy relies on the optical properties of CNT, specifically, the van Hove singularities [31,63]. If the excitation energy (energy of incident photons) matches a van Hove singularity in the electronic joint density of states of the valence and conduction bands, optical transitions can be seen experimentally

(inelastic light scattering along with a change in vibrational energy of a molecule) as up- or downshifts of emission frequency after relaxation. These are the so-called Stokes (down) and anti-Stokes (up), which complement the Rayleigh, i.e. elastic scattering. Thus, not only phonons are involved in Raman scattering, but also, magnons and plasmons can be involved in a scattering process satisfying the energy-momentum conservation [63]. Accordingly, a Raman spectrum consists of a plot of intensity of Raman scattered light versus the Raman shift (frequency difference from the incident radiation).

The G-band (around 1580 cm^{-1}) and the radial breathing mode (RBM) (about 100-500 cm^{-1}) are first-order Raman modes (involving one-phonon emission). The G-band, is related to the in-plane vibrations along the tangential direction and indicates the presence of sp^2 carbon networks, and the RBM (bond-stretching out-of-plane phonon mode) is a characteristic feature, mostly present in SWCNT, related to the coherent movement of carbon atoms in the radial direction with a certain frequency (Raman shift) inversely proportional to the tube diameter [63]. Moreover, the G-band full width at half maximum (FWHM) can be related to the CNT structural crystallinity. The D-band (~ 1350 cm^{-1}), which stems from the disorder-induced mode, and its second harmonic, the G'-band (~ 2700 cm^{-1}), are the strongest second-order Raman modes. As the G'-band is less sensitive to defects in CNT, the ratio $I_{G'}/I_D$ can be used as purity index [64]. Fig. 4 shows the different characteristic Raman modes of a sample of pristine MWCNT synthetized by chemical vapor deposition (CVD).
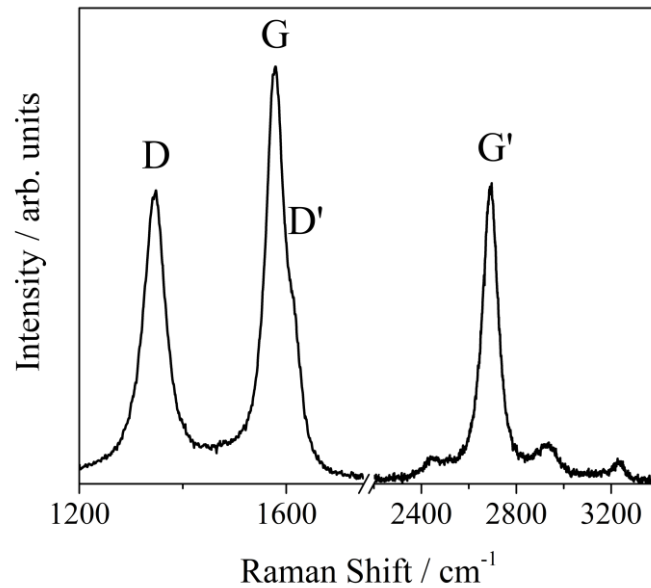
Fig. 4 Raman spectrum of a pristine MWCNT sample synthetized by CVD, showing the characteristic peaks. The excitation wavelength used was 532 nm (2.33 eV).

The D-band arises from aromatic rings [65] and its intensity ratio with the G-band (i.e. defect index I_D/I_G) increases with increasing disorder and is inversely proportional to the domain size L_a (related to the defect-to-defect distance), as studied by Tuinstra and Koenig (TK) by X-ray diffraction experiments in graphitic structures [66]. Nevertheless, ordering in the case of amorphous carbons is accompanied by the development of a D-band (the opposite of disorder in graphite), and therefore the TK relation will no longer hold (transition from graphite to amorphous graphite (a-G)) and thus the intensity I_D/I_G ratio will decrease [65].

Raman spectroscopy using monochromatic visible light excitation (typically from a laser) is an optimal technique for the study of sp^2 hybridized materials. Based on calculations by Loudon [67] and on experimental results by S.R. Sails et al. [68], sp^2 domains with the characteristic π-bonds are up to 233 times more sensitive to visible light than sp^3, and higher photon energy would be necessary to excite both the π and σ-bonds (UV light, 5.1 eV) in contrast to, for example, green light (~2.33-2.41 eV) [69].

Accordingly, visible Raman spectrum provides mainly direct information about sp^2 ordering and indirect estimation of sp^3. Based on the competing features in a Raman spectrum, Ferrari and Robertson [65] defined an *amorphization trajectory* ranging from graphite (0% sp^3) to ta-C (~ 100% sp^3, tetrahedral amorphous carbon or defective diamond). This *amorphization trajectory* is defined by considering the evolution of the G-band position and the I_D/I_G ratio, and can be used to derive the sp^3 fraction. The shift of the G-band is actually caused by the appearance of another disorder induced peak (D') at around 1620 cm^{-1} (shown in Fig. 5), which merges in the G-band when small domains are present. Table 2 summarizes the features of the *amorphization trajectory* for Raman data at 514 nm.
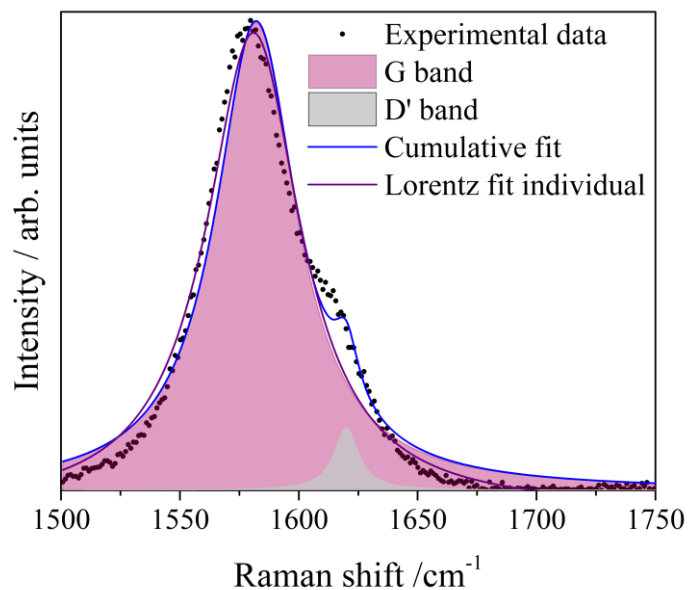
Fig. 5 Deconvolution of the G-band showing the cumulative fit and the individual Lorentz fit.

Table 2. Summary of variation of the G-band position and I_D/I_G ratio.

	Stage 1	Stage 2	Stage 3
G position in cm^{-1}	(+) 1581 → ~ 1600	(-) ~ 1600 → ~ 1510	(+) ~ 1510 → ~ 1570
I_D/I_G	(+) 0 → ~ 2 Follows TK [66]	(-) ~ 2 → ~ 0 TK no longer valid	Very low or 0

Graphite
0% sp³   **NC-graphite**
0% sp³   **a-C**
~ 20% sp³   **ta-C 85% sp³**

In summary, the characteristic features of the Raman spectra of CNT enable the study of their purity ($I_{G'}/I_D$) and defective state (I_D/I_G, G-band shift and FWHM) [64,65,70].

According to the information discussed in the present chapter, *Raman spectroscopy* constitutes a key technique for the study of structural defects in carbon nanomaterials, and was therefore extensively used in the present dissertation.

2.2. Metal Matrix Composites (MMC)

Composite materials are engineering materials consisting of two or more physically distinguishable components that are completely insoluble in each other. Composites possess improved functional and/or physical properties than their individual components separately and usually possess a lower density, allowing for a higher specific strength. They are composed by a matrix, a reinforcement and the interface between them, which enables the interaction (e.g. load transfer) between the components. The matrix can be of ceramic, polymeric or metallic nature and the reinforcement can be particles or fibers (continuous, short or whiskers) [71,72].

MMC are typically reinforced by ceramic particles or ceramic fibers (e.g. oxides, carbides, nitrides, etc.). The matrix is selected according to the application and final characteristics required in the composite. Moreover, the performance and characteristics of the composites depend not only on the reinforcement volume fraction, composition, size, distribution and orientation, but also on its chemical composition and physical properties, as well as on the processing history of the composite (e.g. fabrication method, cold work, heat treatment, etc.).

MMC are traditionally known to be composed by a metallic matrix and a non-metallic reinforcement, whereas classical alloys, consisting of two phases obtained from the melt by solidification are normally not considered a composite [73]. However, some authors have considered these two-phase alloys and the

severely deformed counterparts as metal-metal nano/composites [74]. In line with the classical definition, in the present dissertation, relevant discussion about MMC is focused on particulate reinforced MMC, with special attention to carbon nanotubes.

2.2.1. Fabrication methods of MMC

The fabrication method is to be chosen depending on the characteristics of both the matrix and the reinforcement, as well as on the required final performance and shape of the composite. MMC thus can be manufactured by a wide variety of processing methods such as liquid metal, deposition and solid state processes [75–77]. Relevant for the present dissertation are solid state methods of particulate-reinforced composites, in which adverse and interfacial reactions between the components can be avoided, since the processing is performed at temperatures lower than the melting temperature of the matrix. Furthermore, solid state methods allow to tailor the distribution of the reinforcing phase [71], especially critical in the case of CNT-reinforced MMC, in which the CNT tend to agglomerate due to Van der Waals interactions.

Solid state methods are mainly based on **powder metallurgy techniques,** the starting materials consist of metallic powders and powder/particulate reinforcing materials, which are **mixed/blended** and **cold pressed** to form green bodies. The latter can then be uniaxially or isostatically **sintered** and/or **extruded** - **forged** (or other deformation processes) in order to obtain the

maximum densification possible. The main secondary processing methods are discussed in the following.

Mixing/Blending

In the case of carbon nanoparticles (CNP)-reinforced MMC, the mixing/blending process is a very critical step, which will determine the homogeneity of the reinforcement distribution. The three most common methods to mix/blend CNP with metallic powders are **molecular level mixing**, **ball milling** and **colloidal mixing**.

Molecular level mixing involves the functionalization of the CNP, i.e. chemical treatment of the particles (typically acid oxidation [78]), in order to break covalent bonds and thus attach functional groups to the surface (e.g. −OH, -COOH, etc.). These groups will act as nucleation sites for the formation of metal oxides on the surface of the CNP (for example CNT) by mixing the functionalized particles in a solvent with a metal salt and a reducing agent. This solution consisting of metal particles decorated CNT is then calcined in, for instance, hydrogen atmosphere, resulting in metal-encapsulated CNT. By this method, very homogeneous interfaces are obtained. However, damage is introduced to the CNT during the process, which is detrimental for their intrinsic physical properties [52,79,80], and can decrease the performance of the CNT-reinforced MMC.

Ball milling is a technique traditionally used for the secondary grinding step to reduce the size of minerals in the mining industry in order to provide proper particle sizes for the extraction of metals by post-separation techniques. Typically, alumina or steel balls (and/or cylinders) of a certain diameter size distribution are mixed with the solid particles in a cylindrically shaped container (mill). The filling volume of the mill, its rotational speed, the grinding time and the ball/powder ratio should be set as to enable the optimum cascade formation, in which the solid particles are reduced in size by the impact of the hard balls against the solid powder.

Even though this technique is widely used for homogenously distributing CNP with metal powders [79,81–83], as in **molecular level mixing**, **ball milling** introduces defects on the CNT by the energetic impact of the hard balls on the powder mixture. The stress applied on the powder (and MWCNT) during the process can be as high as ~ 30GPa [31].

In **colloidal mixing** the CNT are mixed with the metallic powder in a solvent by means of mechanical and/or ultrasonic agitation. The degree of dispersion depends strongly on the nature of the solvent and the agitation time. The dispersion is then heated as to evaporate the solvent and to obtain a powder, which can be subsequently cold pressed and further processed. Even though, shortening of the CNT can occur if the agitation time is too long [84], in this method, the functionalization of the CNT is not necessary, which removes

unwanted degradation of the CNT during processing. L. Reinert et al. performed the dispersion process by mechanical agitation and ultra-sonication of CNP/Ni powders for the manufacture of CNP-reinforced Ni-MMC for their use as self-lubricating surfaces without significant degradation of the CNP [85]. They used ethylene glycol (EG) as solvent, which had proved to be successful in the manufacture of CNT-reinforced Ni-MMC [86]. S. Suarez et al. [86] studied the dispersion time in ultrasound of MWCNT/EG and found that the sonication should be performed at least during 10 min in order to obtain a proper disentanglement of the CNT without further introducing structural defects.

Colloidal mixing thus is an optimal dispersion technique for the blending of CNT/Metal powder mixtures without performing particle functionalization and without significant degradation of the CNT. Therefore, this method was chosen for the blending step of the CNT-MMC composites used in the present dissertation.

Cold Pressed Sintering (CPS)

During sintering, the porosity of the green bodies is significantly reduced by lattice and GB self-diffusion processes. During these processes, the total interfacial energy is reduced leading to *necking*, *interconnection of pores.*

Complete densification takes place with increasing sintering time until finally only residual *isolated pores* exist [87]. The green pellets are pressureless sintered in a furnace with either vacuum or inert atmosphere to avoid oxidation (see Fig. 6). Nevertheless, due to residual porosity very long sintering times and/or high temperatures have to be used to increase the final density of the composites (for densities greater than ~ 93%) [87].
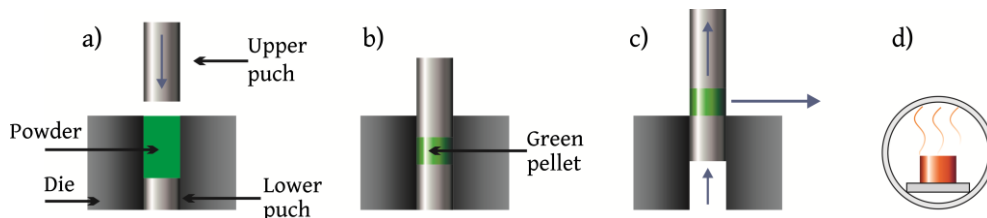

Fig. 6 Schematic of cold pressed sintering (pressureless sintering). a) Die fill stage, b) compaction, c) sample removal and d) sintering.

Hot uniaxial pressing (HUP)

In order to reach high densities in MMC it is necessary to apply external forces, which can promote almost full densification by sintering at lower temperatures and shorter times than in CPS, for instance, by the application of *isostatic* or *uniaxial pressure* during heating. In the latter, the green pellet is inserted into a die (typically of steel) and subjected to *high uniaxial pressure* (several hundred MPa) with the help of alumina punches and subsequently heated either in vacuum or in inert atmosphere (see Fig. 7). Hence the sintering process is aided by plastic deformation and creep in addition to lattice and GB diffusion

mechanisms, which makes HUP more effective than CPS, thus reducing time and temperature needed during the densification process [87].
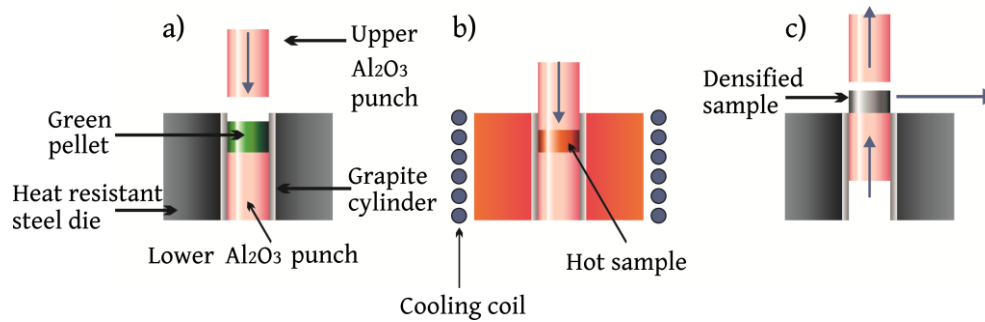

Fig. 7 Schematic of hot uniaxial pressing. a) Die fill stage, b) hot pressing stage and c) sample removal.

Post processing by plastic deformation

For further improvement of the reinforcement distribution, reduction or elimination of porosity and tuning of the microstructure/mechanical properties of the MMC, post processing methods can be applied by means of plastic deformation, e.g. **extrusion**, **forging**, **rolling,** etc., or a combination of these. Nevertheless, plastic deformation methods such as **extrusion** and **forging** are restricted to MMC with discontinuous reinforcement [71]. Regarding the processing by **extrusion,** depending on the reinforcement particle size, volume fraction and on the applied strain, the reinforcement aligns along the extrusion axis, hard particles fracture and the microstructure is refined. **Forging** is performed typically on hot-pressed or extruded products and particles are slightly aligned perpendicular to the forging direction. Furthermore, forging

represents lower costs than extrusion and sinter-forged MMC have similar fatigue and tensile properties as extruded ones [71].

Recently, SPD techniques have been used for the reinforcement homogenization (secondary process) in MMC and for the generation of metallic nanocomposites [74]. For instance, HPT has been used to process CNT-reinforced MMC showing improvement in the reinforcement distribution and mechanical properties [21,88]. Nevertheless, SPD processing of CNT-reinforced MMC induces structural damage on the CNT, which can be detrimental for the microstructural performance of the composites.

In summary, during processing of CNT/MMC, especially by SPD techniques, a trade-off must be found in order to obtain a homogeneous distribution of the CNT without significantly damaging their structure. Relevant discussion in this regard is provided in papers II and III in chapter 4.

2.2.2. Mechanical behavior and strengthening mechanisms of MMC

The mechanical properties of composites depend mainly on the nature, the volume fraction and mechanical properties of the matrix and the reinforcement

and on how they interact during processing and under mechanical loads. In particular, improved mechanical and/or physical properties are desired in MMC (with respect to the matrix). Some aspects regarding the mechanical behavior and the strengthening mechanisms of MMC are considered in the following.

Direct strengthening by **load transfer** takes place both in continuous and in discontinuously reinforced MMC. The load applied to the composite is transferred from the matrix to the reinforcement (stronger than the matrix) across the interface. Nevertheless, the load transfer is more efficient in the case of continuous fibers (due to higher aspect ratio) than in particulate composites [71].

During cooling to room temperature of MMC during processing, due to differences in the **coefficient of thermal expansion (CTE)** between the matrix and the reinforcement, residual stresses arise depending on the volume fraction, size, shape and distribution of the reinforcement, as well as on the processing temperature and mechanical properties of the matrix. For example, in the case of MMC with ceramic reinforcement, which possesses lower CTE than the metallic matrix, tensile residual stresses result in the matrix, whereas compressive residual stresses will be present in the reinforcement [89]. Furthermore, adding ceramic reinforcement leads to an increase in the Young modulus, but MMC yield earlier than the metallic counterpart due to inhomogeneous stress distribution in the matrix [89].

The presence of second-phase particles in MMC also affects the microstructural evolution during processing by stimulating the nucleation of recrystallization [90] and by pinning the GB (Zener drag effect or Zener pinning) [91]. As a result, the grain size is reduced, thus providing **GB strengthening** following a Hall-Petch relation [92]. Thereby, the GB act as obstacles for dislocation movement. Additionally, second-phase particles can act as dislocation obstacles resulting in **particle strengthening.**

In the case of CNT-reinforced MMC, strengthening due to **CTE mismatch** is also present since CNT possess very low or even negative CTE in a wide temperature range [93,94]. Load transfer has been also suggested to play an important role in CNT-reinforced MMC [95–99]. Moreover, GB drag, and thus **grain refinement** take place in MMC in which CNT are mainly located at the GB, where they can pin the microstructure and decrease grain growth during processing at high temperatures and during annealing treatments [22,23,100]. S. Suarez et al. observed that grain growth during sintering of CNT/Ni composites manufactured by solid state processing followed a Zener pinning relationship [22,23] and showed a Hall-Petch behavior [23]. Moreover, grain refinement has been observed in CNT-reinforced MMC with different metallic matrices, as well as an increase in strength (but generally decreased ductility), and improved tribological and physical properties [8,12,16,49,99,101–111]. Those properties depend mainly on the manufacturing process, which determine the distribution, morphology and size of the reinforcement, its bonding (interaction) with the

metallic matrix and the defects introduced to the matrix during manufacturing and processing [98].

2.3. Severe Plastic Deformation (SPD)

Severe plastic deformation (SPD) refers to the application of very large shear strains to a metallic material without significantly changing the overall dimensions and by which a high amount of defects is introduced leading to microstructural refinement. Material strengthening by means of SPD techniques is significantly superior to that obtained by conventional plastic deformation methods (e.g. rolling, forging, etc.) since the true strains introduced by SPD are remarkably larger (>> 10). Even though there are many methods to confer SPD [112,113], the most relevant ones (in which the scientific community has shown the most interest) are **Equal Channel Angular Pressing (ECAP)** [114] – *internal simple shear*, **Accumulative Roll Bonding (ARB)** [115] *–based on ordinary forming operation by rolling* and **High Pressure Torsion (HPT)** [116–119] *–simple shear induced by friction.*

ECAP, on one hand, consists in pressing a sample with a certain cross-section through intersecting channels that have defined angles of curvature (Φ and Ψ, internal and external angle of curvature, respectively. See Fig. 8), with the help of a plunger. With every pass, the sample is subjected to simple shear strain and different routes can be followed by rotating the sample by a certain angle before every pass. ARB, on the other hand, consists in successively rolling, cutting in half, stacking and rolling after respective surface treatment (cleaning) as depicted in Fig. 9. The process is performed with the application of heat in order to enhance the diffusion bonding of the surfaces. Nevertheless, ARB is more

laborious and time consuming than ECAP, which makes the latter a preferred technique for the up-scaling as a material forming process for mass production [120–122].

There are several reviews on the SPD of materials by ECAP and ARB (see [123–125]) and further details will not be discussed. However, since SPD by HPT is more relevant for the present dissertation, it will be discussed in detail in the following chapter.
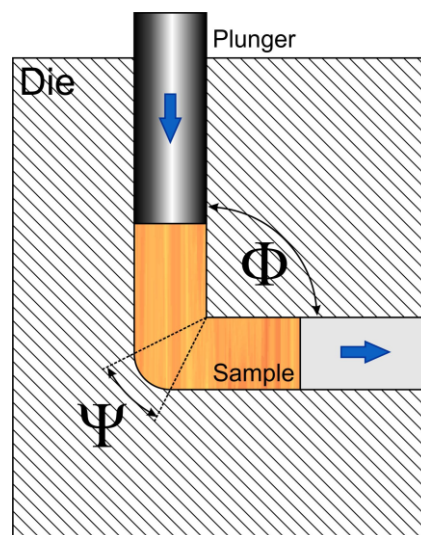

Fig. 8 Schematic of Equal Channel Angular Pressing (ECAP), showing the sample (in form of a rod or a bar) being pressed by a plunger and being bent through a channel with certain internal and external angles.
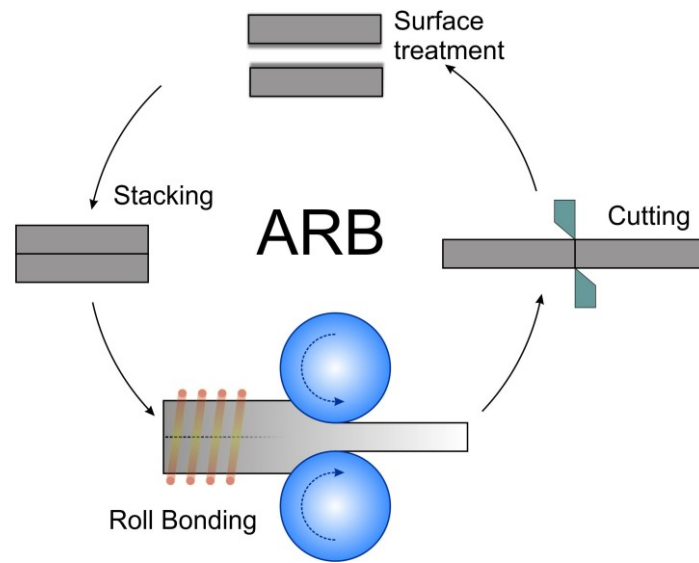
Fig. 9 Schematic illustration of Accumulative Roll Bonding (ARB).

2.3.1. High Pressure Torsion (HPT)

SPD by HPT consists in exerting high hydrostatic pressures (up to 8 GPa) to a disk-shaped sample, which is placed between two anvils, typically under constrained conditions (see Fig. 10). By rotating the lower anvil, the sample is subjected to torsional straining and the deformation (simple shear) is aided by surface frictional forces [119].

Conventionally, the equivalent strain in HPT is calculated by [119,126]:

$$\varepsilon_{VM} = \frac{2\pi Tr}{t\sqrt{3}} \tag{1}$$

where T is the number of turns, r is the distance from the center along the radial direction (i.e. the radius) and t is the thickness of the sample. Under the assumption that the variation of the thickness does not have a significant effect

on the shear strain γ, in HPT $\gamma = \dfrac{r\theta}{t}$, where θ is the rotation angle in radian, $\theta = 2\pi T$. Assuming a von Misses yield locus, the von Mises equivalent strain is given by $\varepsilon_{VM} = \dfrac{\gamma}{\sqrt{3}}$.

Very high equivalent strains can be obtained by HPT and, even though it usually yields grain sizes much smaller than in the case of ECAP and ARB [119,127], the scalability of the technique is more limited. This can be traced back to the microstructural gradient/inhomogeneity along the radius and sample' thickness, the small sample sizes, as well as the need of robust equipment for the application of very high hydrostatic pressure [128]. Despite these challenges, there have been several efforts to upscale HPT to larger sample sizes [129,130]. Nowadays, disks with diameters up to 50 mm and thicknesses of about 10 mm can be processed by HPT at the facilities of the Erich Schmid institute (ESI) in Austria, in an equipment that has a maximum load of 4000 kN.
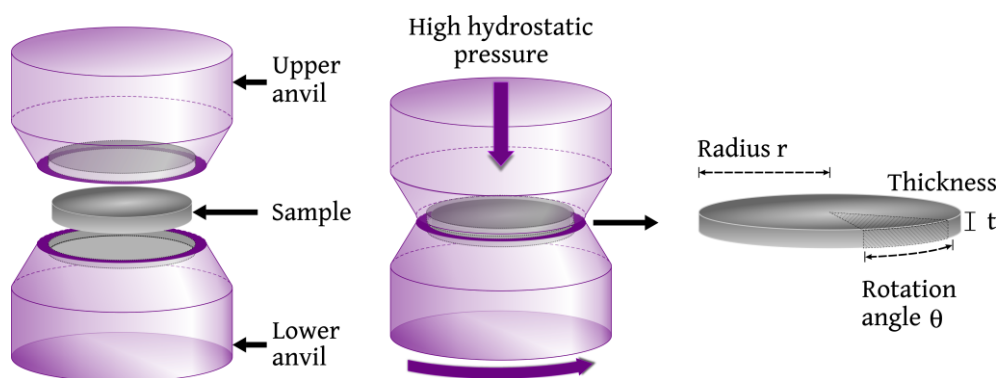

Fig. 10 Schematic of High Pressure Torsion (HPT).

Furthermore, the processing can be performed using different deformation temperatures (from -196 °C up to 700 °C), for instance, by using an induction coil or liquid nitrogen for the heating and the cooling systems, respectively.

The evolution of the microstructure and further characteristics of SPD materials are discussed in the following chapter.

2.3.2. UFG and NC materials by SPD

Microstructural evolution

Microstructure evolution during SPD processing depends on the employed technique and on different process-related parameters (e.g. processing temperature, processing route, induced strain, strain rate, application of high hydrostatic pressure, etc.) and sample-related factors (e.g. chemistry, stacking fault energy, microstructural parameters including texture and initial grain size and defect density, presence of second phases including formation of precipitates and the segregation of impurities and dissolution thereof, etc.).

Regarding the microstructural fragmentation during SPD and its derivation in a steady state (i.e. where no further microstructural changes take place), several dislocation density based models have been proposed throughout the years [113], starting from disclination models [131], which constituted relevant background for the introduction of models based on grain fragmentation by cell

formation in form of rows of dislocation dipoles [113]. These models are based on the understanding that defects are introduced during plastic deformation in form of vacancies, dislocations and GB and, that grain fragmentation occurs when excessively high strains are applied, which leads to the formation of dislocation cells, sub-grains and GB by the arrangement of dislocations and subsequent accumulation of misorientations across the dislocation cell boundaries [113]. Furthermore, L.S. Tóth et al. [132] proposed a model, in which grains are fragmented as a consequence of the development of lattice curvature inside individual grains (rotation of crystallographic planes within a grain caused by dislocation slip) due to constraining of the neighboring grains (lattice rotation is impeded near the GB). This gives rise to geometrically necessary dislocations (GND) leading to grain subdivision, in which texture development was found to play an important role.

There have been several attempts to explain and model the saturation of grain fragmentation during SPD. Nevertheless, it still remains a challenging task. Recently, O. Renk and R. Pippan [133] discussed the current status and open questions in this regard, focusing on single phase materials, from which the following discussion is drawn.

Relevant for the present dissertation are face centered cubic (FCC) metals, which deform predominantly by dislocation slip. However, at low homologous temperature (< 0.2 absolute melting temperature T_m, i.e. at temperatures where

no recovery phenomena are activated) <u>and low strains</u> ($\varepsilon \ll \varepsilon$ needed to reach the steady state), there are other factors that affect the grain fragmentation and the microstructural evolution. One of these factors is the <u>stacking fault energy (SFE)</u>, especially in the case of metals with low SFE, in which twinning and planar slip are favored and their tendency to form macroscopic shear bands is increased. This causes a significantly faster grain subdivision [134,135] leading to higher work hardening rates at early stages of deformation in comparison to metals with medium to high SFE [133]. When <u>severe strains</u> are applied (e.g. by HPT), <u>SFE does not affect the microstructural evolution and the minimum attainable grain size</u> [136–138], resulting in a homogenous nanostructure with predominantly high angle grain boundaries (HAGB).

For very high equivalent strains it was observed that, in the case of Ni single crystals subjected to HPT, the <u>initial crystal orientation had no effect on the texture</u>. Thereby, the texture also reaches a saturation (shear texture) together with the saturation in the microstructural refinement [139]. The <u>initial grain size also does not affect the structure in the steady state</u>, whereby SPD on samples with grain sizes smaller than the saturation grain size (~ 200 nm for Ni) show grain growth upon deformation [140–142]. Furthermore, the <u>strain rate also does not have a significant effect on the saturation grain size at low temperatures</u> [24,143]. This is also true in the case of body centered cubic (BCC) metals [144].

Regarding the mechanisms leading to the saturation of grain refinement during deformation, there must be a dynamic equilibrium between the generation of defects and restoration processes. Specifically, the restoration processes involve the migration of junctions and boundaries, with the former being more relevant at higher temperatures. Furthermore, the fundamental process for boundary migration at low homologous temperatures is the motion of boundary steps, which are linked to mechanical stresses. Thereby, grain growth is accelerated in highly distorted regions due to higher driving force for grain growth [133]. Nevertheless, in several studies the occurrence of the steady state is attributed to the annihilation of dislocations, as discussed in [113].

Finally, factors such as the processing temperature and the addition of alloying elements, impurities and second phases, may play a more important role for the saturation grain size than the previously discussed factors. Specifically, increasing the processing temperature facilitates the arrangement of dislocations into dislocation cells, and the presence of impurity atoms may promote an increase in the dislocation density [24,133].

Mechanical behavior

As a result of the microstructural evolution and grain refinement taking place during SPD, the processed materials show an increase in hardness at early stages of deformation. The hardness reaches homogenization (stays rather constant

throughout the specimen) when the microstructural refinement reaches the steady state. The initial sudden increase in hardness is related to work hardening due to an increase in dislocation density at early stages of the deformation process and, according to the discussion of the last sub-section, as deformation proceeds, dislocations continue to accumulate and eventually start to entangle and arrange into lower energy configurations such as sub-grains, LAGB and HAGB. With sufficiently large applied equivalent strains, restoration processes start to dominate towards the onset of the steady state in the microstructural refinement.

Accordingly, UFG and NC materials obtained by SPD processing usually possess high yield strength due to high dislocation densities (work hardening) and small grain sizes (following a Hall-Petch relation). Nevertheless, in severely deformed materials, the dislocation density and the grain size correlate with each other regarding the increase in hardness, and the linearity of the Hall-Petch plot cannot be taken as GB dominated strengthening [145]. The yield strength (mainly the compressive one) of UFG and NC metals correlates well with the relationship, Vickers Hardness/3 [146,147]. In general, a reduction in ductility is expected in NC materials, mainly due to low work hardening rate, causing early strain localization and failure, in addition to their inability of extensive plastic deformation for the accommodation of crack propagation [148]. Notwithstanding the decreased ductility exhibited by NC materials as strength increases, UFG and NC materials obtained by SPD have exhibited increased yield

strength along with good ductility [149–151]. Moreover, the presence of contaminants and high porosity can significantly reduce the ductility, but a high density of twins can increase it [148].

Based on experimental observations, the occurrence of an inverse Hall-Petch behavior has been suggested [152] (see Fig. 11). Accordingly, analytical models have proposed that this mechanical behavior in NC materials occurs below a critical value D_c (below 25 nm for Cu [148] and ~ 8 nm for Ni [153]) and it is mainly due to GB shear [154]. It should be noted that GB shear differs from GB sliding in that the former involves both GB sliding and GB migration, whereas the latter does not involve GB migration [155]. Regarding the deformation mechanisms in NC materials, it has been implied that dislocations continue to be the main carriers of plasticity down to the smallest grain sizes. For instance, excess porosity [156] and increased dislocation adsorption [152] at small grain sizes lead to deviations in the Hall-Petch behavior. Furthermore, the occurrence of strain hardening [157] (intragranular plasticity) and grain rotation mediated by grain boundary dislocations (GB diffusion dominated plasticity), with dislocation climb instead of cross-grain dislocation slip or GB sliding [158] (studied in a TEM lamella), also implies the important role of dislocations in the deformation of NC materials at room temperature.
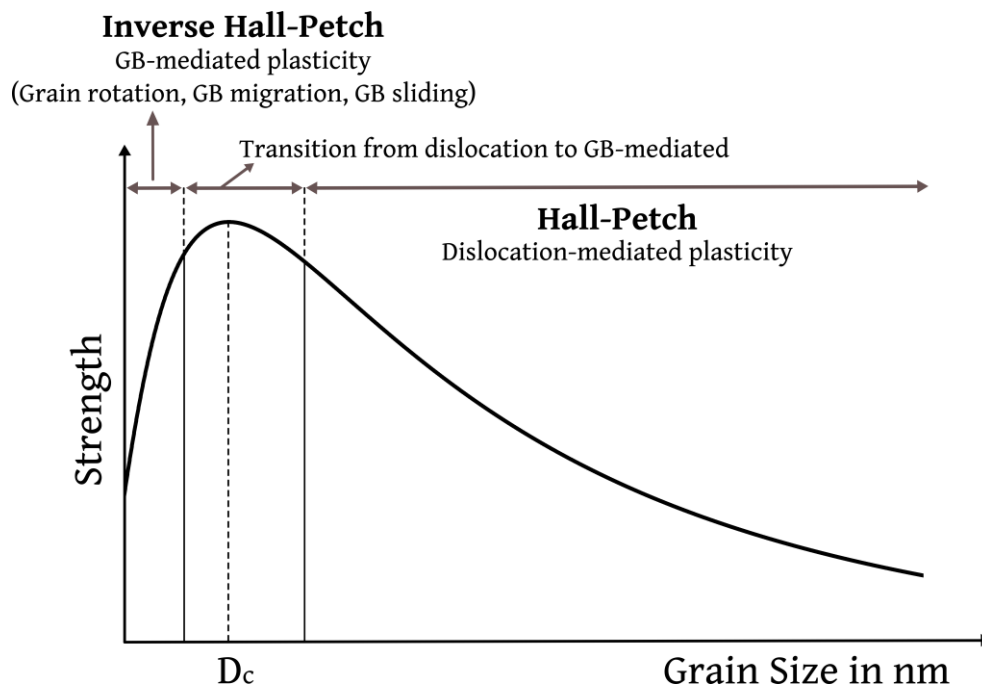
Fig. 11 Schematic of the strength in polycrystalline materials as a function of the grain size. Adapted from [159].

Moreover, NC and UFG materials have been predicted to exhibit superplasticity, which is relevant for the superplastic forming industry, in which complex shapes can be obtained from superplastic metals in one step operation [160]. Superplasticity can be defined as the ability of a material to undergo very large elongation to failure (> 200 %) at high temperatures (> 0.5 T_m) without significant grain growth [161]. This is based on the premise that if GB mainly control the deformation of polycrystalline materials at high temperatures, smaller grain sizes should enable a superplastic behavior [162]. Nevertheless, due to the high amount of defects in the form of vacancies, dislocations and large grain boundary area per unit volume, grain growth can occur already at

low homologous temperatures in NC and UFG materials (particularly those obtained by SPD) [163,164]. Grain growth is driven by a large grain boundary and high strain energies, which limits their application areas and makes it challenging to study the mechanical behavior of these materials at elevated temperatures [161]. However, adding alloying elements or oxide particles has shown to improve the thermal stability in NC and UFG materials [3,4,165] and many alloys severely deformed by HPT have shown superplastic behavior [166]. Further discussion regarding the processing of MMC by HPT is presented in chapter 2.3.3.

Microstructural characterization

There are different characterization techniques by which the microstructural evolution of UFG and NC materials processed by SPD can be studied. Due to the presence of nanoscale structural elements such as non-equilibrium GB, stacking faults and nanotwins, segregation clusters or "clouds" (impurities at GB), nano-sized particles or precipitates, etc., techniques with resolutions down to the nanoscale are required. Electron microscopy techniques, especially high resolution transmission electron microscopy (HRTEM), have proven to be very useful techniques to resolve such nanoscale structural elements, but in cases where the chemical composition must be studied in the atomic scale, for instance to resolve impurities at the grain boundaries, atom probe tomography (APT) is more appropriate.

Furthermore, X-ray diffraction is a well-known technique for the microstructural analysis of NC and UFG materials, in particular those with a high density of defects, which would be challenging to analyze by other techniques. Specifically, information about the crystalline domain size, dislocation density and stacking faults can be extracted from x-ray diffraction patterns by means of line profile analysis (LPA). LPA include <u>traditional methods</u> such as the Scherrer equation [167], Warren-Averbach [168], Williamson-Hall [169] and the modified techniques thereof [170–172], which implement the contrast factor of dislocations, related to the anisotropic nature of the dislocation strain field. These methods rely on the study of <u>diffraction peaks broadening</u> (subtracting the instrumental broadening) for the estimation of crystalline domain sizes and dislocation densities, whereby the strain field arises mainly from the dislocations contained in the crystals and in many cases, the dislocation density is calculated via the Williamson-Smallman equation from the measured microstrain ε and grain size D (crystalline domain size) [173–175] $\rho = \frac{2\sqrt{3}\varepsilon}{Db}$ (b is the magnitude of the Burgers vector), which is only valid for randomly distributed dislocations.

Alternatively, the method by <u>Whole Powder Pattern</u> (WPPM) has been developed [176], in which <u>physical models </u>describe the line profiles of the specimen and the instrument, from which the crystalline domain size and the dislocation density are obtained, <u>without fitting the diffraction profile to arbitrary bell-shaped functions</u> as in traditional techniques.

WPPM is thus considered an optimum technique for the microstructural analysis of severely deformed materials regarding the crystalline domain sizes and dislocation densities. Further details regarding the use of WPPM are provided in paper IV in chapter 4.

Thermal analysis

Regarding the assessment of the thermal stability and the stored energy in severely deformed NC and UFG materials, different techniques have been used. For instance, **differential scanning calorimetry (DSC)**, in which non-reversible energy changes undergone by the specimen during heating can be detected, and the energy released/absorbed can be measured as a function of time or temperature, have been extensively used for the thermal analysis of UFG metals processed by SPD (see [177] and references therein). The stored energy related to the annealing of dislocations has been related to their density ρ [178] as $E_{stor} = Gb^2 \frac{\rho}{4\pi k} ln\left[\frac{1}{b\sqrt{\rho}}\right]$ [179], where G is the shear modulus and k is the arithmetic average of 1 and (1-ν) (if equal contributions from edge and screw dislocation is assumed, ν is the Poisson ratio). Furthermore, the activation energy for recovery and recrystallization can be obtained by using the Kissinger equation [180] $ln\frac{V}{T_p^2} = -\frac{Q}{R}\frac{1}{T_p} + A$, in which the activation energy is related to

the shift of the respective exothermic peak with the changes in heating rate (see Fig. 12), V is the heating rate; T_p, the peak temperature; Q, activation energy; R, universal gas constant and A, a constant. In general, the released heat in DSC increases with decreasing grain size and the exothermic peak related to the annihilation of dislocations and grain growth shifts to lower temperatures with increasing applied strain [178,181]. Thus, the thermal stability of severely deformed metals is expected to decrease with increasing applied strain.
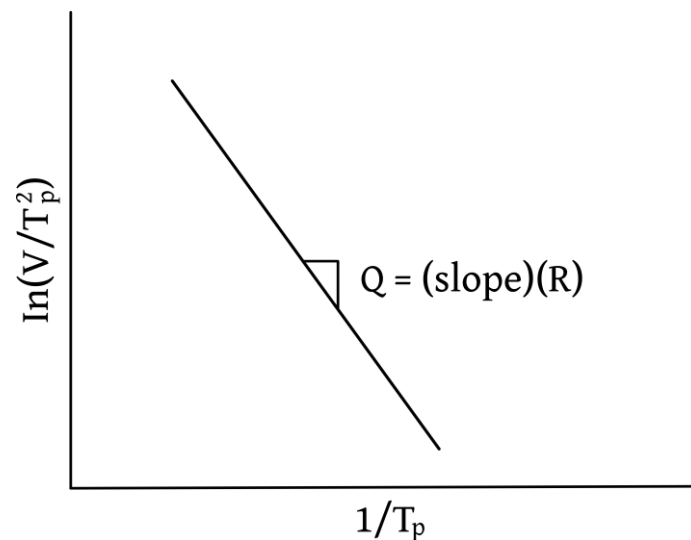

Fig. 12 Schematic of a Kissinger plot.

The thermal stability of severely deformed metals, in terms of changes in the crystallite size (homologous to grain growth analysis) and the dislocation density, can be studied by in-situ heating X-ray diffraction by means of X-ray LPA within the detection limits of the experimental set-up (for instance, up to ~ 800 nm grain size and above $\rho \sim 10^{13}$ m^{-2} for a laboratory diffractometer [181]).

Additionally, post annealing analysis by means of electron backscatter diffraction (EBSD) or TEM provides information about the final grain size and defect density.

2.3.3. MMC by SPD

SPD has been applied to MMC mainly to reduce the second phase particle size and to improve the distribution, as well as to enhance the strength of the material. Equivalently, second phases have been introduced to metallic matrices to reduce the saturation grain size (by improving the structural stability [151]) and to enhance the mechanical properties.

Regarding the microstructural evolution during SPD of MMC, apart from the factors discussed for single phase materials in chapter 2.3.2., it also depends on the size and the volume fraction of the reinforcing phase [74]. Furthermore, the deformation mechanisms are strongly influenced by the presence of reinforcements, which interact with dislocations by Orowan mechanism (when particles are located mainly at grain interiors and if particle size is sufficiently small), act as blockage for dislocation slip (for large particle size) and may limit GB migration (if located at the grain boundaries) [151,182,183]. During SPD of MMC, there is a significant decrease in the saturation grain size and the thermal stability is generally improved in comparison to the respective single phase materials (see [74] and references therein).

There are several reports on improved mechanical behavior, thermal stability and microstructural evolution of CNT-reinforced MMC processed by SPD (for instance, Cu/CNT [182–186] and Al/CNT [25,26]). Regarding Ni/CNT systems, the mechanical behavior of composites consolidated by spark plasma (not SPD) was reported in [187]. Nevertheless, studies on SPD of Ni/CNT composites are still limited in the literature, and the majority of related research has been conducted by our group during the time, by which the present dissertation was being developed. According to our results, regarding the mechanical performance of SPD Ni/CNT composites, it was found that in order to reach the steady state in the microstructural refinement with high hardness (>700 HV) and small grain size (< 100 nm) by HPT, thermomechanical processing (30 T of HPT at 400 °C) and post deformation at room temperature (5 T of HPT) is one optimum processing route [188]. Furthermore, tensile tests performed on micro-size samples of CNT/Ni composites showed that composites with low CNT content (0.25 wt.% CNT), processed by 30 T of HPT at 400 °C and 10 T of HPT at 200 °C, possess both high strength (~1.75 GPa UTS and ~1.7 GPa Yield strength) and good ductility (~0.85% uniform elongation and ~45% reduction in area) [189].

Regarding the improved thermal stability in NC and UFG materials, it has been reported that thermodynamic stabilization (segregation of solute atoms at the GB to lower their energy) and kinetic stabilization (second-phase particle pinning to lower GB movement) play an important role [3,74,151,165,190]. Furthermore, CNT have been suggested to restrict the diffusion paths at high

temperatures, as well as the dislocation movement in Al/CNT composites [191]. Therefore, adding CNT to materials subjected to SPD is expected to improve their thermal stability.

Nevertheless, no systematic investigations had been yet done in the literature on the thermal stability of SPD Metal/CNT composites, specifically, regarding the microstructural evolution during heating, as well as the limiting grain size after annealing as a function of the CNT content.

Additionally, as a result of their significantly higher hardness (when compared with their coarse-grained counterparts), SPD materials are expected to show a decrease in the steady state coefficient of friction (COF) and wear during tribological contact. Yet, a finer microstructure increases the oxidation activity due to a high amount of GB area, which can affect both friction and wear. It has been proposed that the addition of reinforcements to SPD materials should improve their wear resistance [192,193], and since CNT have been proven to improve both the frictional and wear behavior in MMC during tribological contact (by dry sliding) [47,48,50], SPD Ni/CNT composites may exhibit improved frictional behavior compared to NC Ni. However, no investigations on the lubrication effects of CNT in SPD MMC had been yet done in the literature.

In summary, investigation on the microstructural evolution and the performance of SPD Ni/CNT composites regarding their thermal stability and the tribological behavior, <u>is of great relevance to obtain relevant understanding on the material properties of CNT-MMC processed by SPD techniques.</u>

Thorough discussion in this regard can be found in papers V and VI in chapter 4.

To gain further insights into the state of the art related to each individual analysis carried out in the present dissertation, the reader is referred to the corresponding publication contained in the "Results and Discussion" chapter.

3. Approach and overview

Based on the increasing number of publications regarding CNT-MMC, it is obvious that the scientific community has been very interested in the promising characteristics that CNT can provide to metallic matrices of different nature [9,13,100−108,191,192−194,92−94,96,98,99]. Regarding the deformation of CNT-MMC, the formation of carbides would be promoted by the introduction of defects during processing due to the energetic nature of HPT. However, nickel carbide (Ni_3C) is not expected to form in a wide temperature range (0-1500 °C) due to its metastable nature with positive Gibbs free energy of formation [198]. Therefore, **Ni was used in the present dissertation as the metallic matrix**. Even though CNT/Ni systems [21−23,53,58,85,86] and the deformation behavior of pure Ni by HPT have been studied in the literature (see for example [143] and references therein), **an extensive study on the phenomena involved during HPT on CNT/MMC had not yet been performed in the literature before the present dissertation**.

According to the highlighted points in the boxes throughout the state of the art and to the open questions identified in the literature, the following three objectives were proposed:

Objective 1

The first objective of the present dissertation is **to study the effect on the microstructural evolution and on the CNT structural changes during SPD of CNT/MMC by HPT.** Bulk CNT-reinforced MMC will be synthetized and processed by HPT at room temperature. A preliminary assessment of the microstructure should be carried out followed by a thorough analysis of the structural changes undergone by the CNT in order to assess to what extent these can hold the deformation process without compromising their intrinsic features. Additionally, an extensive study on the CNT distribution homogenization must be performed, in which advanced image analysis is combined with concepts from spatial statistics. This aims at obtaining a model, which predicts the minimum effective strain needed to achieve a homogeneous distribution of the reinforcement during HPT.

> **This objective was addressed in papers I, II and III.**

Objective 2

The second objective is **to understand the interaction between the matrix and the CNT during processing and under mechanical loading.** The evolution of microstructural parameters of CNT-reinforced MMC during HPT with increasing applied strains and CNT content should be analyzed. The focus

should be on the changes in dislocation density and the grain size. The proper technique to be used should be carefully chosen and, based on the results, the main strengthening mechanisms should be assessed.

> **This objective was addressed in paper IV.**

Objective 3

The third objective of this dissertation is **to evaluate the performance of the severely deformed CNT/MMC regarding their thermal stability and tribological behavior.** The performance of the composites after processing by HPT regarding their thermal stability should be studied focusing on the grain growth and the recovery phenomena occurring during heating. Furthermore, annealing treatments on the severely deformed composites should be carried out in order to analyze the limiting grain size depending on the CNT composition. Regarding the friction and tribo-chemical behavior, the microstructural changes after micro-tribological testing should be studied.

> **This objective was addressed in papers V and VI.**

These objectives constitute the **key topics of this work** and an overview of the scientific findings are introduced in the following:

Outline

I A preliminary study is carried out focused on the microstructural analysis of the "as sintered" and "as deformed" conditions in CNT-reinforced Ni-MMC fabricated by solid state processing and processed by HPT at room temperature. Vickers microhardness and electron microscopy are used as the main characterization techniques. The as deformed composites exhibited a finer microstructure with smaller agglomerate size and higher hardness. The microstructural steady state was not reached.

II

A thorough study is performed on the influence of processing CNT-reinforced Ni-MMC by HPT on the CNT structural state using Raman spectroscopy as the main characterization technique by analyzing the evolution of different descriptive parameters including the G-band full width at half maximum (crystallinity related), I_D/I_G ratio (defect related). The analysis of the G-band position was found to be essential (amorphization-stage-related). The damage is associated with the accumulated strain and changes with the CNT fractions. The damage mechanism is correlated to a well-established carbon amorphization trajectory proposed in the literature.

III

A thorough analysis on the evolution of the microstructural features and the clustering behavior of the CNT during different stages of the deformation process is performed using a systematic methodology that involves concepts from image analysis and spatial statistics. Furthermore, a model for the prediction of the minimum accumulated strain required to achieve a homogeneous distribution of the second phase during HPT is developed and correlated with the experimental results.

IV   The evolution of dislocation densities and crystalline domain sizes are analyzed by means of XRD using WPPM. The size of the measured area is limited along the radial direction to reduce the effect of the microstructural gradients on the results. The effect of increasing CNT content and increasing strain is investigated. In particular, a higher amount of screw dislocations was measured by WPPM. The strengthening of CNT-MMC processed by HPT is mainly due to work hardening and grain refinement, both being assisted by the presence of CNT, with marginal contribution of particle strengthening.

V   A thorough analysis of the microstructural evolution during heating and the thermal stability of CNT-reinforced Ni MMC processed by HPT, was performed using DSC, HT-XRD and EBSD. The formation and dissolution of metastable Ni_3C phase was evidenced by DSC and HT-XRD in composites with sufficient carbon atoms available as a consequence of irreversible damage on the CNT introduced by HPT. Nevertheless, the composites exhibit an improved thermal stability with respect to Ni samples processed under the same conditions.

VI Micro-tribological testing (100 mN load, 3 mm diameter counter body) is performed on deformed Ni and CNT/Ni composites in order to analyze the effect of CNT content and increasing equivalent strains on their frictional and tribo-chemical behavior. The microstructure beneath the wear scar is analyzed by FIB cross-sections. As a result of structural damage, which is introduced on the CNT during SPD, and of a continuous formation/damage of a stable oxide layer during tribo-contact, the CNT lubricant ability is counteracted. Consequently, the steady state COF reaches the same value in all the studied samples. The microstructure under the wear scar do not show evident changes, which is related to a hardened surface, especially in the composites, in which the wear is reduced with respect to Ni.

4. Results and discussion

The scientific findings within the cumulative part of this dissertation are reported in the following publications:

I. **Evolution of the microstructure in carbon nanotube reinforced Nickel matrix composites processed by high pressure torsion**

II. **Study of the structural defects on carbon nanotubes in metal matrix composites processed by severe plastic deformation**

III. **On the reinforcement homogenization in CNT/metal matrix composites during severe plastic deformation**

IV. **Evolution of the lattice defects and crystalline domain size in carbon nanotube metal matrix composites processed by severe plastic deformation**

V. **Microstructural evolution during heating of CNT/Metal Matrix Composites processed by Severe Plastic Deformation**

VI. **Friction and tribo-chemical behavior of SPD-processed CNT-reinforced composites**

I. Evolution of the microstructure in carbon nanotube reinforced Nickel matrix composites processed by high pressure torsion

Katherine Aristizabal[1], Sebastián Suárez[1], Andreas Katzensteiner[2], Andrea Bachmaier[2], Frank Mücklich[1]

1 Department of Material Science and Engineering, Saarland University,
66123 Saarbrücken, Germany
2 Erich Schmid Institute, Austrian Academy of Sciences, Jahnstrasse 12, 8700 Leoben,
Austria

Own Contribution: Project management, sample manufacturing and processing, experimental execution, data analysis and manuscript writing.

Abstract:

Carbon nanotube (CNT)-reinforced nickel matrix composites were processed using high-pressure torsion (HPT) at room temperature (RT). Different CNT weight fractions were used in order to study the behavior of the composites in the "as sintered" and the "as deformed" conditions and to determine the effect of the amounts of CNT added on the different processing methods. The samples were analyzed by means of Vickers microhardness and electron microscopy. According to the results, increasing the CNT content in the "as sintered"

condition increases the agglomerate size but decreases only slightly the grain size. Regarding the "as deformed" condition it showed little to negligible effect in further refining the microstructure. By means of HPT the hardness was increased up to 800%. It was concluded that the microstructure could be further improved in terms of grain size and agglomerate size and distribution by means of HPT.

Evolution of the microstructure in carbon nanotube reinforced Nickel matrix composites processed by high-pressure torsion

K Aristizabal[1,*], S Suárez[1], A Katzensteiner[2], A Bachmaier[2], and F Mücklich [1, 3]

[1] Chair of Functional Materials. Department of Materials Science, Campus D3.3, 66123 Saarbrücken, Germany.

[2] Erich Schmid Institute, Austrian Academy of Sciences, Jahnstrasse 12, 8700 Leoben, Austria

[3] Materials Engineering Center Saarland, Campus D3.3, D-66123, Saarbrücken, Germany.

E-mail: katherine.aristizabal@uni-saarland.de, s.suarez@mx.uni-saarland.de, andreas.katzensteiner@oeaw.ac.at, andrea.bachmaier@oeaw.ac.at, muecke@matsci.uni-sb.de

Abstract. Carbon nanotube (CNT)-reinforced nickel matrix composites were processed using high-pressure torsion (HPT) at room temperature (RT). Different CNT weight fractions were used in order to study the behavior of the composites in the "as sintered" and the "as deformed" conditions and to determine the effect of the amounts of CNT added on the different processing methods. The samples were analyzed by means of Vickers microhardness and electron microscopy. According to the results, increasing the CNT content in the "as sintered" condition increases the agglomerate size but decreases only slightly the grain size. Regarding the "as deformed" condition it showed little to negligible effect in further refining the microstructure. By means of HPT the hardness was increased up to 800%. It was concluded that the microstructure could be further improved in terms of grain size and agglomerate size and distribution by means of HPT.

1. Introduction

Seeking the stabilization of the microstructure against grain growth is critical in nanocrystalline (NC) and ultrafine-grained (UFG) materials processed by severe plastic deformation (SPD), since they possess high amounts of stored energy in their large grain boundary area, giving them an unstable nature. This instability can activate microstructural recovery and grain growth processes even at low temperatures that can alter the material properties considerably. In some studies, the addition of reinforcing phases to metallic matrices subjected to SPD has been performed with the aim of overcoming this issue and given a proper distribution of the particles [1] they even result in enhanced mechanical properties [2, 3]. The resulting metal matrix composites (MMC) behave differently than pure metals and provided that the appropriate reinforcing phase is chosen and a uniform distribution of the agglomerates can be obtained, the thermal instability drawback might be overcome by making use of different mechanisms (e.g. by hindering the grain boundary and dislocation mobility).

1

In this study, we propose the use of carbon nanotubes as reinforcing phase in Ni matrix composites, acting a stabilizing second phase. The choice is based on the fact that, though they possess outstanding intrinsic properties, they have also shown the ability to pin the grain boundaries under thermal inputs [4, 5]. The results presented here are emphasized on the comparison between the "as sintered" and the "as deformed" conditions of the studied composites and serve as a starting point of a deeper microstructural study, which will be discussed elsewhere.

2. Experimental

Carbon nanotube (CNT)-reinforced nickel matrix composites were processed using high-pressure torsion (HPT). Different CNT weight fractions were studied, namely: 0.5 wt.% (2.4 vol.%), 1 wt.% (4.8 vol.%), 2 wt.% (9.5 vol.%) and 3 wt.% (14.5 vol.%). These composites were sintered by means of hot uniaxial pressing (HUP) and afterwards subjected to HPT at room temperature (RT) using different number of turns (1T, 4T, 10T and 20T) under 4 GPa of pressure.

The "as sintered" condition was analyzed by means of Vickers micro-hardness, scanning electron microscopy (SEM), with a resolution of 125 nm per pixel, and electron backscattered diffraction (EBSD). The electron microscopy characterization was performed on a dual beam system Helios NanoLab 600 (FEI). The EBSD measurements were performed with an EDAX TSL detector, with a 20 kV voltage bias and 22 nA current. The step size for the analysis was varied for the different samples, ranging from 150 to 500 nm.

The evolution of the microstructure along the radial direction, corresponding to increasing equivalent strain values ε_{vM} [6] (according to $\varepsilon_{vM} = \frac{2\pi n r}{t\sqrt{3}}$, where n is the number of turns, t is the sample thickness and r the distance from the center of the sample), was studied by means of SEM using backscattered electron imaging (BSE) as a faster way of obtaining information about the mean grain size (equivalent diameter), given that in the "as deformed" samples, the significant residual stresses made difficult the proper sample preparation for EBSD. The shape, size and distribution of the CNT agglomerates were also studied. The images were taken every 1 mm along the radial direction with a resolution of 2.5 nm per pixel.

Vickers micro-hardness, which is extensively used as a quick way of assessing the saturation in the microstructural refinement of such composites, was performed every 0.5 mm along the radial direction, using an indenter Struers DuraScan 50/70/80.

3. Results and discussion

The mean grain size values obtained for the different compositions of the HUP samples by means of EBSD lay all within the micrometer range and are summarized in Table 1. From these values, no clear correlation between the mean grain size and the CNT concentration can be extracted. This might be due to an incomplete pinning effect of the CNTs on the grain boundaries during the densification stage [7].

Table 1. Mean grain sizes of HUP samples obtained by EBSD. For the determination of the mean and standard deviation, a log-normal distribution was assumed.

HUP Samples	Mean grain size [μm]
0.5wt.% MWCNT/Ni	4.80 ± 2.89
1wt.% MWCNT/Ni	3.10 ± 1.17
2wt.% MWCNT/Ni	3.42 ± 1.55
3wt.% MWCNT/Ni	3.67 ± 1.67

Figure 1 shows the evolution of the grain size (equivalent diameter) along the radius of the samples, obtained from BSE images for the deformed samples. Here, it was assumed that the grains are the areas delimited by the different gray values within the image, and the misorientation angle between the grains, which cannot be measured with this method, was not considered. The results show a large decrease in grain size after HPT and at early stages of the deformation, but only a subtle decrease with increasing equivalent strains reaching values down to 100 nm, which is independent of the CNT volume fraction. From this, it can be stated that the increment of the CNTs volume fraction has little to negligible effect on further refining the microstructure during deformation, presenting similar results regarding the grain size for the same processing conditions (as shown in Figure 1).
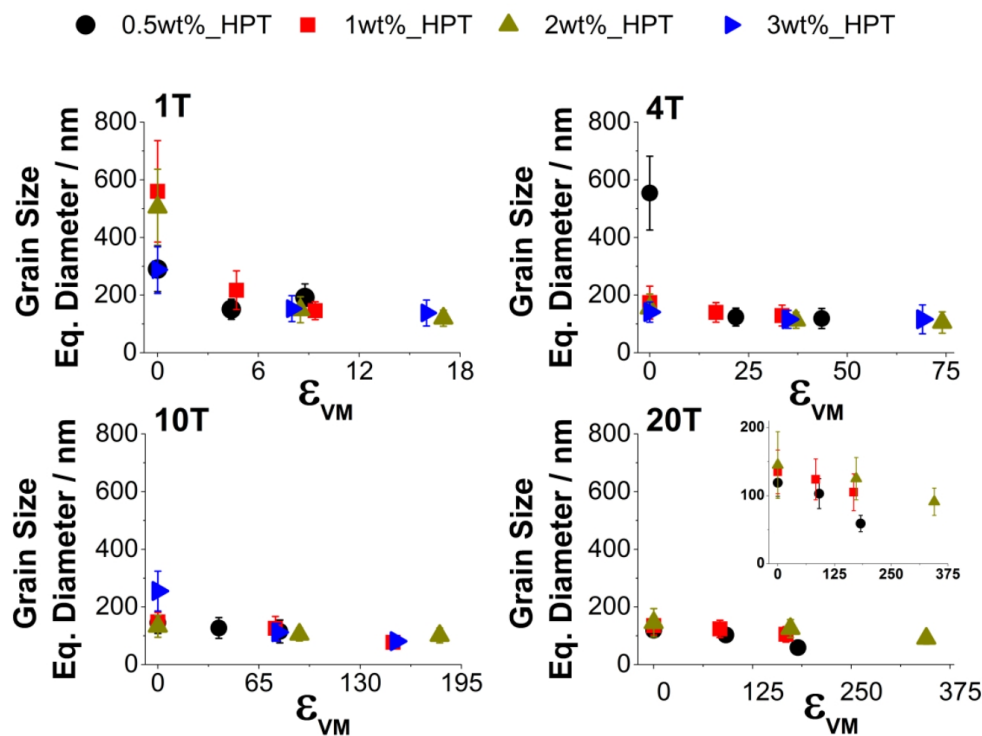
Figure 1. Change in grain size (equivalent diameter) with increasing equivalent strains. (Sample 3wt.% could not be further deformed by HPT at RT due to its high hardness causing slippage between the sample and the anvils).

Regarding the hardness, table 2 summarizes the values for the as sintered condition (HUP). The hardness increases only slightly with increasing CNT content. This correlates well to what has been previously reported in the literature [4], and is traced back to the role played by the partial CNT concentration in the dislocation mobility hindering in these composites during the indentation stage. The CNTs act as pinning points to the dislocation fronts, progressively reducing their energy. This effect combined with the microstructural refinement, leads to a combination of two strengthening mechanisms, namely: grain boundary strengthening (Hall-Petch effect) and dispersion strengthening (Orowan mechanism). Since there are no relevant changes in the mean grain size in the HUP state, the largest role in the enhancement might thus be provided by an Orowan-type mechanism.

3

Table 2. Vickers hardness HUP samples as a function of the partial CNT fraction.

HUP Samples	Hardness [GPa]
0.5wt.% MWCNT/Ni	1.17 ± 0.05
1wt.% MWCNT/Ni	1.17 ± 0.03
2wt.% MWCNT/Ni	1.20 ± 0.07
3wt.% MWCNT/Ni	1.31 ± 0.07

In Figure 2 the evolution of the hardness along the radial direction is shown for the HPT samples. The results show a significant increase in hardness with increasing equivalent strains of about 800 % with respect to the as sintered condition. Interestingly, even after 20 turns the hardness values continue to increase indicating that the onset of the microstructural refinement saturation has not been reached for the equivalent deformation here studied. Remarkably, all the analyzed concentrations show the similar trends in the hardening behavior. Thus, it could be stated that this feature is mainly based on the nature of the matrix and cannot be straightforwardly correlated to the amount of second phase. Nevertheless, a slight decrease in the "slope" of the "lines" is observed for increasing CNT content, which can be a "sign" that the dislocation and grain boundary mobility are hindered by the CNT during deformation.
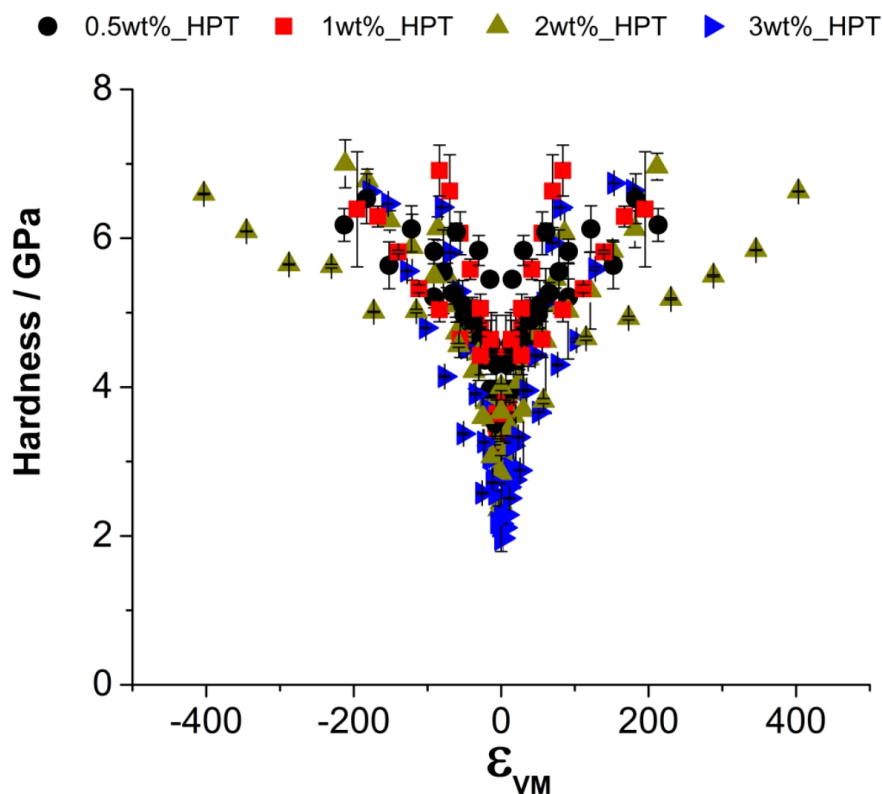
Figure 2. Variation of the hardness with increasing equivalent strains. The negative values of the equivalent strain represent only the opposite direction of the radius and do not depict a physical value.

4

Focusing on the effect of the deformation on the CNT agglomerate morphological characteristics, the analysis is directed to the study of the change in size and shape of the CNT clusters. Figure 3 shows binarised images for the HUP samples showing the CNT agglomerates and the corresponding mean agglomerate size values are summarized in table 3. From this observation, it becomes evident that the agglomerate size increases with increasing CNT content. This is explained by the fact that for larger CNT concentrations, there is a lower mean free path for CNT re-clustering. This has been already observed in sintered bulk metal matrix composites, and is traced back to the fact that, since the CNTs are not embedded in the metal particles, the material transport during sintering brings them closer together increasing their probability of reagglomeration due to van der Waals interactions [8].
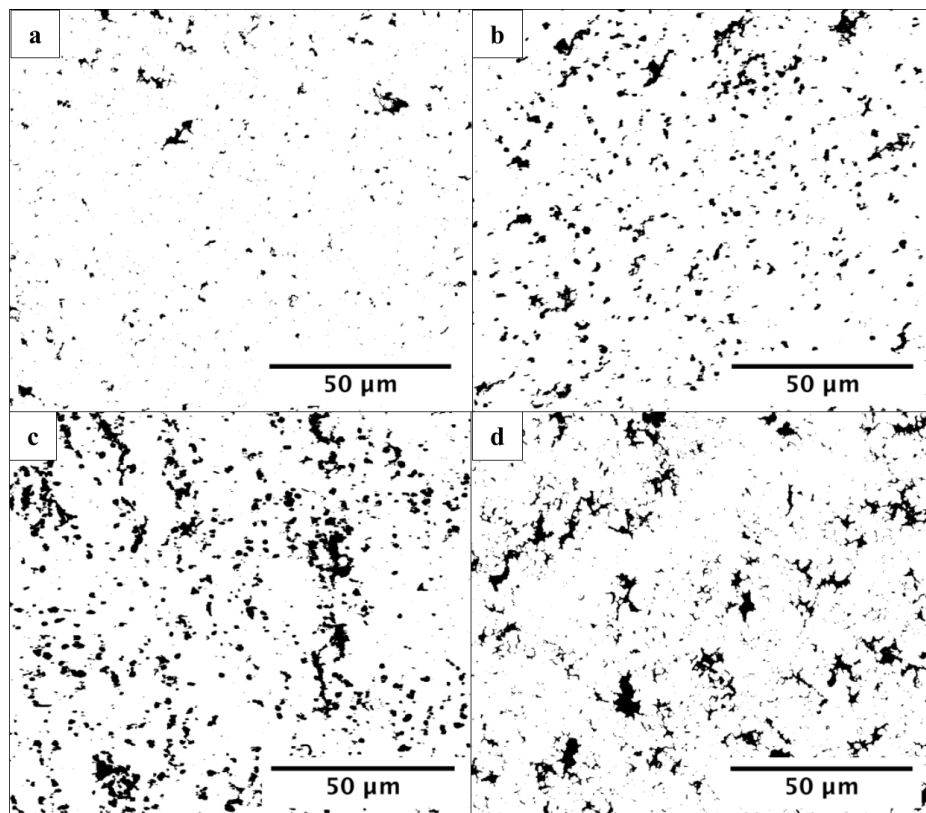
Figure 3. Binary images HUP samples. a) 0.5wt.% MWCNT/Ni, b) 1wt.% MWCNT/Ni, c) 2wt.% MWCNT/Ni and d) 3wt.% MWCNT/Ni.

Table 3. Mean agglomerate sizes of HUP samples obtained by image analysis using the image-analysis software FIJI.

HUP Samples	Mean agglomerate size [µm]
0.5wt.% MWCNT/Ni	1.91 ± 1.52
1wt.% MWCNT/Ni	2.44 ± 1.62
2wt.% MWCNT/Ni	3.11 ± 2.41
3wt.% MWCNT/Ni	3.77 ± 2.34

Concerning the as-deformed state, figure 4 presents BSE images taken at 3 mm from the center for different compositions and number of turns. The evolution of the shape, the distribution and the agglomerate size can be exemplarily visualized in this figure. The agglomerates develop an elongated shape in the shear direction at early stages of the deformation. With higher number of turns, the agglomerates become more rounded and their distribution improves. The agglomerate size decreases significantly when comparing to the as sintered condition, reaching values down to the sub-micrometer range.
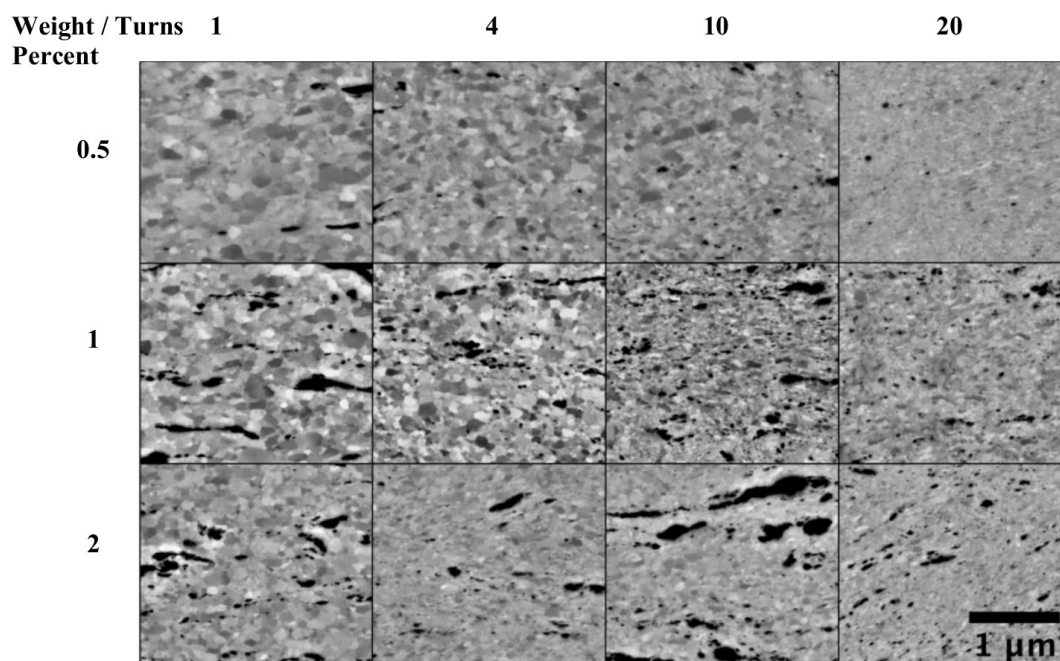
Figure 4. BSE images for a sample set at a radius of 3 mm. (Equivalent strain increases from left to right).

The decrease in grain size is within the same range and remains almost constant for the higher equivalent strains (as shown in figure 2), resembling the saturation onset of the microstructural refinement. Nevertheless, according to the Vickers hardness results, this statement cannot be confirmed for the parameters of HPT here studied. The results suggest that the microstructure can be

Katherine Aristizabal   61   Results and discussion

further refined in terms of grain size (see inset in figure 1) and improved in terms of agglomerate size and distribution by means of HPT.

4. Concluding remarks

CNT reinforced Ni matrix composites with different CNT contents were processed by HPT at RT using 4 GPa of pressure. When comparing to the HUP samples, it could be shown that after HPT not only the grain size but also the agglomerate size decreases and the microhardness increases significantly. Nevertheless, increasing the CNT content both in HUP and in HPT samples showed little to negligible effect on further refining the microstructure. Furthermore, the size and spatial distribution of the agglomerates was improved by HPT. Finally, the results suggest that the microstructure can be further improved in terms of grain size and agglomerate size and distribution by means of HPT (e.g. by optimizing the parameters used during processing).

Acknowledgments

References

[1]   Bachmaier A and Pippan R 2013 *Int. Mater. Rev*. 58 41–62
[2]   Islamgaliev R K, Buchgraber W, Kolobov Y R, Amirkhanov N M, Sergueeva A V, Ivanov K V and Grabovetskaya G P 2001 *Mater. Sci. Eng. A* 319–21 872–6
[3]   Bachmaier A and Pippan R 2011 *Mater. Sci. Eng. A* 528 7589–95
[4]   Suarez S, Lasserre F, and Mücklich F 2015 *Mater. Sci. Eng. A* 587 381–386
[5]   Suarez S, Lasserre F, Soldera F, Pippan R and Mücklich F 2015 *Mater. Sci. Eng. A* 626 122–7
[6]   Stüwe H P 2003 *Adv. Eng. Mater.* 5, 291–5
[7]   Reinert L, Suarez S, Müller T, and Mücklich F 2017 *Adv. Eng. Mater.*
DOI: 10.1002/adem.201600750
[8]   Rossi P, Suarez S, Soldera F, and Mücklich F. 2015 *Adv. Eng. Mater*. 17(7) 1017-21.

II. Study of the structural defects on carbon nanotubes in metal matrix composites processed by severe plastic deformation

Katherine Aristizabal[1], Andreas Katzensteiner[2], Andrea Bachmaier[2], Frank Mücklich[1], Sebastián Suárez[1]

1 Department of Material Science and Engineering, Saarland University,
66123 Saarbrücken, Germany
2 Erich Schmid Institute, Austrian Academy of Sciences, Jahnstrasse 12, 8700 Leoben, Austria

Own Contribution: Project management, sample manufacturing and processing, experimental execution, data analysis, conceptualization of experimental results and manuscript writing.

Abstract:

Carbon nanotubes (CNT) have been recently proposed as stabilizers against grain growth that can happen even at low temperature inputs in nano-crystalline and ultrafine-grained materials obtained by severe plastic deformation. In this study, we analyzed the evolution of the structural defects on the nanotubes in CNT-reinforced nickel matrix composites with different reinforcement weight fractions. The composites were processed by high pressure torsion, and we used Raman spectroscopy as the main characterization

technique. The results indicate that for CNT subjected to highly energetic processing, it is not sufficient to analyze only the ID/IG ratio (as proposed in the available literature), but it is also necessary to evaluate the shifting of the G-band, which traces the amorphization trajectory undergone by the CNT. Furthermore, we observed that the deformation suffered by the CNT is related to the accumulated strain and varies with the partial CNT fractions of these composites. This is related to their capacity to withstand the plastic strain that occurs during deformation. In addition, the defective state reaches a saturation before achieving the saturation in the microstructural refinement. These results will help to efficiently optimize the processing of this type of engineering composites.

Study of the structural defects on carbon nanotubes in metal matrix composites processed by severe plastic deformation

Katherine Aristizabal [a], Andreas Katzensteiner [b], Andrea Bachmaier [b], Frank Mücklich [a], Sebastian Suarez [a, *]

[a] *Chair of Functional Materials, Department of Materials Science, Saarland University, D-66123, Saarbrücken, Germany*
[b] *Erich Schmid Institute of Materials Science, Austrian Academy of Sciences, Jahnstrasse 12, A-8700, Leoben, Austria*

A B S T R A C T

Carbon nanotubes (CNT) have been recently proposed as stabilizers against grain growth that can happen even at low temperature inputs in nano-crystalline and ultrafine-grained materials obtained by severe plastic deformation. In this study, we analyzed the evolution of the structural defects on the nanotubes in CNT-reinforced nickel matrix composites with different reinforcement weight fractions. The composites were processed by high pressure torsion, and we used Raman spectroscopy as the main characterization technique. The results indicate that for CNT subjected to highly energetic processing, it is not sufficient to analyze only the I_D/I_G ratio (as proposed in the available literature), but it is also necessary to evaluate the shifting of the G band, which traces the amorphization trajectory undergone by the CNT. Furthermore, we observed that the deformation suffered by the CNT is related to the accumulated strain and varies with the partial CNT fractions of these composites. This is related to their capacity to withstand the plastic strain that occurs during deformation. In addition, the defective state reaches a saturation before achieving the saturation in the microstructural refinement. These results will help to efficiently optimize the processing of this type of engineering composites.

© 2017 Elsevier Ltd. All rights reserved.

1. Introduction

Carbon nanotubes (CNT) possess superior characteristics (outstanding physical properties, low weight and high aspect ratio), which render them as suitable candidates to be used as reinforcement in composite materials. In the past years, there have been several reports where they are used as reinforcements in metal matrix composites (MMC) with different metallic matrices, aiming mainly to improve the electrical and mechanical properties. An improvement in the mechanical properties has been observed by adding different volume fractions of CNT to different metallic matrices (e.g. Al [1—8], Cu [9—11] and Ni [12—14]). Nevertheless, the processing route also dictates to what extent the properties are improved, where the agglomerates and a weak interface can lead to a lower improvement [15] or even to a deterioration thereof [16]. CNT have been also used in MMC as stabilizing phases against grain growth in materials subjected to severe plastic deformation (SPD)

[17,18]. This was based on their ability to pin the grain boundaries in coarse-grained materials under thermal inputs, enabling the control of the final microstructure [19] and subsequently, the tailoring of their mechanical properties [12]. Particularly, the boundary drag effect becomes more evident in composites manufactured by solid-state routes (e.g. powder metallurgy), since the reinforcement can only be placed on grain boundaries, as opposed to other chemical synthesis routes (e.g. molecular-level mixing). A thorough literature review about the use of CNT in MMCs is beyond the scope of this manuscript and can be found in Ref. [20] and the references therein.

As previously demonstrated [21], the particle distribution homogenization in MMCs is achievable using high pressure torsion (HPT), which is essential in the case of CNT, given their predisposition to form agglomerates due to van der Waals interactions. The homogeneous distribution of the particles within the matrix in MMCs is very important to avoid anisotropic behavior during mechanical loading. Additionally, in the case of CNT-reinforced composites, it is also of paramount importance that the CNT keep their microstructural features as unaltered as possible after processing. This would ensure to some extent that the CNT will retain their
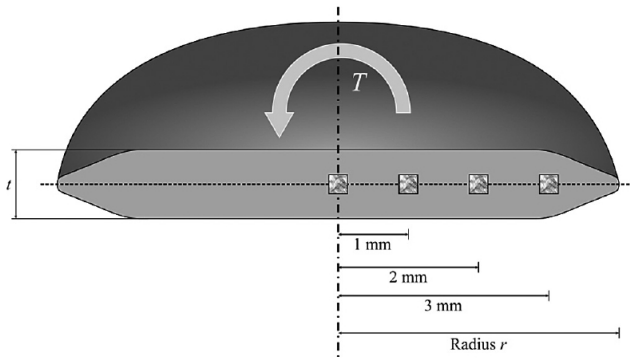
Fig. 1. Schematic view of the measurement positions in the cross section of the composites.

is extended (in the best cases) to an observation of the so-called defect index (I_D/I_G) [17,25,26], which would not present a full overview of the structural state. Specifically, Tokunaga and co-workers [25] studied the HPT deformation of CNT-reinforced Al composites at 2.5 GPa and 30 turns. They report that there is an increased D-band intensity due to structural damage generated by bending and/or breaking of the CNT. However, by analyzing the presented Raman spectra, an increase in the G-band width and a strong upshifting is clearly noticeable. This might indicate a possible amorphization of the graphitic structure. This was also observed in Ref. [26], even after the pre-processing, but was not discussed. In this case, the authors only focus on a brief analysis of the I_D/I_G ratio. Thus, in light of the available literature, a thorough study of the influence of HPT on the CNT structure becomes very important.

In the present work, we obtained CNT-reinforced nickel matrix composites via HPT, and evaluated the influence of the processing parameters on the nanotubes structural state for different CNT weight fractions. These composites were sintered by means of hot uniaxial pressing (HUP) and afterwards subjected to HPT at room temperature using different number of turns (T) applying a pressure of 4 GPa.

physical properties and could avoid chemical interactions with the metallic matrix. These chemical interactions are detrimental to the mechanical performance, since they generate brittle phases (i.e. carbides) which stem from the degradation of the C-containing phase. Even though some authors correctly state that the presence of carbides enhance the interface in composites, this would be a detrimental feature in two ways. First, the aforementioned brittle interface might crack after applying a certain stress, thus rendering the load transfer negligible. Second, by degrading the CNT, their intrinsic physical properties are severely compromised. Therefore, a processing route in which the structural state of the CNT is retained and a seamless interface with the matrix is achieved becomes extremely important.

Different kind of defects (e.g. point defects or dangling bonds) can be present in CNT after highly energetic processes such as ball milling [22–24], which can lead to interaction between the CNT and the matrix. In the same way, seeking the refinement of the microstructure by means of HPT, the samples can be subjected simultaneously to high pressures and high strains, and although the CNT are surrounded by the softer matrix and can −to some extent− be protected by it, they might be degraded during the processing. It is widely recognized that Raman spectroscopy is a very powerful and versatile technique for the characterization of carbon-based materials. By analyzing the change of certain characteristic bands of sp^2 carbons (D, G and G′ bands and their intensity ratios) and certain descriptive features (peak central position and full width at half maximum − FWHM, Γ − of the G band), it is possible to obtain a fairly accurate picture of the structural state of the carbonaceous phase. To the best of our understanding, there are no thorough studies of the damage suffered by CNT after SPD using Raman Spectroscopy. Though certain reports present Raman spectra of deformed composites, the analysis

2. Experimental

2.1. Manufacturing and HPT processing of CNT/Ni composites

Different CNT weight fractions were analyzed, namely: 0.5 wt.% (2.4 vol.%), 1 wt.% (4.7 vol.%), and 2 wt.% (9 vol.%), the latter being the maximum reasonable amount of CNT to be used in CNT/Ni composites as determined in previous studies [12]. The manufacturing of the composites started with the dispersion of multi-wall carbon nanotubes (MWCNT) (CCVD grown, Graphene Supermarket, USA. Density 1.84 g/cm^3, diameter: 50−85 nm, length: 10−15 µm, carbon purity: >94%) in ethylene glycol EG (MWCNT/EG concentration ratio at 0.2 mg/ml). Afterwards, a mixture with nickel dendritic powder (Alfa Aesar, Mesh 325 (45 µm), density 8.91 g/cm^3) was produced by means of a homogenizer (WiseTis, Witeg) to disperse the larger agglomerates, and an ultrasonic bath (Sonorex Super RK 514 BH, Bandelin, 860 W, 35 kHz) to disperse the smaller ones. The dispersion was performed following the process described in Ref. [27]. The solvent was evaporated in a ventilated furnace at 150 °C and the powder was carefully grinded using an agate mortar to obtain more uniformly distributed particles and therefore to ease the compaction of the green pellets (990 MPa). After the densification process at 750 °C in vacuum (2 × 10^{-6} mbar) for 2.5 h, using a hot uniaxial press (264 MPa), the resulting samples with different compositions were subjected to HPT at room temperature using different number of
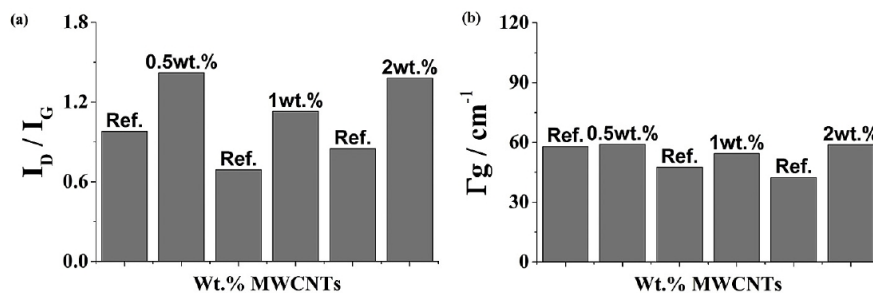

Fig. 2. Effect of the applied Pressure during HPT (taken at the center of the sample, $\varepsilon_{vM} = 0$) after 1 turn. (a) Defect index I_D/I_G and, (b) full width at half maximum (FWHM) of the G band.

Table 1
Mean CNT agglomerate sizes in the as-sintered (initial) and post-deformation (final) state for a subset of samples measured at the center of the sample.

Sample	Initial agglomerate size/μm	Final agglomerate size/μm
1 wt.%_1T_4 GPa	4.1 ± 1.5	0.8 ± 0.3
1 wt.%_1T_7 GPa		0.4 ± 0.2
2 wt.%_1T_4 GPa	6.6 ± 2.4	0.4 ± 0.2
2 wt.%_1T_7 GPa		0.3 ± 0.1

turns (T = 1, 4, 10 and 20) applying 4 GPa of pressure. An additional set of samples with 1 wt.% and 2 wt.% were processed in HPT using 1 rotation, 4 GPa and 7 GPa, in order to evaluate the effect of pressure on the damage. Raman measurements were performed in the center of the samples, where no deformation caused by strain should take place, in order to analyze the effect of the pressure subjected to the MWCNT.

The samples were cut in halves and embedded using conductive resin. All the analyses were carried out along the radial direction (Fig. 1). The shear strain in HPT is calculated by:

$$\gamma = \frac{2\pi T}{t} r \qquad (1)$$

where T is the number of revolutions, r is the distance from the center of the rotation axis and t is the thickness of the sample. If one assumes a von Mises yield locus [28], the equivalent strain applied in HPT can be calculated by:

$$\varepsilon_{vM} = \frac{2\pi T}{\sqrt{3}\, t} r \qquad (2)$$

The sample diameter was 8 mm in all cases and the thickness varied from 0.6 mm to 1 mm, so the equivalent strain was specifically calculated for each sample radius.

2.2. Structural characterization of the CNT

Raman spectra were acquired with an InVia™ Raman spectrometer (Renishaw) using a 2400 lines/mm grating and an Nd:YAG laser with an excitation wavelength of 532 nm (2.33 eV) through a 50× objective (numerical aperture of 0.9) with a spectral resolution of 1.2 cm^{-1}. Each spectrum is the average of 3 measurements performed on the same spot (spot size of 3 μm). Measurements along the radii were carried out every 1 mm in order to visualize the evolution of the data along the middle plane and the results were compared to those of the reference samples in the "as sintered" condition. Following the analysis proposed by N. Souza et al. [29], it was confirmed that no laser-induced modification of the CNT occurs up to a laser power of 0.5 mW. According to this, the laser power was set for all the measurements to 0.2 mW. Information

about the height of the G, D and G′ bands were taken directly from the normalized data and their ratios were computed and plotted against the corresponding equivalent strain values. A Lorentzian fit of the spectra was used in order to get information about position of the G-band as well as its full width at half maximum. The analysis was carried out by studying the evolution of different descriptive parameters such as the full width at half maximum of the G band Γ_G (crystallinity-related), I_D/I_G ratio (defect-related), and the G band position (amorphization-stage related). In all the cases, the data was recorded along the middle plane in order to avoid the effect of the microstructural gradients along the height of the specimens on the results, as shown in Fig. 1 [30].

3. Results and discussion

The microstructural refinement of these composites was studied and reported elsewhere [31]. During HPT, a pronounced microstructural refinement takes place, which implies that the CNT present in the composites also may undergo strong deformations during processing.

All the results indicate that the larger variations of the Raman parameters occur during the early stages of processing, where the application of high compressive loads takes place. This can be observed in all the cases, when comparing the results to those of the reference samples.

Fig. 2 shows some qualitative markers of the CNT structural state that are influenced mainly by the applied pressure during HPT. According to Equation (2), the measurements taken at the center of the sample (r = 0) would not present accumulated von Mises strain (ε_{vM} = 0). By studying the case for 1 wt.% and 2 wt.% samples, it becomes evident that the application of pressure increases the structural disorder in the CNT (Fig. 2a). Additionally, the peak width is also increased, indicating a reduction in the crystallinity (Fig. 2b). The broadening of the G band indicates a reduction in the resonance-induced vibration extinction time [32], meaning that there is either a rise in the amount of structural defects, a shortening of the CNT or a combination thereof.

Concerning the CNT agglomerate size, a significant reduction in size is clearly noticeable as shown in Table 1. The change in the mean agglomerate size shows a drop of one order of magnitude after only one turn in HPT. The values stay in the sub-micron range, which might be more useful when a dispersion-strengthening effect is needed, as opposed to the as-sintered state with μm-ranged clusters. As an example (Fig. 3), the deformation induced by a 20 turns HPT processing rendered a more homogeneous and finer CNT cluster distribution throughout the metallic matrix. This has been already reported for hard, ceramic particles in soft metallic matrices [21].

When applying high compressive loads, a relative gliding between adjacent CNT within the agglomerates takes place. This
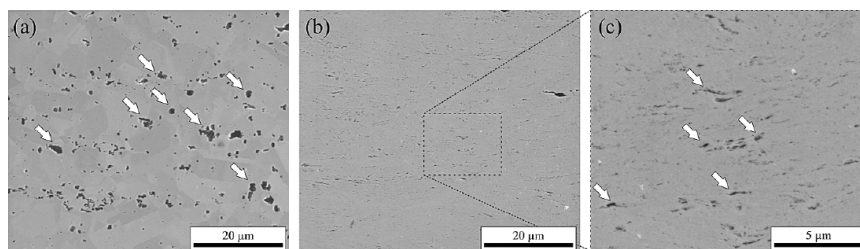

Fig. 3. Electron micrographs of a 1 wt.% CNT composite (a) at the undeformed initial state and (b) after 20 turns of deformation, taken at 3 mm from the center. (c) Magnification of a region of interest. As a guide, the white arrows indicate some regions with CNT agglomerates (this type of composites encloses the CNT in the cavities as observed by EDX, not shown here). The reduction of the mean agglomerate size is clearly noticeable.
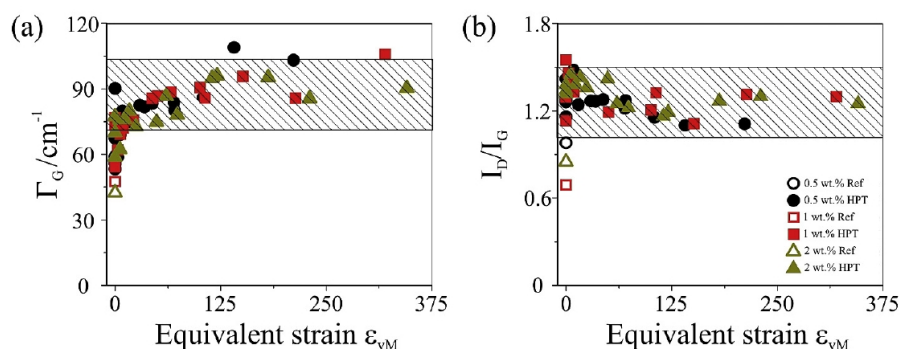
Fig. 4. (a) Evolution of Γ_G as a function of the equivalent strain for different processing conditions. (b) Variation of the I_D/I_G ratio with increasing equivalent strain. (A colour version of this figure can be viewed online.)

derives in a significant reduction in the cluster size and a better detachment of the impurities when applying higher compressive loads (7 GPa). This is confirmed by these results, where the 7 GPa processed samples present a smaller mean agglomerate size than those processed with 4 GPa. This feature adds a significantly practical solution to a prevalent complication in the manufacturing of CNT-reinforced metal matrix composites, where agglomeration is one of the major concerns towards practical applicability.

3.1. Effect of the accumulated strain (at 4 GPa)

The study of the effect of accumulated strain on the CNT has been approached by analysing three different indicators (Γ_G, I_D/I_G ratio and G band position) within an equivalent strain range of $\varepsilon_{vM} = 0$ 375.

The crystallinity-related index Γ_G shows a constant increase in its value in all cases (Fig. 4a), indicating an increase in amorphization of the nanotubes. Interestingly, all samples show a saturation in the broadening at approximately 90 cm^{-1} at high deformation grades. This indicates a greater structural disorder and a likely shortening of the CNT, as explained before. Furthermore, it is evident that the broadening happens during the early stages of deformation ($\varepsilon_{vM} < 5$). This is related to the fact that, as the agglomerates are detached and new smaller agglomerates appear, the load is distributed among a larger number of clusters. Thus, the effective pressure applied on each of the agglomerates would be higher when a higher amount of agglomerates is present.

This is in agreement with the I_D/I_G results (Fig. 4b), where the index seems to remain constant in all the cases with the values lying between 1 and 1.5. Again, this quasi steady state is reached at quite low accumulated equivalent strain and remains, to some extent, within the same magnitude. That means that the higher amount of damage is produced at early stages. Since the data do not change significantly after the initial stages of deformation, an extra parameter must be included in the analysis to differentiate the structural disorder. In this case, the examination of the evolution of the G band position would provide a better approach to the identification of the potential amorphization of the sp^2 structure. Ferrari and Robertson [33] proposed a straightforward method to evaluate the damage in carbonaceous structures by observing the up and downshifting of the G band. Carbon materials undergo an amorphization trajectory depending on the clustering of the sp^2 phase, the bond disorder, the presence of sp^2 rings or chains and the sp^2/sp^3 ratio [32]. These changes can be tracked and analyzed from the variations in the Raman spectra (i.e. relative intensities, broadening and position shifts of the main peaks). The model consists of three stages, describing the transition from a graphitic to a predominantly sp^3 hybridized material. In the first stage, the main structural change is the alteration from a monocrystalline to a polycrystalline phase. Characteristically, the G band presents an upshift to larger wavenumbers (up to 1600 cm^{-1}). This upshift is actually a convolution between the original G band (approx. 1580 cm^{-1}) and the D$'$ band (approx. 1620 cm^{-1}). The second stage comprises a decrease of the G band position towards values around 1510 cm^{-1}, and is related to the accumulation of introduced defects in the graphitic lattice, deriving in a softening of the phonon modes.

Fig. 5 shows exemplarily the deconvolution of the upshifted G band for the pristine CNT (Fig. 5a) and in the case of CNT in a highly deformed sample (Fig. 5b). The resulting peak is a convolution of two bands, namely: the G band at 1580 cm^{-1} and the D$'$ band at
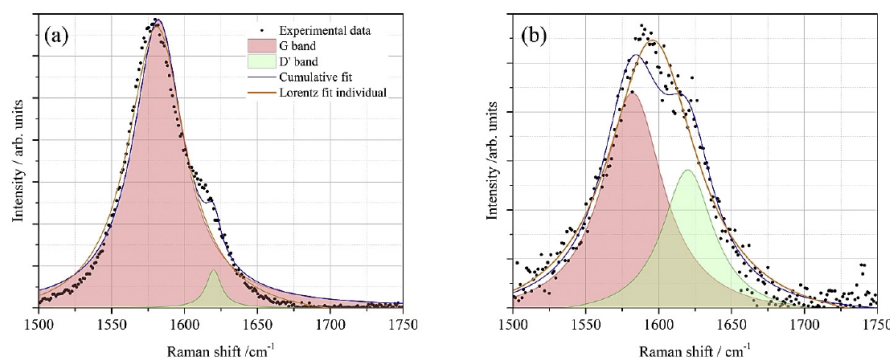

Fig. 5. Example of the deconvolution of the G band in (a) pristine CNT and (b) 0.5 wt.% CNT sample deformed to an equivalent strain of $\varepsilon_{vM} = 195$. (A colour version of this figure can be viewed online.)

0.5 wt.% 4 GPa
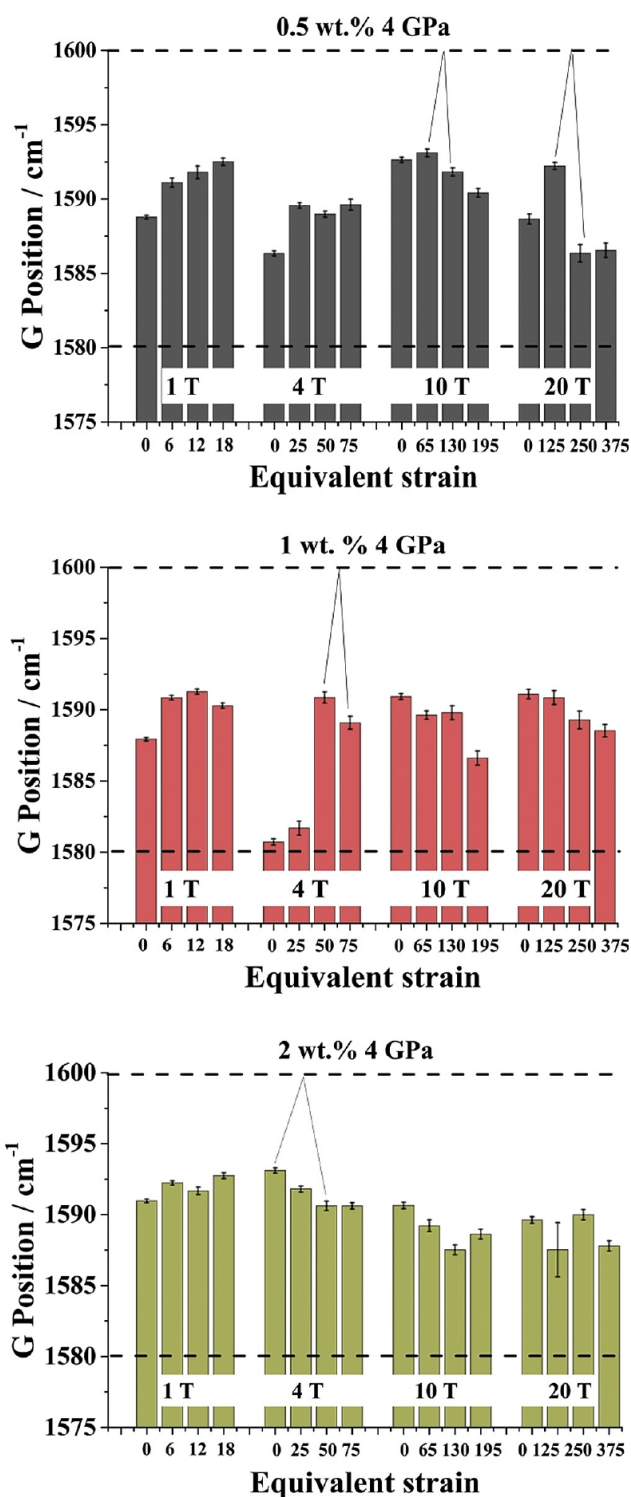

1 wt. % 4 GPa

2 wt.% 4 GPa

Fig. 6. Variation of G peak position as a function of the equivalent von Mises strain for the different evaluated CNT concentrations. The dashed lines indicate the lower and upper bounds of the first stage in Ferrari's model. (A colour version of this figure can be viewed online.)
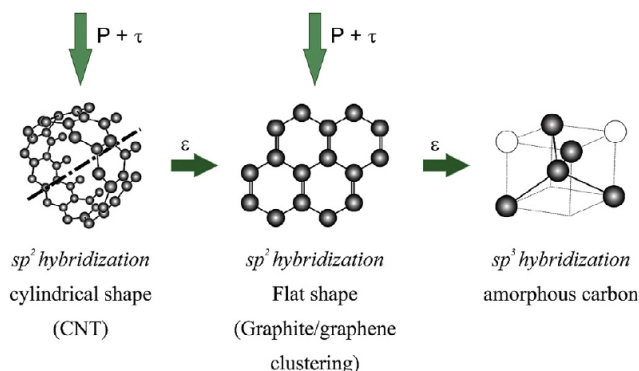

Fig. 7. Representation of the different stages of the amorphization trajectory that sp[2] carbons can undergo. (A colour version of this figure can be viewed online.)

1620 cm^{-1} [33]. It is evident that the upshifting is due to an increase in the intensity of the D′ band, which is related to the reduction in the crystallite size of the CNT [33].

Fig. 6 shows the position of the G band for the different samples as a function of the deformation degree. The low CNT-containing samples (0.5 wt.% CNT) show a clear upshifting trend for low deformations, whereas at higher deformation, an inflection point is identifiable. This turning point is located between a von Mises strain of 65 and 130 for 10 turns and between 125 and 250 for 20 turns. In the case of the higher CNT concentrations, the transition occurs at earlier stages of deformation. Specifically, the 1 wt.% samples go through the transition at von Mises strains as low as 50, whereas the 2 wt.% samples show the inflection point at an $\varepsilon_{vM} = 25$. This is evidently related to the amount of available CNT that are subjected to the strain and their distribution. In the case of lower concentrations, the matrix predominantly absorbs the deformation energy, as opposed to the case in which a broad distribution of CNT renders them more vulnerable to the strain.

In spite of the fact that the CNT undergo an amorphization trajectory as indicated in Fig. 6, the G band does not shift to values lower than 1580 cm^{-1}, which means that, according to the aforementioned model proposed by Ferrari et al. and, in the worst case, the nanotubes are at the late periods of the model's first stage.

Concerning the damage mechanisms, it is well known that HPT processing acts on the microstructure of the metallic matrix by inducing large amounts of geometrically necessary dislocations (GND). Since the CNT are placed at the grain boundaries and act as non-coherent bodies with the matrix, the likely strengthening mechanisms would be Orowan looping and grain boundary strengthening [12,19,34]. That means that the GND would round up the second phases, without directly interacting with them. Thus, the most likely damage mechanism acting on the CNT is the matrix plastic flow. Since the CNT are subjected to a strong axial pressure and a shearing movement, it is highly likely that after a certain deformation, the weak structural points of the CNT (structural defects) no longer resist the induced strain and break. The consecution of deformation and breaking of the nanotubes activates the aforementioned amorphization trajectory, sequentially damaging the structure as schematically shown in Fig. 7. Regarding the practical implications of this issue, the fact of having shorter CNT would imply a reduction in the effective load transfer area, which can be detrimental to the mechanical properties of the composites.

Summarizing, after a thorough analysis aided by Raman spectroscopy, it is evident that the carbon nanotubes are strongly affected by the applied strain during deformation, independent of their relative amount in a composite material. It is then evident that an analysis based solely on the well-known defect index (I_D/I_G) is

insufficient and, for a proper identification of the processing limits, a complementary analysis considering the G band peak width and position is of great importance.

Finally, it has been shown that the processing at room temperature of this type of composites by HPT is possible to a certain extent (defined by the degradation of the nanotubes). The distribution of the agglomerates is improved and a reduction in the mean agglomerate size is achieved. This reduction might play a very important role in the thermal stabilization of the microstructure and subsequently, in the mechanical performance of the composites.

4. Conclusions

We have shown that, even though HPT is a useful technique when it comes to the improvement of the distribution of CNT agglomerates in metal matrix composites, it induces irreversible damage on the CNT. In this study, we tracked the defects on the CNT from the *as-sintered* to the *as-deformed* condition for different CNT concentrations and different degrees of deformation. We concluded that the apparent maximum damage, as shown by the evolution of the different Raman parameters here studied and the shifting of the G band, is reached already at early stages of the deformation process, and occurs before the saturation in the microstructural refinement is reached. Specifically, for high CNT concentrations it can start even at a von Mises strain of 25. Furthermore, we were able to correlate the damage mechanism to a well-established carbon amorphization trajectory proposed in the literature. Finally, this study demonstrates that, in order to reliably characterize and track the mechanically induced damage in nanocarbons, the widely used I_D/I_G ratio is not sufficient.

Acknowledgements

References

[1]   C. He, N. Zhao, C. Shi, X. Du, J. Li, H. Li, et al., An approach to obtaining homogeneously dispersed carbon nanotubes in Al powders for preparing reinforced Al-Matrix composites, Adv. Mater. 19 (2007) 1128–1132.

[2]   T. Laha, Y. Chen, D. Lahiri, A. Agarwal, Tensile properties of carbon nanotube reinforced aluminum nanocomposite fabricated by plasma spray forming, Compos A 40 (2009) 589–594.

[3]   T. Laha, A. Agarwal, T. Mckechnie, S. Seal, Synthesis and characterization of plasma spray formed carbon nanotube reinforced aluminum composite, Mater Sci. Eng. A 381 (2004) 249–258.

[4]   K. Balani, S.R. Bakshi, Y. Chen, T. Laha, A. Agarwal, Role of powder treatment and carbon nanotube dispersion in the fracture toughening of plasma-sprayed aluminum oxide-carbon nanotube nanocomposite, J. Nanosci. Nanotechnol. 7 (2007) 3553–3562.

[5]   T. Kuzumaki, K. Miyazawa, H. Ichinose, K. Ito, Processing of carbon nanotube reinforced aluminum composite, J. Mater Res. 13 (1998) 2445–2449.

[6]   S.I. Cha, K.T. Kim, S.N. Arshad, C.B. Mo, S.H. Hong, Extraordinary strengthening effect of carbon nanotubes in metal-matrix nanocomposites processed by molecular-level mixing, Adv. Mater. 17 (2005) 1377–1381.

[7]   M. Yu, O. Lourie, M.J. Dyer, K. Moloni, T.F. Kelly, R.S. Ruoff, Strength and breaking mechanism of multiwalled carbon nanotubes under tensile load, Science 287 (2000) 637–640.

[8]   S.R. Bakshi, A. Agarwal, An analysis of the factors affecting strengthening in carbon nanotube reinforced aluminum composites, Carbon 49 (2011)

533–544.

[9]   S.R. Dong, J.P. Tu, X.B. Zhang, An investigation of the sliding wear behavior of Cu-matrix composite reinforced by carbon nanotubes, Mater Sci. Eng. A 313 (2001) 83–87.

[10] K. Tae, S. Il, S. Hyeon, S. Hyung, Microstructures and tensile behavior of carbon nanotube reinforced Cu matrix nanocomposites, Mater. Sci. Eng. A 430 (2006) 27–33.

[11] K.T. Kim, K.H. Lee, S Il Cha, C.-B. Mo, S.H. Hong, Characterization of carbon Nanotubes/Cu nanocomposites processed by using nano-sized Cu powders, MRS Proc. (2004) 821.

[12] S. Suarez, F. Lasserre, F. Mücklich, Mechanical properties of MWNT/Ni bulk composites: influence of the microstructural refinement on the hardness, Mater. Sci. Eng. A 587 (2013) 381–386.

[13] T. Borkar, J. Hwang, J.Y. Hwang, T.W. Scharf, J. Tiley, S.H. Hong, et al., Strength versus ductility in carbon nanotube reinforced nickel matrix nanocomposites, J. Mater. Res. 29 (2014) 761–769.

[14] J. Nguyen, T.B. Holland, H. Wen, M. Fraga, A. Mukherjee, E. Lavernia, Mechanical behavior of ultrafine-grained Ni–carbon nanotube composite, J. Mater. Sci. 49 (2013) 2070–2077.

[15] Y.S. Jeon, J.Y. Byun, T.S. Oh, Electrodeposition and mechanical properties of Ni − carbon nanotube nanocomposite coatings, J. Phys. Chem. Sol. 69 (2008) 1391–1394.

[16] W. Salas, L.E. Murr, Explosive shock-wave consolidation of aluminum powder/ carbon nanotube aggregate Mixtures : optical and Electron metallography, Met. Mater. Trans. A 38A (2007) 2928–2935.

[17] S. Suarez, F. Lasserre, F. Soldera, R. Pippan, F. Mücklich, Microstructural thermal stability of CNT-reinforced composites processed by severe plastic deformation, Mater. Sci. Eng. A 626 (2015) 122–127.

[18] P. Jenei, J. Gubicza, E.Y. Yoon, H.S. Kim, J.L. Lábár, High temperature thermal stability of pure copper and copper–carbon nanotube composites consolidated by High Pressure Torsion, Compos Part A Appl. Sci. Manuf. 51 (2013) 71–79.

[19] S. Suárez, E. Ramos-Moore, B. Lechthaler, F. Mücklich, Grain growth analysis of multiwalled carbon nanotube-reinforced bulk Ni composites, Carbon 70 (2014) 173–178.

[20] S. Suárez, L. Reinert, F. Mücklich, Carbon nanotube (CNT) -reinforced metal matrix bulk composites: manufacturing and evaluation, in: M. Aliofkhazraei (Ed.), Diam. Carbon Compos. Nanocomposites, first ed., InTech, 2016, p. 180.

[21] I. Sabirov, O. Kolednik, R. Pippan, Homogenization of metal matrix composites by high-pressure torsion, Metall. Mater. Trans. A 36 (2005) 2861.

[22] K.S. Munir, M. Qian, Y. Li, D.T. Oldfield, P. Kingshott, D.M. Zhu, et al., Quantitative analyses of MWCNT-Ti powder mixtures using Raman spectroscopy: the influence of milling parameters on nanostructural evolution, Adv. Eng. Mater. 17 (2015) 1660–1669.

[23] F. Ostovan, K. Matori, M. Toozandehjani, A. Oskoueian, H. Yusoff, R. Yunus, et al., Nanomechanical behavior of multi-walled carbon nanotubes particulate reinforced aluminum nanocomposites prepared by ball milling, Materials 9 (2016) 140.

[24] M.S.S. Saravanan, S.P.K. Babu, Synthesis, characterization, and ECAP consolidation of carbon nanotube reinforced AA 4032 nanocrystalline composites produced by high energy ball milling, J. Eng. Mat. Tech. 137 (2015) 1–9.

[25] T. Tokunaga, K. Kaneko, Z. Horita, Production of aluminum-matrix carbon nanotube composite using high pressure torsion, Mater. Sci. Eng. A 490 (2008) 300–304.

[26] H. Asgharzadeh, S.-H. Joo, H.S. Kim, Consolidation of carbon nanotube reinforced aluminum matrix composites by high-pressure torsion, Metall. Mater. Trans. A 45 (2014) 4129–4137.

[27] L. Reinert, M. Zeiger, S. Suárez, V. Presser, F. Mücklich, Dispersion analysis of carbon nanotubes, carbon onions, and nanodiamonds for their application as reinforcement phase in nickel metal matrix composites, RSC Adv. 5 (2015) 95149–95159.

[28] H.P. Stüwe, Equivalent strains in severe plastic deformation, Adv. Eng. Mater. (2003) 291–295.

[29] N. Souza, M. Zeiger, V. Presser, F. Mücklich, In situ tracking of defect healing and purification of single-wall carbon nanotubes with laser radiation by time-resolved Raman spectroscopy, RSC Adv. 5 (2015) 62149–62159.

[30] A. Hohenwarter, A. Bachmaier, B. Gludovatz, S. Scheriau, R. Pippan, Technical parameters affecting grain refinement by high pressure torsion, Int. J. Mater. Res. 100 (2009) 1653–1661.

[31] A. Katzensteiner, K. Aristizabal, S. Suarez, R. Pippan, A. Bachmaier, Temperature dependent structural evolution in nickel/carbon nanotube composites processed by high-pressure torsion, IOP Conf. Ser. Mat. Sci. Eng. 194 (2017) 012019.

[32] S. Suarez, F. Lasserre, O. Prat, F. Mücklich, Processing and interfacial reaction evaluation in MWCNT/Ni composites, Phys. Status Solidi A 211 (2014) 1555–1561.

[33] A. Ferrari, J. Robertson, Interpretation of Raman spectra of disordered and amorphous carbon, Phys. Rev. B 61 (2000) 14095–14107.

[34] L. Reinert, S. Suarez, T. Müller, F. Mücklich, Carbon nanoparticle-reinforced metal matrix composites: microstructural tailoring and predictive modeling, Adv. Eng. Mater. 19 (2017) 1600750.

III. On the reinforcement homogenization in CNT/metal matrix composites during severe plastic deformation

Katherine Aristizabal[1], Andreas Katzensteiner[2], Andrea Bachmaier[2], Frank Mücklich[1], Sebastián Suárez[1]

1 Department of Material Science and Engineering, Saarland University,
66123 Saarbrücken, Germany
2 Erich Schmid Institute, Austrian Academy of Sciences, Jahnstrasse 12, 8700 Leoben, Austria

Own Contribution: Project management, sample manufacturing and processing, experimental execution, data analysis, conceptualization of experimental results and calculations, manuscript writing.

Abstract:

Carbon nanotube (CNT)-reinforced nickel matrix composites with different concentrations were processed by high pressure torsion (HPT). We thoroughly characterized the CNT agglomerates' spatial arrangement at different stages of deformation in order to extract information valuable for the optimization of the processing parameters and to elucidate the mechanisms involved during the processing of particle reinforced metal matrix composites by HPT. From the electron micrographs taken on the radial direction with increasing equivalent strains, we observed that CNT agglomerates debond by relative sliding between

CNT during HPT, becoming spherical at higher stages of deformation. Furthermore, we introduced a model for the prediction of the minimum strain required for a homogeneous distribution of a second phase during HPT, which can be correlated to the material's three-dimensional structure and agrees well with the experimental data.

On the reinforcement homogenization in CNT/metal matrix composites during severe plastic deformation

Katherine Aristizabal[a,*], Andreas Katzensteiner[b], Andrea Bachmaier[b], Frank Mücklich[a], Sebastian Suárez[a]

[a] *Chair of Functional Materials, Department of Materials Science, Saarland University, Campus 66123, Saarbrücken, Germany*
[b] *Erich Schmid Institute of Materials Science, Austrian Academy of Sciences, Jahnstrasse 12, A-8700 Leoben, Austria*

ARTICLE INFO

ABSTRACT

Carbon nanotube (CNT)-reinforced nickel matrix composites with different concentrations were processed by high pressure torsion (HPT). We thoroughly characterized the CNT agglomerates' spatial arrangement at different stages of deformation in order to extract information valuable for the optimization of the processing parameters and to elucidate the mechanisms involved during the processing of particle reinforced metal matrix composites by HPT. From the electron micrographs taken on the radial direction with increasing equivalent strains, we observed that CNT agglomerates debond by relative sliding between CNT during HPT, becoming spherical at higher stages of deformation. Furthermore, we introduced a model for the prediction of the minimum strain required for a homogeneous distribution of a second phase during HPT, which can be correlated to the material's three-dimensional structure and agrees well with the experimental data.

1. Introduction

The distribution of reinforcing phases in composite materials is of great importance and has a big influence on their mechanical performance. Carbon nanotubes have been widely used as reinforcing phase not only in polymer [1,2] and ceramic matrix composites [3,4] but also in metal matrix composites [5–7]. Some authors have explored different strategies for improving the distribution of CNT in MMC such as blending by mixing, nano-scale dispersion, ball milling, cold spraying and molecular-level mixing [6,8,9] However, blending by mixing has been found to deteriorate the mechanical properties of the composites due to poor distribution of the CNT. Although nano-scale dispersion was found to improve significantly the distribution of the CNT in Aluminum matrix, because it consist in utilizing natural rubber in a mixture with the CNT and the metallic powder alternatively stacked in a preform, it needs to be subjected to high temperatures (800 °C) in order to burn the rubber and to melt the metal, which would imply the use of even higher temperatures in the case of nickel, which has a melting point of 1455 °C, adding further difficulties to the manufacturing process. Ball milling and molecular-level mixing methods also improve significantly the dispersion of the CNT, both producing large agglomerates' sizes of about some microns to some millimeters. Ball milling also results in severe damage to the CNT. A thorough discussion of the advantages and drawbacks of each technique is beyond the scope of this

manuscript and can be found in [6] and the references therein. Therefore, given their tendency to form agglomerates due to Van der Waals forces, a homogeneous distribution of CNT is still a challenging task.

High-pressure torsion, a severe plastic deformation process, has shown to be a powerful tool for improving the distribution of particles in MMC. I. Sabirov et al., showed how ceramic particles are reduced in size and dispersed inside the metallic matrix by debonding [10]. During HPT, the sample is placed between two anvils using high pressures (> 2 GPa) and rotated in quasi-constrained conditions a certain number of turns (T). By the action of plastic flow and the generation, mobility and re-arrangement of dislocations, a refinement of the microstructure takes place and the strength of the material increases with increasing strain until the saturation in the microstructural refinement is reached [11]. Nevertheless, these microstructures possess high stored energy in their large grain boundary area. Recently, based on their ability to pin the microstructure [5], CNT have been used as stabilizing phase against grain growth [12,13] in MMC processed by severe plastic deformation. However, in order to efficiently fulfill their stabilization task, CNT should be homogeneously distributed [14], which is also expected to increase the mechanical performance of these MMC. For that purpose, the processing route used in this work started by colloidal mixing of the CNT with the metallic Nickel powder, followed by the cold pressing and hot sintering of the blends and succeeding processing

---

by means of high pressure torsion.

For qualitative assessment of the distribution, directly observation of electron micrographs is sufficient. Previously, a preliminary assessment of the reinforcement homogeneity in CNT/Ni MMC was carried out [15]. In the present study the aim is to extract quantitative information from the electron micrographs on the CNT agglomerate size and spatial distribution in MMC subjected to severe plastic deformation, and correlate it to the mechanisms involved in the deformation of the reinforcement during processing, seeking the optimization of the process parameters and the improvement of the physical properties of the composites. Some quantitative methods on the evaluation of the dispersion and distribution of CNT in MMC have been proposed in the literature [16–19]. A thorough discussion of the different quantification methods can be found elsewhere [20]. Furthermore, event-to-event (nearest neighbor distance NND), based methods, commonly used in spatial statistics, have been used in unidirectional composites [21]. Moreover, the method of Region Homogeneity H_{RO} has been proposed as an easy way of assessing the distribution homogeneity of second phases in metallic materials [22] and also of CNT agglomerates in MMC [23]. The advantages and limitations of the latter in the evaluation of MMC processed by SPD are discussed here.

In this work, an extensive clustering and distribution homogeneity analysis was performed with the aim of understanding the behavior of the CNT during the deformation process as a function of the accumulated deformation. For the evaluation of the studied composites' homogeneity, a NND clustering analysis-based methodology is used, which can be completely carried out using open source software [24,25]. From the electron micrographs, a CNT agglomerate-debonding mechanism by relative sliding between CNT during HPT is observed, which contributes to the understanding of the reinforcement arrangement after the processing by severe plastic deformation of CNT MMC. Finally, a model for the prediction of the minimum equivalent strain that should be applied during HPT for a homogenous distribution of particles in MMC is proposed, which provides a basis for the optimization of the processing parameters.

2. Experimental

2.1. Manufacturing and HPT Processing of CNT/Ni Composites

The composites were obtained via powder metallurgy and further processed by HPT. The starting materials were MWCNT (CCVD grown, Graphene Supermarket, USA density 1.84 g/cm^3, diameter: 50–85 nm, length: 10–15 μm, carbon purity: > 94%) and dendritic Ni powder (Alfa Aesar, mesh − 325). A colloidal mixing process was used to blend the precursor powders by which CNT are dispersed in ethylene glycol EG (CNT/EG concentration ratio at 0.2 mg/ml) and mixed with Ni powder. A thorough description of this process is reported elsewhere [26]. The CNT fractions used were 0.5, 1, 2 and 3 wt% (2.4, 4.7, 9 and 13 vol%, respectively). The powders were dried and cold pressed under 990 MPa and subsequently sintered in a hot uniaxial press HUP under vacuum (2 × 10^{-6} mbar) at 750 °C for 2.5 h with a 264 MPa axial pressure. Sintered samples were further processed by means of HPT at room temperature using 1, 4, 10 and 20 T under 4 GPa of pressure. Samples with 1 wt% CNT were processed 30 T at room temperature RT and at 200 °C, were also analyzed. Fig. 1 shows schematically the HPT set up.

2.2. Characterization

The HPT samples were cut in halves, embedded in conductive resin and fine polished using polishing discs with the aid of 6, 3 and 1 μm diamond suspensions and finally with OPS colloidal silica. The samples were then characterized by scanning electron microscopy (SEM) using a Helios NanoLab™ 600 dual beam field emission microscope (FEI Company). The analysis of the microstructure was carried out along the
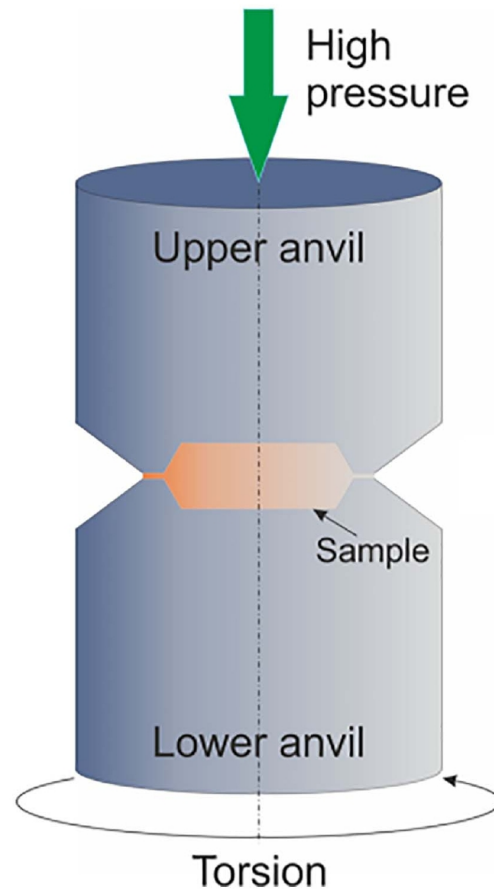

Fig. 1. Schematic HPT set up used for sample processing.

middle plane, in order to avoid the effect of the microstructural gradients along the height of the specimens [27]. The images were taken every 1 mm with a resolution of 12.5 nm per pixel along the radial direction, corresponding to increasing equivalent strain values, according to $\varepsilon_{eq} = \frac{2\pi Tr}{t\sqrt{3}}$, where T is the number of turns, t is the sample thickness and r the distance from the center of the sample [28]. In the case of HPT samples, the micrographs were acquired at 10 kX magnification, resulting in a field of view of (12.8 × 12.8) μm^2. The choice was made based on the size of the agglomerates: if the images were to be taken at lower magnifications, information about the smaller agglomerates in the case of the highly deformed samples would be lost due to resolution issues. On the other hand, at higher magnifications the larger agglomerates would be also neglected, since they would hardly fit into the region of interest. Furthermore, the size was kept constant for comparison purposes.

The images were digitally binarised and analyzed using the image processing package FIJI [24]. Micrographs with corresponding binary images are shown exemplarily in Fig. 2. The CNT agglomerates were considered as compact particles and a thorough particle analysis was performed on each image. The particle analysis protocol was as follows: the images were calibrated with the known scale; the threshold was adjusted thoroughly, in order to separate the dark (CNT agglomerates) from the light regions (Ni matrix), without removing pixels from the boundaries (manual segmentation was performed when necessary) and finally, the images were made binary. Different size descriptors (such as the area, the maximum and minimum Feret diameter and the perimeter) and shape factors (such as roundness, circularity, aspect ratio etc.) can be obtained during particle analysis. In this case, the particle
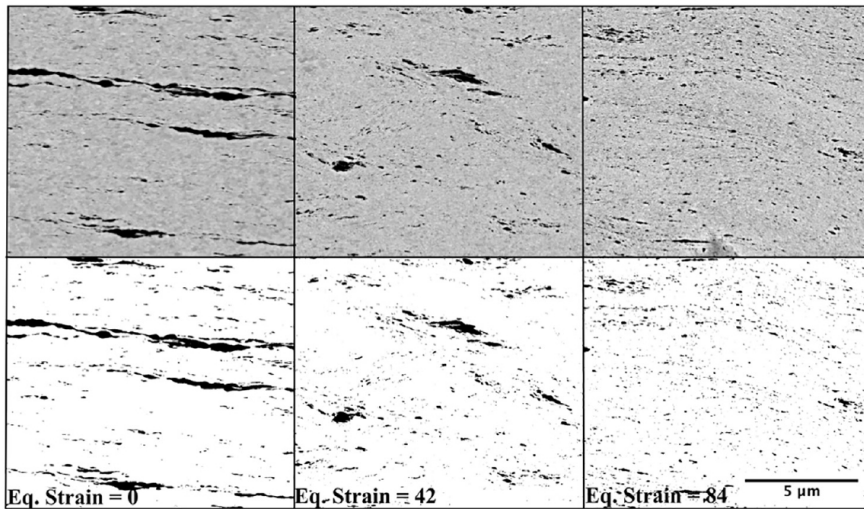
Fig. 2. Electron micrographs (upper row) and their respective binarized images (lower row) from a 1 wt% sample after 10 turns. The equivalent strain increases from left to right. The dark regions correspond to CNT agglomerates.
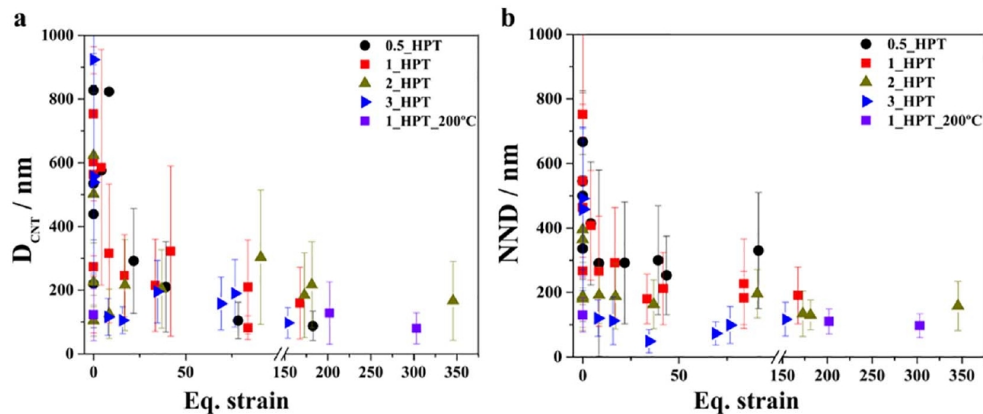

Fig. 3. a) Evolution of agglomerate diameter D_{CNT}, and b) evolution of the mean inter-particle distance (defined as NND) with increasing strain, of samples with different compositions.

area was obtained and the diameter of an equivalent circumference was computed as the agglomerate equivalent diameter D_{CNT}. Additionally, the position of the agglomerate centers of mass was extracted and used to calculate the NND (nearest neighbor distance). The evolution of the area weighted agglomerate diameter and the mean NND with increasing equivalent strain were studied (Fig. 3).

2.3. Quantitative Assessment of the Distribution Homogeneity and Clustering Behavior

Furthermore, a set of samples was analyzed in terms of homogeneity and distribution using two different methodologies. The quantitative assessment of the homogeneity was carried out following the method proposed by Rossi et al. [23]. The agglomerate area fraction (phase amount) and the number of objects were obtained using particle analysis in 20 different regions of interest using ROI manager in FIJI. The region homogeneity H_R is a constructed homogeneity obtained by multiplying the object number homogeneity H_{NO} and the phase amount homogeneity H_{PA}. The partial homogeneities H were calculated as the counterpart of the Gini G coefficients G: $H = 1 - G$, which is a measure of distribution inequality [22]. The Gini index of each parameter (object number and phase amount as obtained from particle analysis in FIJI) was retrieved using the *ineq* package in R studio, an integrated development environment for R, which is a programming language for

statistical computer and graphics [25].

Information about the agglomerates' centers of mass was used for further point pattern analysis by means of the nearest neighbor distance distribution function (G-function) using the *spatstat* package in R Studio [29], in order to obtain more detailed information about the spatial behavior between the individuals (CNT agglomerates' centers of mass, treated as "points") of the investigated population (studied areas, treated as "point patterns"). This method consists on the comparison of the empirical cumulative distribution function $G_{obs}(r)$, with the nearest neighbor distribution function $G_{theo}(r)$ for complete spatial randomness (CSR). The nearest neighbor distance distribution function for a CSR is described by $G_{theo}(r) = 1 - \exp(-N_A \pi r^2)$, where N_A is the number of particles per unit area, and r the evaluated distance. According to this, the condition $G_{obs}(r) < G_{theo}(r)$ is inherent of regular patterns and the opposite case, $G_{obs}(r) > G_{theo}(r)$, is interpreted as "clustering" (for example, Fig. 4a–c) because the NND are smaller than expected for the CSR case [30–32]. As there are numerous configurations for CSR, pointwise critical envelops with fixed respective number of points (corresponding to each case), obtained from 100 Monte Carlo simulations of CSR with a significance level of $2/101 = 0.0198$ and spatial Kaplan-Meier edge correction, which is performed in order to correct effects arising from the non-visibility of points lying outside the evaluated field of view during the evaluation of the G-Function [33], were plotted as the theoretical expected behavior.

Accordingly, the G-function is a useful tool in spatial statistics that summarizes the "clustering" behavior of points in a point pattern. It displays the empiric cumulative distribution of NND in contrast to that of the CSR with the same number of points within a window of the same size. If a point pattern does not adjust to a Poisson pattern, then it can be either *clustered* (i.e. when the particles are interacting and tend to come closer together) or *regular* (i.e. when the points tend to avoid each other). It might be inferred that a homogeneous sample, e.g. with a high H_{RO} value, also does not display a clustering behavior and vice versa. The G-Function can help to confirm or deny this statement. In this case, border corrections are carried out and the size of the window is arbitrary. For this reason, the G-function was chosen as a complementary method.

3. Results and Discussion

By plotting the area weighted mean agglomerate diameter D_{CNT} and the mean NND vs. Eq. Strain (Fig. 3) the evolution of both parameters with increasing strain can be tracked. Results show that both, D_{CNT} and NND decrease significantly in size during the first stages of deformation approximately up to a strain of 20, but do not significantly change afterwards, where both D_{CNT} and NND are between 100 and 400 nm. The deviation of the data also decreases with increasing strain. Fig. 3b also suggests that the agglomerates come closer for higher CNT concentration. Furthermore, a previous study showed that the agglomerate area fraction does not change significantly with increasing strain values [34]. Fig. 3 also displays information for a sample with 1 wt% CNT processed with 30 T at 200 °C. In the latter case, D_{CNT} and NND are also within the same range discussed before.

Nevertheless, from these results, an explicit relation concerning the evolution of the particle homogeneity during HPT is not feasible. In order to address this matter, analysis of the distribution of the CNT was carried out using the region homogeneity parameter H_{RO} and the nearest neighbor distribution function G.

The parameter region homogeneity H_{RO}, as proposed by Rossi et al. [23] serves as a general evaluation of the distribution of particles lying within a studied area divided in an arbitrary number of regions, by quantifying the similarity of the different regions in terms of number of objects and amount of phase. This method is a practical and straightforward way of assessing the homogeneity distribution, when studying well-dispersed particle composites. Nevertheless, it does not take into account the separation or the interaction of the agglomerates (it is not sensitive to the clustering behavior of particles within the analyzed regions). Furthermore, the analysis is limited to samples (micrographs) of the same dimensions, since this method is area size sensitive.

On the other hand, when studying non-deformed MMC samples, lower magnifications can be used in order to display a higher number of particles without neglecting any significant information since the initial agglomerates are much larger ($D_{CNT} > 2\mu$m) than in the case of highly deformed samples ($D_{CNT} \sim 100$ nm, Fig. 3). Furthermore, it is possible to keep the size of the analyzed area constant and H_{RO} can be used to compare the homogeneity of different kind of MMC samples. Nevertheless, the inability of using lower magnifications and of keeping the size of the micrographs constant without losing significant information restricts the usefulness of H_{RO} in highly deformed samples.

Fig. 4d displays the evolution of H_{RO} for the samples with 1 wt% CNT processed at RT. Even though H_{RO} does not significantly improve during HPT up to 30 T, in most cases it is true that H_{RO} increases with increasing strain except after only 1 T. Also, the diameter of the agglomerates and the inter-particle distance decrease significantly compared to the HUP samples (Fig. 3), and this is also an indicative of the improvement of the agglomerate distribution. Fig. 4a–c corresponds to the G-function of samples with 1 wt% CNT processed 10 T, which displayed the higher improvement in H_{RO} (Fig. 4d). In all the cases a clustered behavior is present, as the empiric distributions are above the envelope for 100 simulations of the theoretical CSR expectation. In the

case of samples with 1 wt% CNT processed 30 T, H_{RO} increases slightly with increasing strain above $H_{RO} = 60$% (Fig. 4d). Fig. 4e–h shows the G-function for the latter case. It can be seen from Fig. 4e that even for zero equivalent strain the empiric cumulative distribution of NND is closer to the CSR envelope. Nevertheless, for distances > 50 nm, a slight clustering behavior is observable. It can be inferred that for eq. strains $84 < \varepsilon < 100$ (Fig. 4c and f) the agglomerate NND cumulative distribution starts to behave homogeneously (Fig. 4f–h G_{obs} stays within the envelope for completely random Poisson distributions).

A similar behavior can be seen in Fig. 5 for the samples with 1 wt% CNT processed 30 T at 200 °C. In this case is also true that when $\varepsilon = 0$, G(r) is closer to the theoretical expectation CRS and for higher ε, G(r) is within the CRS envelopes, and for distances < 100 nm the agglomerates are more separated than the CRS case.

Sabirov [10] proposed the extended Tan and Zhang model (originally conceived for cold rolled MMCs) as an assessment of the equivalent strain values required in HPT to achieve a homogeneous particle distribution in ceramic particle reinforced MMC subjected to extrusion according to $d_p \geq \dfrac{d_m}{\left[\left(\frac{\pi}{6f}\right)^{\frac{1}{3}}\right]\sqrt{R}\,\gamma}$ where d_p is the particle size, d_m is the matrix powder size required to attain a homogeneous particle distribution; f the particle volume fraction; R is the extrusion ratio; γ is the shear strain with $\gamma = \sqrt{3}\,\varepsilon_{eq}$. This is based on the assumption that the particles are spherical. They found that SiC and Al_2O_3 particles behave differently during HPT and that the homogenization occurs according to Tan and Zhang model [35]. Nevertheless, the experimental data did not adjust well to their proposed model, which was attributed to the fact that the ceramic particles are de-clustered through a debonding mechanism without deformation of the particle clusters.

Although, in the samples studied here, the agglomerates cannot be considered spherical throughout the entire process because during the first stages of deformation elongated CNT agglomerates in the shear direction are observed (Fig. 2, $\varepsilon = 0$). Nevertheless, at higher applied strains, they start to debond forming more spherical agglomerates (Fig. 2, eq. $\varepsilon = 84$). Contrary to ceramic particles, which are hard and brittle, CNT are elastic and CNT agglomerates are bonded by Van der Waals forces that can be overcome during deformation. According to this, CNT agglomerates debond by relative sliding between CNT. Furthermore, sliding between CNT walls may also occur [36].

In the literature, a unique value of inter-particle distance, which only deals with the case of equidistant particles, has been considered for the assessment of a uniform distribution of particles during plastic deformation [10,35]. Nevertheless, as already discussed, the particles can be homogeneously distributed according to different configurations describing a Poisson distribution. Therefore, a model is proposed, starting from the nearest neighbor distribution function in 3D, and its correlation with the CNT agglomerates' spatial behavior. In this case, HPT is considered and the agglomerates are assumed to be spherical.

The nearest neighbor distance NND distribution function in 3D for completely random Poisson distribution is described by Eq. (1) [37]:

$$D(r) = 1 - \exp\left(-N_V \frac{4\pi}{3} r^3\right); \, r \geq 0 \tag{1}$$

where N_V is the mean number of objects per unit volume. N_V for isolated spherical objects of random diameter D is [37] (pg. 78):

$$N_V = \frac{6 V_V}{\pi D^3} \tag{2}$$

Replacing 2 in Eq. (1) yields:

$$D(r) = 1 - \exp\left(-\frac{8 V_V}{D^3} r^3\right) \tag{3}$$

For point fields it is true that the volume fraction equals the spherical contact distribution $V_V = H^s(r)$ and from the completely random property of the Poisson field it follows that the NND distribution D(r) and the spherical contact distribution function $H^s(r)$ are identical [37]
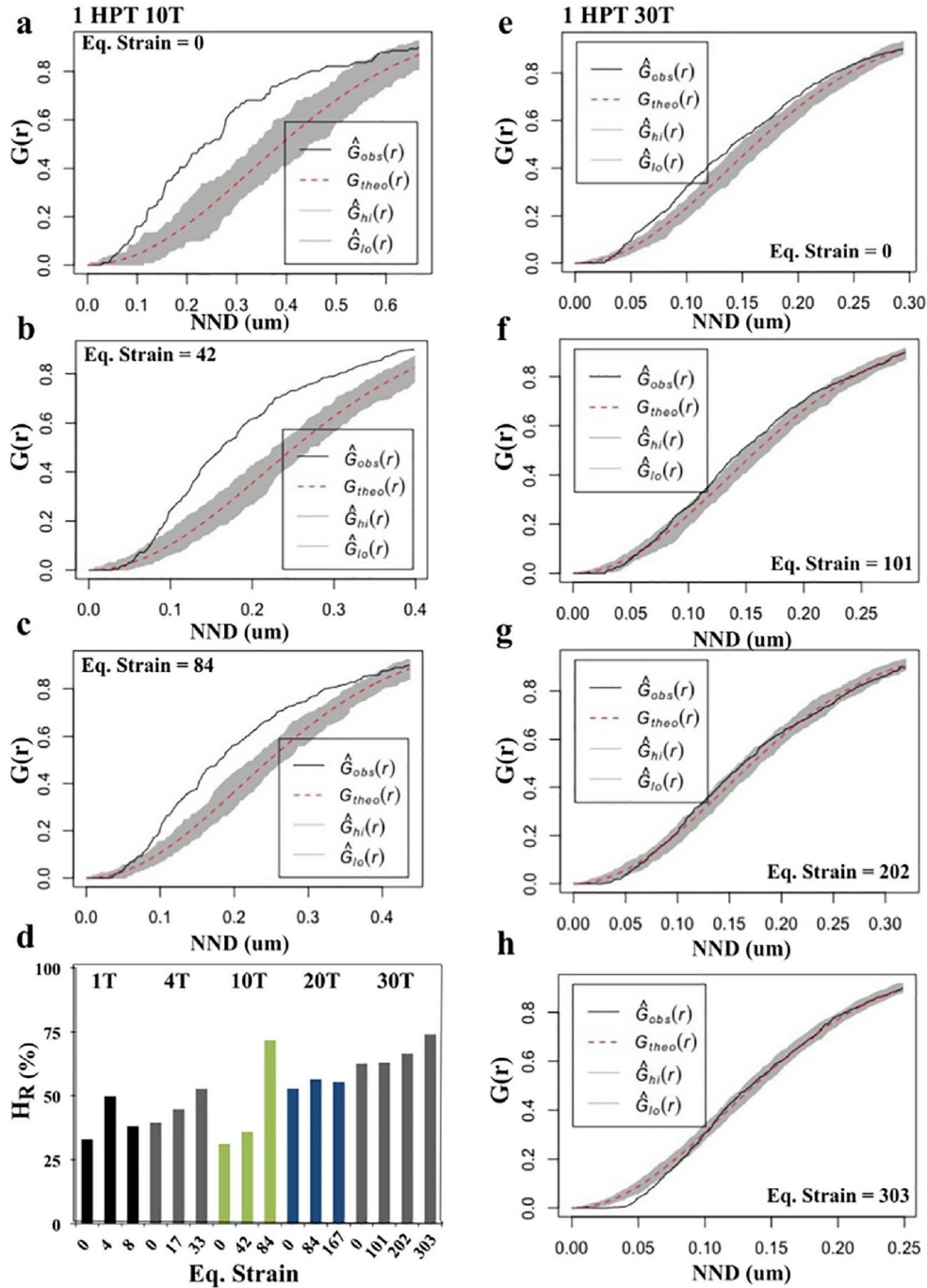
Fig. 4. (a–c) G(r) at different equivalent strains for 1 wt% CNT deformed at 10 T. (d) H_{RO} for the selected set of samples. (e–f) G(r) at different equivalent strains for 1 wt.%CNT deformed at 30 T. Where $\hat{G}_{Obs}$ (r) is the observed value of G(r); G_{theo} (r) is the theoretical value of G(r) for complete spatial randomness; G_{lo} (r) and G_{hi} (r) represent the lower and upper bounds of G(r) from simulations. The deformation was performed at room temperature.

(pg. 315) $H^s(r) \equiv D(r)$, thus $D(r) = V_V$. According to this and solving r in Eq. (2):

$$r = \frac{D}{2}\left[-\frac{\ln(1 - V_V)}{V_V}\right]^{1/3}$$

(4)

Also, for uniform distribution of CNT, which are expected to be at the grain boundaries due to the nature of the processing route (powder metallurgy), r should be equal or greater than the grain size of the

matrix after HPT GS_{fHPT}:

$$r \geq GS_{fHPT}$$

(5)

Furthermore, for simple shear a volume element, which may be a grain or a second phase in a composite, will be deformed in an ellipsoid with apex ratio r'. The reduction ratio of an ellipsoid is given by $\sqrt{r'}$. For large shear strains ($\gamma > 2$), $r' = \gamma^2$, with $\gamma = \sqrt{3}\varepsilon_{eq}$ [28]. In the case of the studied CNT reinforced MMC, it is assumed that the agglomerates
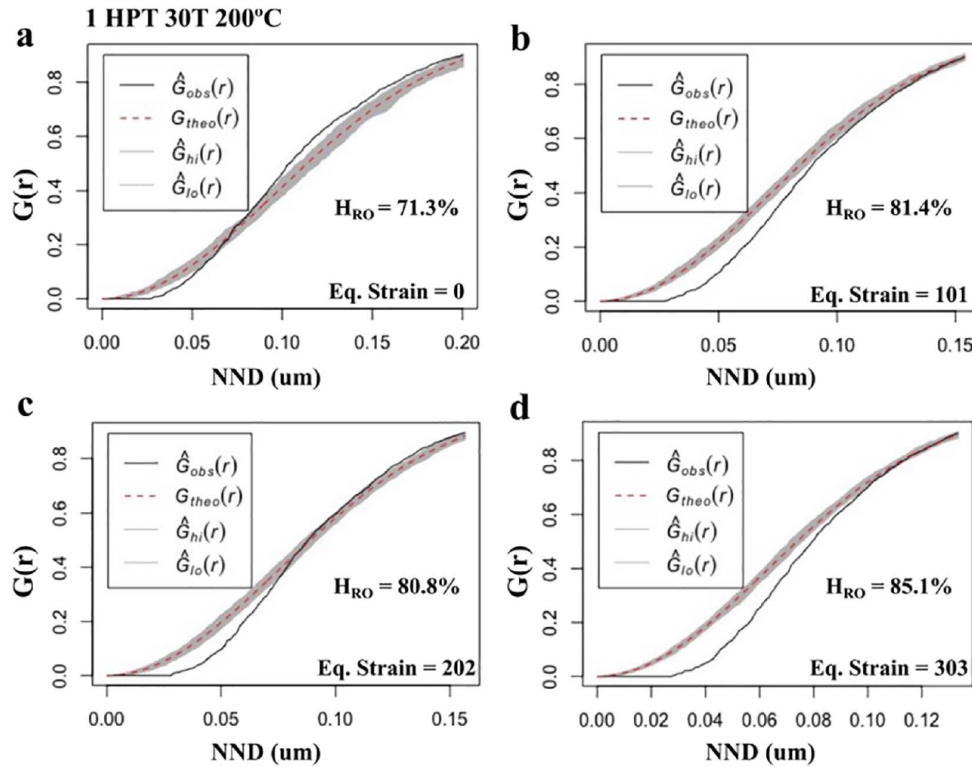
Katherine Aristizabal   77   *Results and discussion*

Fig. 5. G(r) for a 1 wt.%CNT sample processed with 30 T at 200 °C, as a function of the equivalent strain. The measured H_{RO} is also displayed.

are deformed in the same way as the matrix. Accordingly, after HPT the reduction ratio is given by:

$$\frac{GS_{iHPT}}{GS_{fHPT}} = \sqrt{3}\,\varepsilon_{eq} \qquad (6)$$

GS_{iHPT} corresponds to the grain size of the matrix before HPT, i.e. the grain size of the composite after the sintering process by HUP $GS_{iHPT} = GS_{fHUP}$. Thus, replacing in Eq. (6) and solving GS_{fHUP}:

$$GS_{fHPT} = \frac{GS_{fHUP}}{\sqrt{3}\,\varepsilon_{eq}} \qquad (7)$$

and Eq. (5) can be expressed as:

$$\frac{D}{2}\left[-\frac{\ln(1-V_V)}{V_V}\right]^{1/3} \geq \frac{GS_{fHUP}}{\sqrt{3}\,\varepsilon_{eq}} \qquad (8)$$

Previously, it was shown for consolidated CNT reinforced Nickel matrix composites that, in the presence of CNT a grain growth stagnation takes place during sintering and eventual annealing and the final grain size is related to the CNT volume fraction V_V according to the Zener based relationship $GS_{fHUP} = \frac{0.99 \pm 0.07}{V_V^{0.4}}$ [38].

Fig. 6 shows the experimental data of the mean grain size measured by EBSD of the studied composites before HPT with the corresponding Zener based model.

Accordingly, and rearranging Eq. (8):

$$\varepsilon_{eq} \geq \frac{1.143 V_V^{\left(-\frac{1}{15}\right)}}{D}\left[-\frac{1}{\ln(1-V_V)}\right]^{\left(\frac{1}{3}\right)} \qquad (9)$$

According to Eq. (9), there is a minimum strain ε^{hom} that should be applied in order to obtain a homogenous distribution of CNT. It can be thus inferred that for increasing CNT volume fraction V_{CNT} a lower strain should be applied in order to obtain a homogeneous distribution of CNT after HPT. This corresponds well with the literature, where, for
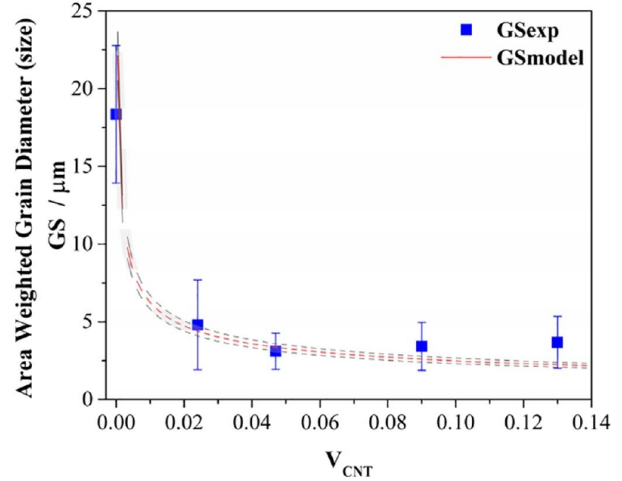

Fig. 6. Mean grain size of studied composites after HUP as a function of the reinforcement volume fraction (V_{CNT}). Dashed curves represent the empirical Zener pinning model with respective upper and lower bounds (grey envelope).

Table 1
Values of equivalent strain required for achieving a homogenous CNT distribution in MMC processed by HPT.

V_{CNT}	ε^{hom}
0.024	126.5
0.047	96.31
0.09	73.71
0.13	63.16

lower V_{CNT}, inhomogeneity rises due to the presence of reinforcement-depleted regions [23,39]. Table 1 shows the results for ε^{hom}, according to Eq. (9), for the different CNT compositions used in this work.

In the case of the samples with 1wt. %CNT (V_{CNT} = 0.047) ε^{hom} = 96.31, which is within the range 84 < ε < 100 previously found experimentally, for which these samples were found to be homogenously distributed according to the NND distribution function. These homogenously distributed samples presented values of region homogeneity $H_R \geq 60\%$. It can thus be inferred, that a H_R over 60% is an empirical lower bound, which is necessary but not sufficient to un-equivocally identify a homogeneous random distribution of the second phase. It is therefore unavoidable the utilization of a complementary evaluation, as proposed here, which additionally evaluates the distribution of the mean spatial inter-particle distance. Furthermore, this approach provides information valuable for the optimization of the processing parameters by HPT of MMC.

4. Conclusions

The distribution homogeneity of CNT agglomerates in MMC processed by high-pressure torsion is evaluated by the combination of the region homogeneity parameter H_{RO} and the nearest neighbor distribution function G(r). This methodology can be used as a thorough evaluation of the distribution homogeneity of second phases in MMC. Furthermore, CNT agglomerates debond by relative sliding between CNT during HPT, which differs significantly to the debonding-mechanism in ceramic particles. Finally, a model that predicts the minimum equivalent strain required for a homogenous second phase distribution during HPT is developed, which correlates well with the experimental data and provides a basis for the optimization of the processing parameters of MMC by severe plastic deformation.

Acknowledgements

References

[1] R. Haggenmueller, H.H. Gommans, A.G. Rinzler, J.E. Fischer, K.I. Winey, Aligned single-wall carbon nanotubes in composites by melt processing methods, Chem. Phys. Lett. 330 (2000) 219–225, http://dx.doi.org/10.1016/S0009-2614(00)01013-7.

[2] C. Bower, R. Rosen, L. Jin, Deformation of carbon nanotubes in nanotube, Polym. Compos. 74 (1999) 3317–3319.

[3] A. Peigney, C. Laurent, E. Flahaut, A. Rousset, Carbon Nanotubes in Novel Ceramic Matrix Nanocomposites, 26 (2000), pp. 677–683.

[4] A. Peigney, E. Flahaut, C. Laurent, F. Chastel, A. Rousset, Aligned carbon nanotubes in ceramic-matrix nanocomposites prepared by high-temperature extrusion, Chem. Phys. Lett. 352 (2002) 20–25, http://dx.doi.org/10.1016/S0009-2614(01)01441-5.

[5] S. Suarez, F. Lasserre, F. Mücklich, Mechanical properties of MWNT/Ni bulk composites: influence of the microstructural refinement on the hardness, Mater. Sci. Eng. A 587 (2013) 381–386, http://dx.doi.org/10.1016/j.msea.2013.08.058.

[6] S.R. Bakshi, D. Lahiri, A. Agarwal, Carbon nanotube reinforced metal matrix composites - a review, Int. Mater. Rev. (2010), http://dx.doi.org/10.1179/095066009X12572530170543.

[7] T. Kuzumaki, K. Miyazawa, H. Ichinose, K. Ito, Processing of carbon nanotube reinforced aluminum composite, J. Mater. Res. 13 (1998) 2445–2449, http://dx.doi.org/10.1557/JMR.1998.0340.

[8] H.J. Choi, G.B. Kwon, G.Y. Lee, D.H. Bae, Reinforcement with carbon nanotubes in aluminum matrix composites, Scr. Mater. 59 (2008) 360–363, http://dx.doi.org/10.1016/j.scriptamat.2008.04.006.

[9] S.R. Bakshi, V. Singh, K. Balani, D.G. McCartney, S. Seal, A. Agarwal, Carbon nanotube reinforced aluminum composite coating via cold spraying, Surf. Coat. Technol. 202 (2008) 5162–5169, http://dx.doi.org/10.1016/j.surfcoat.2008.05.042.

[10] I. Sabirov, O. Kolednik, R. Pippan, Homogenization of metal matrix composites by high-pressure torsion, Metall. Mater. Trans. A 36 (2005) 2861–2870.

[11] R. Pippan, S. Scheriau, A. Taylor, M. Hafok, A. Hohenwarter, A. Bachmaier, Saturation of fragmentation during severe plastic deformation, Annu. Rev. Mater. Res. 40 (2010) 319–343, http://dx.doi.org/10.1146/annurev-matsci-070909-104445.

[12] S. Suarez, F. Lasserre, F. Soldera, R. Pippan, F. Mücklich, Microstructural thermal stability of CNT-reinforced composites processed by severe plastic deformation, Mater. Sci. Eng. A 626 (2015) 122–127, http://dx.doi.org/10.1016/j.msea.2014.12.065.

[13] P. Jenei, J. Gubicza, E.Y. Yoon, H.S. Kim, J.L. Lábár, High temperature thermal stability of pure copper and copper-carbon nanotube composites consolidated by High Pressure Torsion, Compos. A: Appl. Sci. Manuf. 51 (2013) 71–79, http://dx.doi.org/10.1016/j.compositesa.2013.04.007.

[14] A. Bachmaier, R. Pippan, Generation of metallic nanocomposites by severe plastic deformation, Int. Mater. Rev. 58 (2013) 41–62, http://dx.doi.org/10.1179/1743280412Y.0000000003.

[15] K. Aristizabal, S. Suárez, A. Katzensteiner, A. Bachmaier, F. Mücklich, Evolution of the microstructure in carbon nanotube reinforced Nickel matrix composites processed by high-pressure torsion, IOP Conf. Ser. Mater. Sci. Eng. 258 (2017) 12008, , http://dx.doi.org/10.1088/1757-899X/258/1/012008.

[16] I.H. Sul, J.R. Youn, Y.S. Song, Quantitative dispersion evaluation of carbon nanotubes using a new analysis protocol, Carbon 49 (2011) 1473–1478, http://dx.doi.org/10.1016/j.carbon.2010.12.017.

[17] B.M. Tyson, R.K. Abu Al-Rub, A. Yazdanbakhsh, Z. Grasley, A quantitative method for analyzing the dispersion and agglomeration of nano-particles in composite materials, Compos. Part B 42 (2011) 1395–1403, http://dx.doi.org/10.1016/j.compositesb.2011.05.020.

[18] A. Yazdanbakhsh, Z. Grasley, B. Tyson, R.K. Abu Al-Rub, Dispersion quantification of inclusions in composites, Compos. A: Appl. Sci. Manuf. 42 (2011) 75–83, http://dx.doi.org/10.1016/j.compositesa.2010.10.005.

[19] S.R. Bakshi, R.G. Batista, A. Agarwal, Quantification of carbon nanotube distribution and property correlation in nanocomposites, Compos. A: Appl. Sci. Manuf. 40 (2009) 1311–1318, http://dx.doi.org/10.1016/j.compositesa.2009.06.004.

[20] N. Saheb, N.U. Qadir, M.U. Siddiqui, A.F.M. Arif, S.S. Akhtar, N. Al-Aqeeli, Characterization of nanoreinforcement dispersion in inorganic nanocomposites: a review, Materials (Basel). 7 (2014) 4148–4181, http://dx.doi.org/10.3390/ma7064148.

[21] R. Pyrz, Quantitative description of the microstructure of composites. Part I: morphology of unidirectional composite systems, Compos. Sci. Technol. 50 (1994) 197–208, http://dx.doi.org/10.1016/0266-3538(94)90141-4.

[22] P. Rossi, M. Engstler, F. Mücklich, Quantitative classification and assessment of Sr modification in hypoeutectic Al-Si and Al-Si-Mg alloys, Pract. Metallogr. 52 (2015) 571–589, http://dx.doi.org/10.3139/147.110361.

[23] P. Rossi, S. Suarez, F. Soldera, F. Mücklich, Quantitative assessment of the reinforcement distribution homogeneity in CNT/metal composites, Adv. Eng. Mater. 1 (2014) 1–5, http://dx.doi.org/10.1002/adem.201400352.

[24] J. Schindelin, I. Arganda-Carreras, E. Frise, V. Kaynig, M. Longair, T. Pietzsch, S. Preibisch, C. Rueden, S. Saalfeld, B. Schmid, J.-Y. Tinevez, D.J. White, V. Hartenstein, K. Eliceiri, P. Tomancak, A. Cardona, Fiji: an open-source platform for biological-image analysis, Nat. Methods 9 (2012) 676–682 https://doi.org/10.1038/nmeth.2019.

[25] RStudio Team, RStudio: Integrated Development for R, RStudio, Inc., Boston, MA, 2016 http://www.rstudio.com/.

[26] L. Reinert, M. Zeiger, S. Suárez, V. Presser, F. Mücklich, Dispersion analysis of carbon nanotubes, carbon onions, and nanodiamonds for their application as reinforcement phase in nickel metal matrix composites, RSC Adv. 5 (2015) 95149–95159, http://dx.doi.org/10.1039/C5RA14310A.

[27] A. Hohenwarter, A. Bachmaier, B. Gludovatz, S. Scheriau, R. Pippan, Technical parameters affecting grain refinement by high pressure torsion, Int. J. Mater. Res. 100 (2009) 1653–1661, http://dx.doi.org/10.3139/146.110224.

[28] H.P. Stüwe, Equivalent strains in severe plastic deformation, Adv. Eng. Mater. 5 (2003) 291–295, http://dx.doi.org/10.1002/adem.200310085.

[29] A. Baddeley, R. Turner, Journal of statistical software, J. Stat. Softw. 12 (2005), http://dx.doi.org/10.18637/jss.v069.i12.

[30] B.D. Ripley, Statistical Inference for Spatial Processes, Cambridge University Press, New York, USA, 1988.

[31] N. Cressie, Statistics for Spatial Data, John Wiley & Sons, New York, USA, 1991, http://dx.doi.org/10.1111/j.1365-3121.1992.tb00605.x.

[32] J. Peter, Diggle, Statistical Analysis For Spatial Point Processes, Academic Press, London, 1983.

[33] A. Baddeley, R.D. Gill, Kaplan-Meier estimators of distance distributions for spatial point processes, Ann. Stat. 25 (1997) 263–292, http://dx.doi.org/10.1214/aos/1034276629.

[34] A. Katzensteiner, K. Aristizabal, S. Suarez, R. Pippan, A. Bachmaier, Temperature dependent structural evolution in nickel/carbon nanotube composites processed by high-pressure torsion, IOP Conf. Ser. Mater. Sci. Eng. 194 (2017) 12019, , http://dx.doi.org/10.1088/1757-899X/194/1/012019.

[35] M.J. Tan, X. Zhang, Powder metal matrix composites: selection and processing, Mater. Sci. Eng. A 244 (1998) 80–85, http://dx.doi.org/10.1016/S0921-5093(97)00829-0.

[36] A. Pantano, D.M. Parks, M.C. Boyce, Mechanics of deformation of single- and multi-wall carbon nanotubes, J. Mech. Phys. Solids 52 (2004) 789–821, http://dx.doi.org/10.1016/j.jmps.2003.08.004.

[37] J. Ohser, F. Mücklich, Statistical Analysis of Microstructures in Material Sciences, John Wiley & Sons, Chichester, UK, 2000.

[38] L. Reinert, S. Suarez, T. Müller, F. Mücklich, Carbon nanoparticle-reinforced metal matrix composites: microstructural tailoring and predictive modeling, Adv. Eng. Mater. (2017) 1–6, http://dx.doi.org/10.1002/adem.201600750.

[39] S. Yamanaka, R. Gonda, A. Kawasaki, H. Sakamoto, Y. Mekuchi, M. Kun, T. Tsukada, Fabrication and thermal properties of carbon nanotube/nickel composite by spark plasma sintering method, Mater. Trans. 48 (2007) 2506–2512, http://dx.doi.org/10.2320/matertrans.MRA2007084.

381

IV. Evolution of the lattice defects and crystalline domain size in carbon nanotube metal matrix composites processed by severe plastic deformation

Katherine Aristizabal[1], Andreas Katzensteiner[2], Matteo Leoni[3], Frank Mücklich[1], Sebastián Suárez[1]

1 Department of Material Science and Engineering, Saarland University,
66123 Saarbrücken, Germany
2 Erich Schmid Institute, Austrian Academy of Sciences, Jahnstrasse 12, 8700 Leoben, Austria
3 University of Trento, DICAM, via mesiano, 77, 38123 Trento, Italy

Own Contribution: Project management, sample manufacturing and processing, experimental execution, data analysis, conceptualization of experimental results and calculations, manuscript writing.

Abstract:

Nickel (Ni) and carbon nanotube (CNT)-reinforced Ni-matrix composites were processed by high-pressure torsion (HPT). The evolution of dislocation densities and crystalline domain sizes were analyzed by means of X-ray diffraction (XRD) using Whole Powder Pattern Modelling (WPPM). The composites showed an evident gradient in the microstructural refinement and in hardness with increasing applied strain. This effect was found to be more pronounced in the
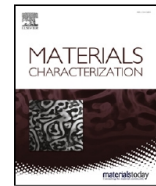
presence of higher amounts of CNT. In particular, a higher amount of screw dislocations was measured by WPPM after HPT. It was concluded that the strengthening of CNT-MMC processed by HPT is mainly due to work hardening and grain refinement, both mechanisms being assisted by the presence of CNT, with marginal contribution of particle strengthening.

Evolution of the lattice defects and crystalline domain size in carbon nanotube metal matrix composites processed by severe plastic deformation

Katherine Aristizabal[a,*], Andreas Katzensteiner[b], Matteo Leoni[c], Frank Mücklich[a], Sebastian Suárez[a]

[a] *Department of Materials Science, Saarland University, D-66123 Saarbrücken, Germany*
[b] *Erich Schmid Institute of Materials Science, Austrian Academy of Sciences, Jahnstrasse 12, A-8700 Leoben, Austria*
[c] *University of Trento, DICAM, via mesiano, 77, 38123 Trento, Italy*

ARTICLE INFO

ABSTRACT

Nickel (Ni) and carbon nanotube (CNT)-reinforced Ni-matrix composites were processed by high-pressure torsion (HPT). The evolution of dislocation densities and crystalline domain sizes were analyzed by means of X-ray diffraction (XRD) using Whole Powder Pattern Modelling (WPPM). The composites showed an evident gradient in the microstructural refinement and in hardness with increasing applied strain. This effect was found to be more pronounced in the presence of higher amounts of CNT. In particular, a higher amount of screw dislocations was measured by WPPM after HPT. It was concluded that the strengthening of CNT-MMC processed by HPT is mainly due to work hardening and grain refinement, both mechanisms being assisted by the presence of CNT, with marginal contribution of particle strengthening.

1. Introduction

It is well known that during severe plastic deformation (SPD) there is an increase in the dislocation density and high-angle grain boundaries, leading to the refinement of the microstructure [1]. Particularly in high pressure torsion (HPT), a microstructural gradient is observed in the sample (along the radial direction), which decreases gradually with increasing imposed strain until the saturation in the microstructural refinement is reached [2,3]. In the case of pure Ni, the equivalent von Mises strain ε_v needed to reach the onset of saturation in the microstructural refinement, characterized by a fairly constant hardness throughout the sample, is approximately $\varepsilon_v \sim 20$ [3]. In the disk center, on the other hand, stress homogeneity is not really obtained [4]. Nevertheless, although the equivalent strain there should be zero, according to $\varepsilon_v = \frac{2\pi Tr}{t\sqrt{3}}$, where T is the number of turns, t is the sample thickness and r the distance from the center of the sample [5], the dislocation density should increase due to the accumulated stress, especially in the case of pure metals, in which impurities are not expected to influence the microstructural evolution during processing. Furthermore, as dislocation glide is a very important deformation mechanism during HPT [4], a thorough analysis of the dislocation density in severely deformed CNT/Ni composites is of great interest, in order to better understand the remarkable increase in hardness [6] and the

premature cracking during the deformation process at room temperature in the presence of high amounts of CNT [7]. Nevertheless, and to the best knowledge of the authors, there are still limited studies in the literature regarding the microstructural evolution of severely deformed metal matrix composites (MMC).

Structural and microstructural information, including crystalline domain sizes and dislocation densities, have been extracted from diffraction patterns by means of line profile analysis (LPA) using traditional approaches such as the Scherrer equation [8], the Warren-Averbach method [9] and Williamson-Hall plot [10]. Furthermore, semi-quantitative studies based on the modified approaches of these traditional techniques are common [11–16], which take into account the anisotropic nature of the dislocation strain field by considering the so-called dislocations contrast factor. Nevertheless, most of these techniques are limited to the extraction of microstructural information from the peak widths, by fitting each reflection with an arbitrary bell-shaped function; all other diffraction pattern details, albeit potentially important, are disregarded. To remove this limitation, full pattern analysis techniques such as the Whole Powder Pattern Modelling (WPPM), have been proposed [17]. In WPPM, the line profiles are obtained from physical models of the instrument and from the specimen. Specifically, the peak shape originating from dislocation effects is obtained according to the Wilkens-Krivoglaz-Ryaboshapka theory [18]

* Corresponding author.
E-mail address: katherine.aristizabal@uni-saarland.de (K. Aristizabal).

that originally introduced the contrast factor of dislocations. Furthermore, dislocation densities analyzed by LPA techniques have been reported in the literature for severely deformed metals, whose high dislocation densities ($\rho > 10^{14}$ m^{-2}) cannot be easily quantified by means of traditional techniques such as Transmission Electron Microscopy (TEM); in many cases, conventional LPA is performed to obtain crystalline domain size and micro-strain, from which the dislocation density is calculated via the Williamson-Smallman approach [19–21], which is only valid for random distribution of dislocations (i.e. non-interacting dislocations).

The present study provides a systematic approach, in which WPPM is performed at two different positions on HPT deformed CNT/Ni composites as well on bulk Ni samples, by limiting the measured area along the radial direction and thus reducing the effect of the microstructural gradients on the results, in order to investigate the effect of increasing CNT content and increasing strain on the evolution of the domain size and dislocation densities during HPT. Finally, the strengthening contributions from grain boundaries, dislocation accumulation and the presence of particles were estimated from the results.

2. Materials and methods

The starting materials included multi-walled CNT (CCVD grown, Graphene Supermarket, USA density 1.84 g/cm^3) and dendritic Ni powder (Alfa Aesar, Germany mesh -325, 99.8% purity). Powder mixtures obtained via colloidal mixing (see e.g. [22]) were cold pressed (990 MPa) into cylindrical pellets (diameter 8 mm, thickness ~ 1 mm) and sintered under vacuum (2.0×10^{-6} mbar) at 900 °C for 3 h. Different CNT fractions were used, namely: 0.5, 1, and 2 wt% (2.4, 4.7 and 9 vol%, respectively). All sintered samples (~1 mm thickness and 8 mm of diameter) were further processed by means of HPT at room temperature using 1, 4, 10 and 20 T (turns), 4 GPa of pressure and 2 rpm. Pure Ni bulk samples were also obtained and processed under the same conditions and analyzed for comparison reasons, given that Ni has been extensively investigated and serves as model material for the HPT processing of MMC.

TEM micrographs were collected on selected samples using a JEOL JEM 2010 instrument operated at 200 kV. Specifically, Ni and 2 wt% CNT samples processed using 1 T and 20 T were analyzed at 3 mm from the center. The TEM lamellas were extracted perpendicular to the shear direction in a dual-beam Helios NanoLab 600 (FEI) microscope using a gallium focused ion beam (FIB).

The HPT samples were cut in halves, embedded in resin, polished using polishing disks with 6, 3 and 1 μm diamond suspensions and mirror-finished with OP-S (Struers) colloidal silica. In this way, possible effects of the sample roughness on the results are avoided. The X-ray diffractograms were collected using Cu-K$_\alpha$ radiation at room temperature by means of a PANalytical Empyrean diffractometer, equipped with a 50 μm focusing polycapillary collimator in the primary beam, and a parallel plate collimator (0.27° acceptance angle) in the diffracted beam. A Ni filter was used to suppress the unwanted K$_\beta$ radiation. In this setup, only the lattice planes parallel to the surface of the specimen, i.e. orthogonal to the scattering vector $\vec{s}$, contribute to the diffracted signal. In order to limit the effects of the microstructural gradients on the results, the beam size was restricted to a width of 50 μm and a variable length depending of the 2θ angle, e.g. 146.19 μm at 40° and 65.27 μm at 100°. In order to better correlate the results to the specific equivalent strains corresponding to the measured areas located at about 3 mm from the center, the specimen was aligned such that the scattering vector was parallel to the shear direction and in this way, although the X-ray penetration depth in Ni varies from 34.28 μm at 40° and 52.52 μm at 100°, the microstructural gradient along the depth is expected to be negligible.

Only the peaks corresponding to *fcc* Ni were observed in the 40°–100° scan range. The step size was set to 0.05° with 40 second counting time for a total of 1200 points. Fig. 1 shows a schematic
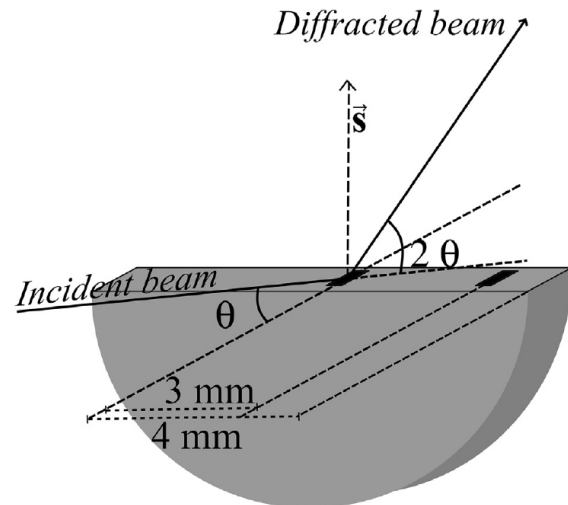

Fig. 1. X-ray diffraction in Bragg Brentano configuration used in the present study.

representation of the XRD setup. The LaB$_6$ instrumental profile powder standard was also measured with the same configuration in order to model the instrumental broadening, using an oscillation of the stage of 5 mm in the X axis to increase the counting statistics and reduce the graininess problems (the LaB$_6$ powder has in fact a particle size of ca. 2 μm and the particles are almost single crystals).

For the analysis of the dislocation density and the crystalline domain size, the PM2K software, implementing the WPPM method, was employed [23,24]. A thorough description of the WPPM approach is given elsewhere [17]. In the following a short and simplified introduction to the method is given.

In WPPM, the complex function $C_{hkl}(L)$ describes the Fourier Transform (FT) of the intensity $I_{hkl}(d^*)$ of the *hkl* diffraction profile. If d^* is a length in reciprocal space (equal to d_{hkl}^* in the Bragg condition), then

$$I_{hkl}(d^*) = k_{hkl}(d^*) \int C_{hkl}(L) \exp(2\pi L(d^* - d_{hkl}^*)) dL \qquad (1)$$

Here, $k_{hkl}(d^*)$ comprises all terms contributing to $I_{hkl}(d^*)$ and not related to line broadening sources, such as Lorenz-polarization factor, the structure factor, scale factor, etc. As broadening effects are convoluted in the measured diffraction profile and due to the properties of the Fourier transform of a convolution, $C_{hkl}(L)$ is a product of functions describing the various sources of broadening affecting the analyzed profile. In our case we have to consider, for instance, the instrumental broadening (T_{pV}^{IP}) that can be measured using a line-profile standard, the contribution from the finite size of the domains (A^S), the contribution from the lattice distortions caused by dislocations (A^D). Therefore,

$$C_{hkl}(L) = (T_{pV}^{IP}) \bullet (A^S) \bullet (A^D) \qquad (2)$$

Expressions for the above mentioned FTs can be found in [17]. Further broadening sources can be included, when necessary.

The parameters of interest obtained in the WPPM analysis were: mean (μ) and square of the variance (σ) of a log-normal distribution of coherent domain sizes, dislocation density (ρ), and average character of the dislocations (extracted as f_e, relative edge fraction). Spherical domains were used to model the diffraction patterns of the HPT samples with a log-normal distribution of domains, which has been considered appropriate in the case of severely deformed metals [1].

For a quantitative evaluation of the dislocation densities, the (orientation-averaged) dislocation contrast factor is however needed for each individual *hkl*. The approach proposed by Martinez-Garcia et al.

Microstructural development and stability in CNT/Ni composites processed by high pressure torsion
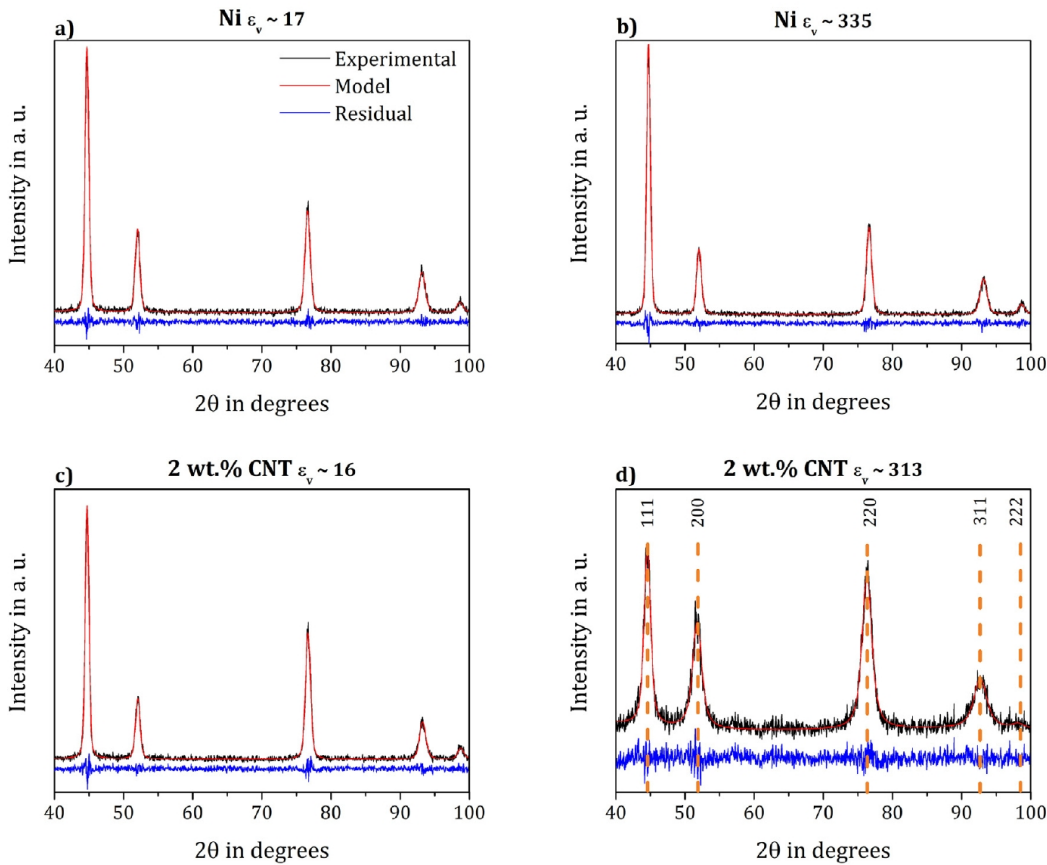
Fig. 2. Examples of WPPM of the data collected at 3 mm from the center on a) Ni after 1 T and b) after 20 T, c) 2 wt% CNT after 1 T and d) after 20 T.

[25] can be used in the general case. For cubic materials, the following holds [26]: $\bar{C}_{hkl} = A + BH$, with $H = \frac{(h^2k^2 + h^2l^2 + l^2h^2)}{(h^2 + k^2 + l^2)^2}$, and A and B are constants that depend on the dislocation slip system and on the single-crystal elastic constants of the material. The primary slip system of Ni is $\frac{1}{2}\langle 110 \rangle \{1\bar{1}1\}$ Suitable A and B values for edge and screw dislocations acting on this slip system were calculated from the known values proposed by Ungár et al. [11] obtained using the single elastic constants $c_{11} = 243.6$; $c_{12} = 149.4$ and $c_{44} = 119.6$ GPa (note that a different parameterization is used in the cited reference, and in particular that $A = \bar{C}_{h00}$, $B = -\frac{q}{A}$). The calculated values for edge dislocations are: $A_e = 0.262$, $B_e = -0.367$, and for screw dislocations: $A_s = 0.267$ and $B_s = -0.599$ in agreement with the data calculated by Scardi et al. [26].

Moreover, despite the technical difficulties related to the need of working with a small spot size and consequently, with a broad instrumental function, the agreement between data and model is rather good. As an example, Fig. 2 shows the modelling result for Ni and 2 wt% CNT samples processed to equivalent strains of $\varepsilon_v \sim 16$ and $\varepsilon_v \sim 320$, as representative examples. Moreover, the difference plot is almost featureless in all studied cases. Fig. 2 shows that the addition of CNT to Ni causes evident line broadening with increasing strain.

In addition, Vickers micro hardness ($HV_{0.3}$) measurements were performed at 3 mm from the samples' centers using an indenter Struers DuraScan 50/70/80 using 15 s of dwell time.

3. Results and discussion

TEM micrographs in Fig. 3 show exemplarily the effect of CNTs on the microstructural refinement with increasing applied strains. In contrast to pure Ni, where no further grain refinement is observed from Fig. 3e, the HPT applied to 2 wt% CNT samples (Fig. 3f) causes a significant decrease in grain size. Furthermore, oxide particles could also promote grain refinement by pinning the dislocation and grain boundary motion [27]. Nevertheless, a negligible contribution should be expected in this case in comparison to the effect provided by the CNTs. Note that the oxide signal is not detected as shown in the respective SAED patterns in Fig. 3. Additionally, the introduction of oxygen during SPD is more likely to occur in powder samples [28] than in annealed (bulk) ones (this study).

The evolution of the mean domain size, as well as the dislocation density with increasing equivalent strains is presented in Figs. 4 and 5, respectively. The mean domain sizes D and the respective standard deviations SD (presented as the error bars), have been calculated from the mean (μ) and the square of the variance (σ) of the log-normal distributions via $D = e^{\left(\mu + \frac{\sigma^2}{2}\right)}$ and $SD = \sqrt{(e^{(2\mu + \sigma^2)})(e^{\sigma^2} - 1)}$, respectively. In the case of the dislocation densities, the error bars correspond to the estimated errors in the WPPM.

Regarding the composites, the distribution of the reinforcement at the disks' centers is expected to be less homogeneous than at areas further away from it since the reinforcement distribution should improve with increasing equivalent strain and increasing CNT content [29]. Moreover, since the grain size is expected to reduce with increasing accumulated strain, a reduction in the domain sizes is expected further away from the samples' centers, especially in the composites, where the presence of second phases can enhance the refinement process. This effect can be observed in Fig. 4.

On one hand, the reduction in the domain size caused by the presence of CNT in the composites can be explained analogically to the
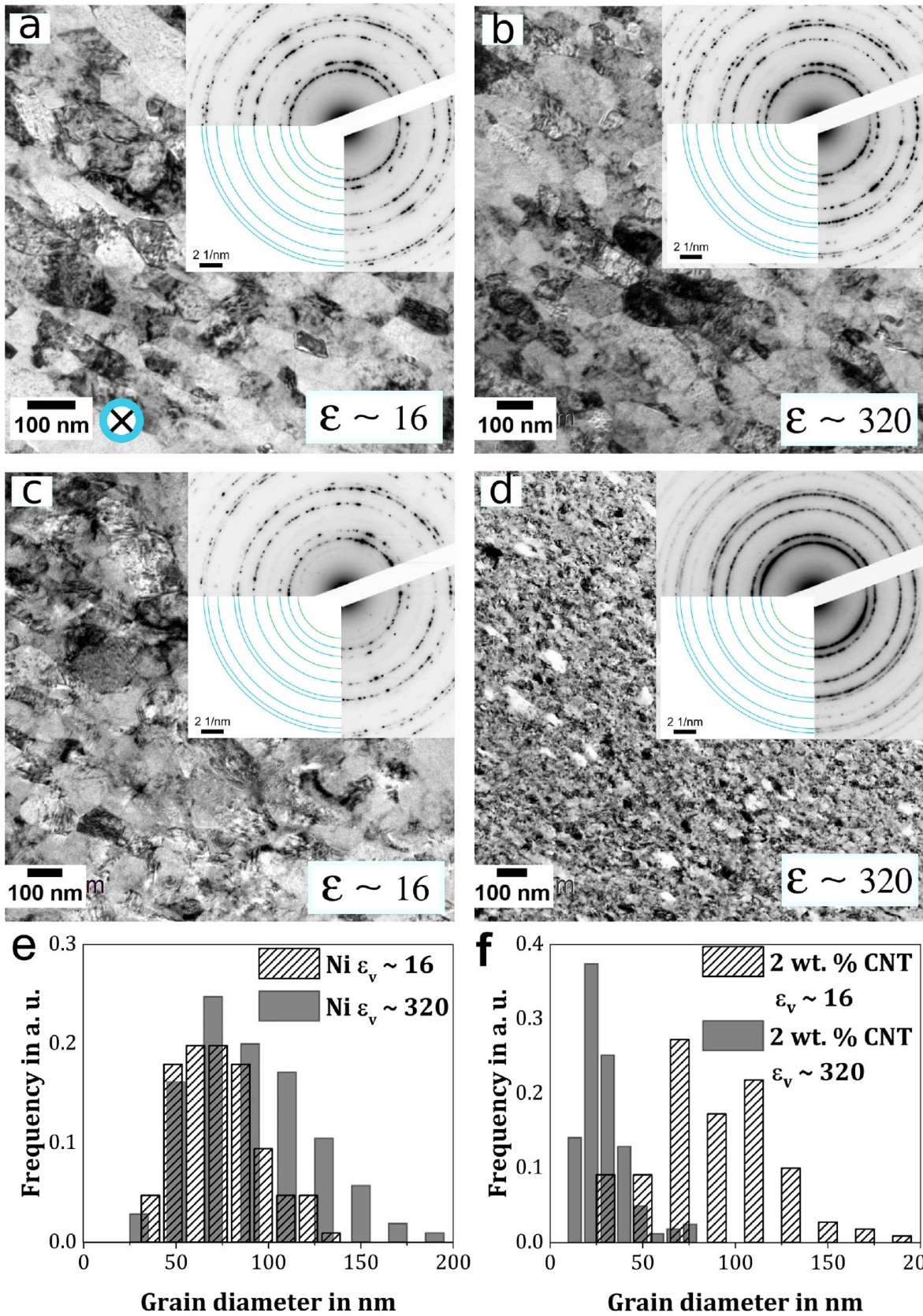
(caption on next page)

Fig. 3. Bright Field TEM micrographs and respective SAED patterns of (a, b): Ni and (c, d): 2 wt% CNT samples, processed to the respective equivalent strains, given on the micrographs. Shear direction normal to plane of paper (marked as X). (e, f): Grain size distributions of Ni and 2 wt% CNT samples, respectively.

reduction in grain size caused by impurities. It is well known that edge dislocations interact more effectively with solute atoms than screw dislocations. For instance, when edge dislocations interact with solute atoms inside the grains (such as dissolved oxygen atoms), they are pinned by them [28]. These pinning effects can eventually promote dislocation pile-up and subsequently dislocation rearrangement into low energy configurations (LAGB), which not only increases the dislocation density but also assists the microstructural refinement. At the same time, dislocations may interact with solute atoms and second phases at the grain boundaries. Additionally, as the steady state is ruled by the grain boundary mobility [3], the decrease in steady state grain size can be accounted by the pinning of the grain boundaries by impurities and second phase particles located there.

On the other hand, in the case of pure bulk Ni samples, processing above the equivalent strain needed for the saturation hardness to take place (i.e. $\varepsilon_v \sim 20$, see Fig. 6), leads to marginal changes in both the domain size and the dislocation density. No further decrease in the domain size might be related to a transient state, which involves dislocation pileup at the grain boundaries and grain boundary motion as discussed by Pippan et al. [3], who studied the evolution of the grain size of Ni samples subjected to HPT at room temperature starting from both coarse and nano grained samples, obtaining the same final steady state grain size after HPT. According to them, during SPD, pure metals are not further refined after the steady state has been reached due to stress-induced boundary migration phenomena. Furthermore, they estimated a saturation size of plastically deformed Ni of about 200 nm (as measured from TEM micrographs) [3]. In the present study, Ni average grain sizes extracted from TEM micrographs are in the order of ~80 nm (see Fig. 3e), which are in the same order to the sizes extracted from

WPPM for the respective samples (see Fig. 4a). However, the domains "seen" by diffraction should not be confused with the grains observed by microscopy: the two are the same only when the "grains" are defect-free, contain a non-significant quantity of defects, or defects are randomly distributed within the grains.

The dislocation density of the bulk Ni samples from the present study is consistent with the results reported in [30] for HPT Ni, namely $\rho \sim 0.3 \times 10^{16}\,\mathrm{m}^{-2}$ (Fig. 5a). On the other hand, the dislocation density increases in the composites with increasing applied strains and increasing CNT content. Specifically, adding CNTs to a Ni matrix leads to a significant increase in the dislocation density up to $\rho \sim 4 \times 10^{16}\,\mathrm{m}^{-2}$ at 3 mm from the center (Fig. 5), which can be in turn observed as an increase in hardness (see Fig. 6).

Additionally, the difference in dislocation density between the center and the edge also increases with increasing strain and CNT content, which is related to an effective pinning of the grain boundaries by the CNT and possible delay in dislocation accumulation at the samples' centers during HPT.

Furthermore, the evolution of the dislocation character, as described by the edge dislocation fraction *fe* obtained from WPPM, is reported in Fig. 7 for the two studied sample's positions. It is observed that mainly screw dislocations accumulate far from the center during processing in both Ni samples and the composites. This can be explained as during plastic deformation, mainly dislocation tangles of edge character are arranging to form dislocation walls and screw dislocations locate primarily in the grain interiors and can be easily annihilated by cross slip [31–33]. Moreover, the application of high hydrostatic pressures during HPT mostly restricts the deformation-induced vacancies to reach the edge dislocations, reducing effectively
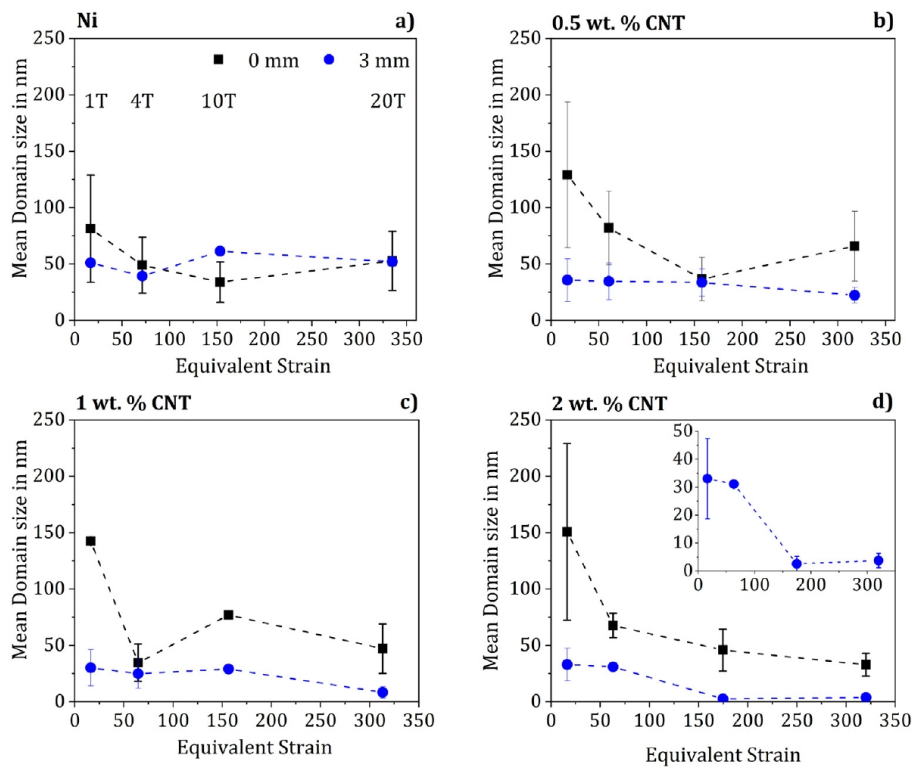

Fig. 4. Evolution of mean domain size for increasing equivalent strains and increasing number of turns (for the case of samples' centers where the equivalent strain is zero) in a) Ni, b) 0.5 wt% CNT, c) 1 wt% CNT and d) 2 wt% CNT.
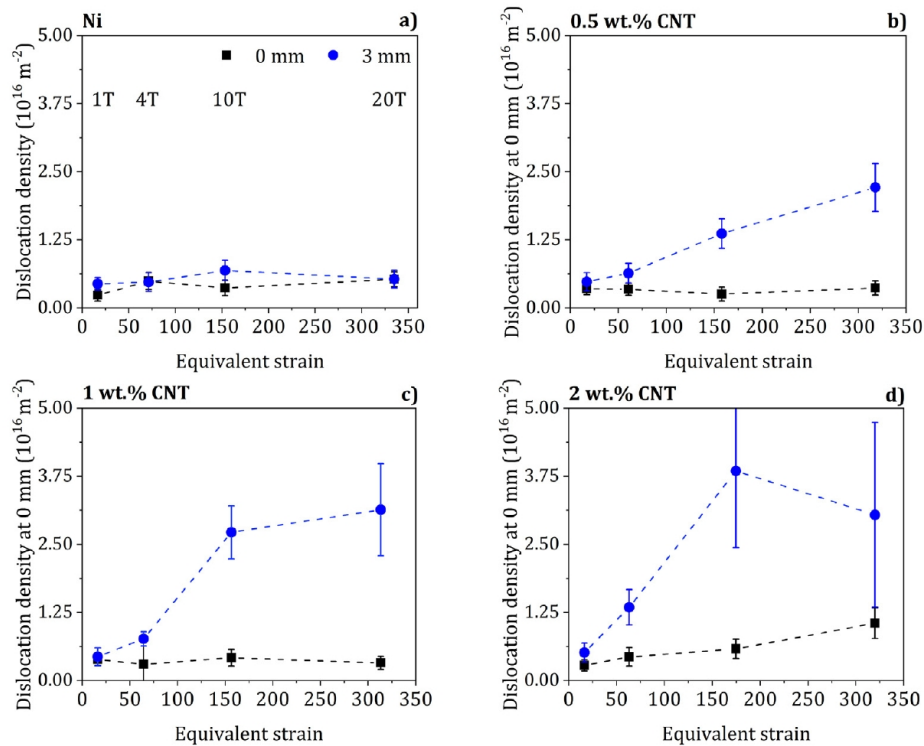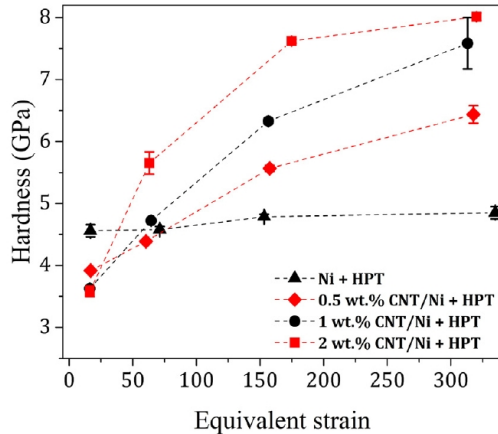
Katherine Aristizabal   86   Results and discussion

Fig. 5. Evolution of the dislocation density for increasing equivalent strains and increasing number of turns (for the case of samples' centers where the equivalent strain is zero) in a) Ni, b) 0.5 wt% CNT, c) 1 wt% CNT and d) 2 wt% CNT.

Fig. 6. Evolution of hardness (measured at 3 mm from the samples' centers) with increasing equivalent strains.

dislocation climb and annihilation [34,35]. By enhancing the dislocation density, there is an increase in the total grain boundary area, which corresponds to a decrease in the average grain size [36] that is equivalent to a decrease in the crystallite size as measured by XPA. Moreover, J. Gubicza et al. [37], suggested that the annihilation of both edge and screw dislocations is hindered during HPT more effectively in comparison to other SPD processing methods due to the high load applied, which delays both climb and cross-slip of dislocations. According to this, the increase in the screw dislocation character can be explained by the cross-slip of dislocations being hindered during HPT, with edge dislocations mainly arranging to contribute to the grain refinement of the material. Moreover, after releasing the hydrostatic pressure applied during processing, a release of excess vacancy concentration takes place

as proposed in [38], which promotes some dislocation annihilation, especially of edge character. In the sample's center the strain accumulates due to the inhomogeneous nature of the HPT process. Therefore, given that low misorientation angles of subgrains and even dipolar dislocation walls separating subgrains with no differences in orientation are "viewed" by XRD as crystalline domains [39], when the available edge dislocations arrange with increasing imposed strain into dislocation cells and sub-grains, these are in turn "seen" by XRD as new crystalline domains, which reduces the detection of edge dislocations located there.

Finally, different strengthening mechanisms can be accounted for the increase in hardness in the severely deformed composites such as strain hardening, grain size refinement (Hall-Petch) and dispersion strengthening (Orowan). However, it was observed that even though increasing carbon content increases the saturation value of hardness in Ni samples during HPT [40], increasing CNT content up to 2 wt% yielded similar saturation values of hardness in samples processed at room temperature, as opposed to higher processing temperatures, where CNT play an important role [7]. Moreover, it was observed that the increase in hardness of CNT-reinforced MMC followed a Hall-Petch relationship with small deviations at smaller grain sizes [7]. Nevertheless, as stated in [41], unless significant recovery of defects post deformation (or during deformation) occurs, there will be a correlation between dislocation density and the grain size and thus the linearity of a Hall-Petch type plot should not be taken as an indication that grain boundary strengthening dominates. The contribution of these three mechanisms to the strengthening was estimated and plotted in Fig. 8. Other contributions are considered negligible in comparison.

For the estimation of the grain boundary contribution via the Hall-Petch relation, it was assumed that crystalline domains act as obstacles for dislocation analogous to grain boundaries according to $\Delta\sigma = K\frac{1}{\sqrt{D}}$, where K was taken from the data compiled in [42] for nano-crystalline Ni assuming $\Delta\sigma = \frac{1}{3}\Delta Hardness$. Furthermore, the contribution of
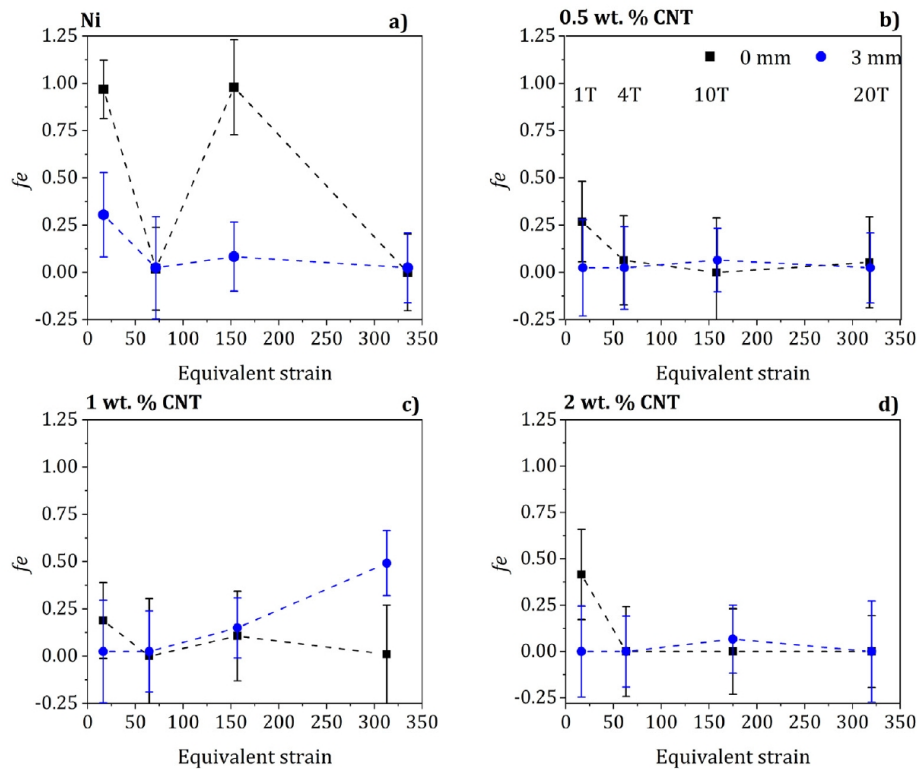
Fig. 7. Evolution of the edge dislocation fraction for increasing equivalent strains and increasing number of turns (for the case of samples' centers where the equivalent strain is zero) in a) Ni, b) 0.5 wt% CNT, c) 1 wt% CNT and d) 2 wt% CNT.

dislocation strengthening (work hardening) was estimated using the Taylor relation $\Delta\sigma = M\alpha Gb\sqrt{\rho}$, where M is the Taylor factor (~3), α is a constant taken as 0.24, G is the shear modulus G = 76.5 GPa, b is the Burgers vector b = 0.249 nm and ρ is the total dislocation density. Dispersion hardening due to the presence of CNT was estimated using the Orowan-Ashby relation $\Delta\sigma = \frac{0.13Gb}{d}In\frac{r}{b}$ [43], where d is the inter-particle distance, which was taken as the nearest neighbor distance calculated from the distance of the agglomerates centers of mass as described in [29], and r was taken as the agglomerate radius. It should be noted that the strengthening contributions remain an estimation and should not be taken as absolute values.

It has been shown that both work hardening and grain boundaries contribute to the strengthening in many metals [44] and composites [45] processed by SPD. This correlates well with the present results. Nevertheless, both dislocations and grain boundaries have comparable contribution to the strengthening, except where the domain sizes are the smallest and grain boundaries dominate due to the significantly smaller fraction of dislocations that can be stored inside the grains. Orowan strengthening, on the other hand, has only small contribution to the strengthening mainly because, even though the CNT agglomerate sizes and homogeneity was significantly improved during HPT [29], the agglomerate size is still large (~100 nm), which in many cases is bigger than the grain sizes, and because dislocation loops that may form around smaller agglomerates can eventually create dislocation cell structures, which in turn may result in a Hall-Petch type strengthening [43].

Based on the present results it can be concluded that the presence of CNT in CNT-MMC processed at room temperature by SPD with increasing CNT content and increasing imposed strain, increases the dislocation density (work hardening), assists the grain refinement and to a lesser extent contribute to particle strengthening via Orowan looping.

4. Conclusions

In summary, SPD of CNT/Ni matrix composites was studied by TEM and advanced X-ray diffraction analysis. The WPPM of diffraction data is capable of evidencing the variations in the microstructure of the specimens subjected to SPD and pointing out the microstructure refinement effect caused by the presence of CNT in the system. The saturation in the microstructural refinement is not reached during HPT at room temperature in the studied composites, as evidenced by the significant gradient in microstructure and hardness. Furthermore, an increase in the dislocation density in the system is evidenced with increasing number of turns. Moreover, the increase in the quantity of screw dislocations measured by WPPM, was attributed to the reduction of restoration processes due to the high applied hydrostatic load during HPT of CNT/MMC, with mainly edge dislocations contributing to the grain refinement. Finally, CNT are observed to promote the grain refinement significantly, as a consequence of the interaction of the nanotubes with grain boundaries and dislocations, which contribute significantly to the strengthening of the composites.

Data availability

Data will be provided upon reasonable request to the corresponding author.

Declaration of Competing Interest

The authors declare no conflict of interest.
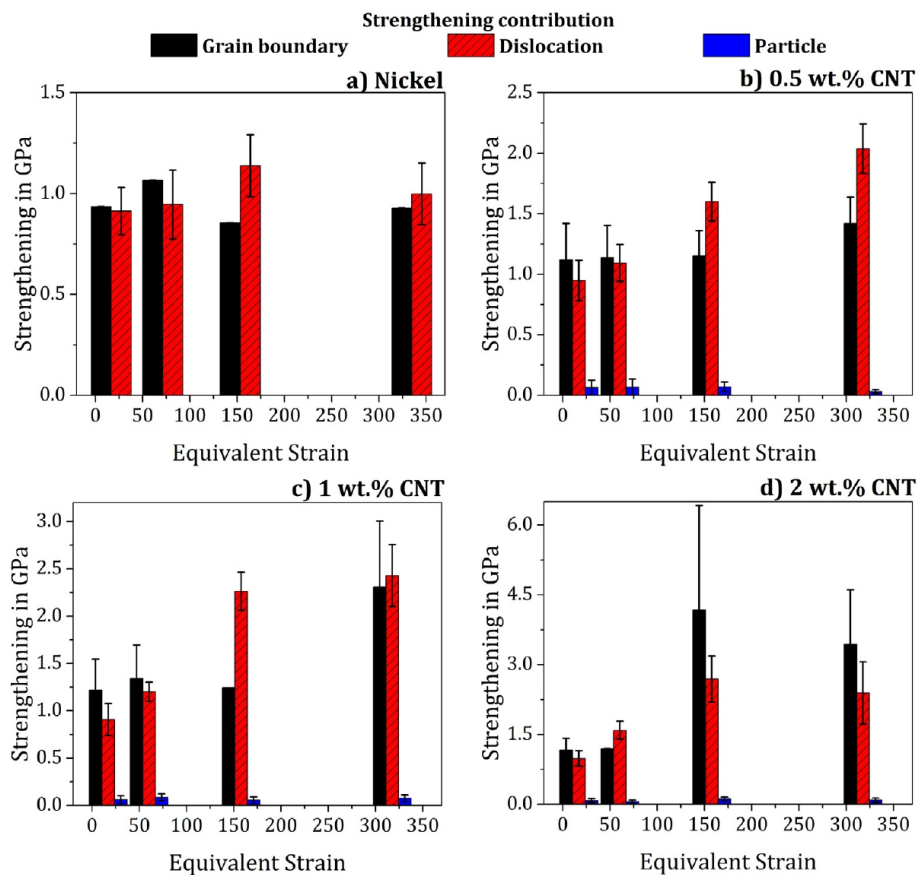
Acknowledgements

Fig. 8. Contribution from the respective strengthening mechanisms with increasing equivalent strains in in a) Ni, b) 0.5 wt% CNT, c) 1 wt% CNT and d) 2 wt% CNT.

References

[1] R.Z. Valiev, R.K. Islamgaliev, I.V. Alexandrov, Bulk nanostructured materials from severe plastic deformation, Prog. Mater. Sci. 45 (2000) 103–189, https://doi.org/10.1016/S0079-6425(99)00007-9.

[2] Y. Estrin, A. Molotnikov, C.H.J. Davies, R. Lapovok, Strain gradient plasticity modelling of high-pressure torsion, J. Mech. Phys. Solids 56 (2008) 1186–1202, https://doi.org/10.1016/j.jmps.2007.10.004.

[3] R. Pippan, S. Scheriau, A. Taylor, M. Hafok, A. Hohenwarter, A. Bachmaier, Saturation of fragmentation during severe plastic deformation, Annu. Rev. Mater. Res. 40 (2010) 319–343, https://doi.org/10.1146/annurev-matsci-070909-104445.

[4] H.W. Zhang, X. Huang, N. Hansen, Evolution of microstructural parameters and flow stresses toward limits in nickel deformed to ultra-high strains, Acta Mater. 56 (2008) 5451–5465, https://doi.org/10.1016/j.actamat.2008.07.040.

[5] H.P. Stüwe, Equivalent strains in severe plastic deformation, Adv. Eng. Mater. 5 (2003) 291–295, https://doi.org/10.1002/adem.200310085.

[6] K. Aristizabal, S. Suárez, A. Katzensteiner, A. Bachmaier, F. Mücklich, Evolution of the microstructure in carbon nanotube reinforced Nickel matrix composites processed by high-pressure torsion, IOP Conf. Ser. Mater. Sci. Eng. 258 (2017), https://doi.org/10.1088/1757-899X/258/1/012008.

[7] A. Katzensteiner, T. Müller, K. Kormout, K. Aristizabal, S. Suarez, R. Pippan, A. Bachmaier, Influence of processing parameters on the mechanical properties of HPT-deformed nickel/carbon nanotube composites, Adv. Eng. Mater. (2018)

1800422, https://doi.org/10.1002/adem.201800422.

[8] P. Scherrer, Bestimmung der Größe und der inneren Struktur von Kolloidteilchen mittels Röntgenstrahlen, Nachrichten von Der Gesellschaft Der Wissenschaften Zu Göttingen, Math. Klasse, (1918), pp. 98–100 http://resolver.sub.uni-goettingen.de/purl?GDZPPN002505045.

[9] B.E. Warren, B.L. Averbach, The effect of cold-work distortion on x-ray patterns, J. Appl. Phys. 21 (1950) 595–599, https://doi.org/10.1063/1.1699713.

[10] G.K. Williamson, W.H. Hall, X-ray line broadening from filed aluminium and wolfram, Acta Metall. 1 (1953) 22–31, https://doi.org/10.1016/0001-6160(53)90006-6.

[11] T. Ungár, I. Dragomir, Á. Révész, A. Borbély, The contrast factors of dislocations in cubic crystals: the dislocation model of strain anisotropy in practice, J. Appl. Crystallogr. 32 (1999) 992–1002, https://doi.org/10.1107/S0021889899009334.

[12] P. Jenei, E.Y. Yoon, J. Gubicza, H.S. Kim, J.L. Lábár, T. Ungár, Microstructure and hardness of copper-carbon nanotube composites consolidated by High Pressure Torsion, Mater. Sci. Eng. A 528 (2011) 4690–4695, https://doi.org/10.1016/j.msea.2011.02.066.

[13] T. Shintani, Y. Murata, Evaluation of the dislocation density and dislocation character in cold rolled Type 304 steel determined by profile analysis of X-ray diffraction, Acta Mater. 59 (2011) 4314–4322, https://doi.org/10.1016/j.actamat.2011.03.055.

[14] J. Gubicza, N.H. Nam, L. Balogh, R.J. Hellmig, V.V. Stolyarov, Y. Estrin, T. Ungár, Microstructure of severely deformed metals determined by X-ray peak profile analysis, J. Alloys Compd. 378 (2004) 248–252, https://doi.org/10.1016/j.jallcom.2003.11.162.

[15] J. Gubicza, L. Balogh, R.J. Hellmig, Y. Estrin, T. Ungár, Dislocation structure and crystallite size in severely deformed copper by X-ray peak profile analysis, Mater. Sci. Eng. A 400–401 (2005) 334–338, https://doi.org/10.1016/j.msea.2005.03.042.

[16] T. Ungár, J. Gubicza, P. Hanák, I. Alexandrov, Densities and character of dislocations and size-distribution of subgrains in deformed metals by X-ray diffraction profile analysis, Mater. Sci. Eng. A 319–321 (2001) 274–278, https://doi.org/10.1016/S0921-5093(01)01025-5.

[17] P. Scardi, M. Leoni, Whole powder pattern modelling, Acta Crystallogr. Sect. A Found. Crystallogr. 58 (2002) 190–200, https://doi.org/10.1107/S0108767301021298.

[18] M.A. Krivoglaz, X-ray and Neutron Diffraction in Nonideal Crystals, Springer-Verlag, Berlin, 1996, https://doi.org/10.1007/978-3-642-74291-0.

[19] G.K. Williamson, R.E. Smallman, III. Dislocation densities in some annealed and cold-worked metals from measurements on the X-ray Debye-Scherrer spectrum, Philos. Mag. 1 (1956) 34–46, https://doi.org/10.1080/14786435608238074.

[20] A.R. Kil'mametov, R.Z. Valiev, R.K. Islamgaliev, G.V. Nurislamova, Structural features of nanocrystalline nickel subjected to high-pressure torsion, Phys. Met. Metallogr. 101 (2006) 75–82, https://doi.org/10.1134/s0031918x06010108.

[21] Z. Yang, U. Welzel, Microstructure-microhardness relation of nanostructured Ni produced by high-pressure torsion, Mater. Lett. 59 (2005) 3406–3409, https://doi.org/10.1016/j.matlet.2005.05.077.

[22] L. Reinert, M. Zeiger, S. Suárez, V. Presser, F. Mücklich, Dispersion analysis of carbon nanotubes, carbon onions, and nanodiamonds for their application as reinforcement phase in nickel metal matrix composites, RSC Adv. 5 (2015) 95149–95159, https://doi.org/10.1039/C5RA14310A.

[23] P. Scardi, M. Ortolani, M. Leoni, WPPM: microstructural analysis beyond the Rietveld method, Mater. Sci. Forum 651 (2010) 155–171, https://doi.org/10.4028/www.scientific.net/MSF.651.155.

[24] M. Leoni, T. Confente, P. Scardi, PM2K: a flexible program implementing Whole Powder Pattern Modelling, Zeitschrift Fur Krist. Suppl. (2006) 249–254.

[25] J. Martinez-Garcia, M. Leoni, P. Scardi, A general approach for determining the diffraction contrast factor of straight-line dislocations, Acta Crystallogr. Sect. A Found. Crystallogr. 65 (2009) 109–119, https://doi.org/10.1107/S010876730804186X.

[26] P. Scardi, M. Leoni, M. D'Incau, Whole Powder Pattern Modelling of cubic metal powders deformed by high energy milling, Zeitschrift Fur Krist. 222 (2007) 129–135, https://doi.org/10.1524/zkri.2007.222.3-4.129.

[27] A. Bachmaier, A. Hohenwarter, R. Pippan, New procedure to generate stable nanocrystallites by severe plastic deformation, Scr. Mater. 61 (2009) 1016–1019, https://doi.org/10.1016/j.scriptamat.2009.08.016.

[28] J. Guo, M.J. Duarte, Y. Zhang, A. Bachmaier, C. Gammer, G. Dehm, R. Pippan, Z. Zhang, Oxygen-mediated deformation and grain refinement in Cu Fe nanocrystalline alloys, Acta Mater. 166 (2018) 281–293, https://doi.org/10.1016/j.actamat.2018.12.040.

[29] K. Aristizabal, A. Katzensteiner, A. Bachmaier, F. Mücklich, S. Suárez, On the reinforcement homogenization in CNT/metal matrix composites during severe plastic deformation, Mater. Charact. 136 (2018) 375–381, https://doi.org/10.1016/j.matchar.2018.01.007.

[30] D. Setman, E. Schafler, E. Korznikova, M.J. Zehetbauer, The presence and nature of vacancy type defects in nanometals detained by severe plastic deformation, Mater. Sci. Eng. A 493 (2008) 116–122, https://doi.org/10.1016/j.msea.2007.06.093.

[31] J. Kratochvil, S. Libovicky, Dipole drift mechanism of early stages of dislocation pattern formation in deformed metal single crystals, Scr. Metall. 20 (1986) 1625–1630.

[32] A.A. Kusov, V.I. Vladimirov, The theory of dynamic annihilation of dislocations, Phys. Status Solidi 138 (1986) 135–142, https://doi.org/10.1002/pssb.2221380114.

[33] U. Essmann, H. Mughrabi, Philos. Mag. A 40 (1979) 731–756, https://doi.org/10.1080/01418617908234871.

[34] M.J. Zehetbauer, J. Kohout, Principles and modeling of severe plastic deformation providing ultra fine grained materials, Plast. Damage Fract. Macro, Micro Nano Scales, Plast. Int. Symp. Plast. Its Curr. Appl. 9, NEAT Press, Fulton, 2002, pp. 543–545.

[35] M.J. Zehetbauer, H.P. Stüwe, A. Vorhauer, E. Schafler, J. Kohout, The role of hydrostatic pressure in severe plastic deformation, Adv. Eng. Mater. 5 (2003) 330–337, https://doi.org/10.1002/adem.200310090.

[36] M.J. Zehetbauer, Y. Estrin, Modeling of strength and strain hardening of bulk nanostructured materials, in: M.J. Zehetbauer, Y. Zhu (Eds.), Bulk Nanostructured Mater, WILEY-VCH Verlag, 2009, pp. 109–136.

[37] J. Gubicza, S.V. Dobatkin, E. Khosravi, A.A. Kuznetsov, J.L. Lábár, Microstructural stability of Cu processed by different routes of severe plastic deformation, Mater. Sci. Eng. A 528 (2011) 1828–1832, https://doi.org/10.1016/j.msea.2010.11.026.

[38] M. Zehetbauer, B. Jóni, G. Tichy, E. Schafler, T. Ungár, Correlation between the microstructure studied by X-ray line profile analysis and the strength of high-pressure-torsion processed Nb and Ta, Acta Mater. 61 (2012) 632–642, https://doi.org/10.1016/j.actamat.2012.10.008.

[39] T. Ungár, G. Tichy, J. Gubicza, R.J. Hellmig, Correlation between subgrains and coherently scattering domains, Powder Diffract. 20 (2005) 366–375, https://doi.org/10.1154/1.2135313.

[40] G.B. Rathmayr, R. Pippan, Influence of impurities and deformation temperature on the saturation microstructure and ductility of HPT-deformed nickel, Acta Mater. 59 (2011) 7228–7240, https://doi.org/10.1016/j.actamat.2011.08.023.

[41] M.J. Starink, Dislocation versus grain boundary strengthening in SPD processed metals: non-causal relation between grain size and strength of deformed polycrystals, Mater. Sci. Eng. A 705 (2017) 42–45, https://doi.org/10.1016/j.msea.2017.08.069.

[42] R.W. Armstrong, N. Balasubramanian, Unified Hall-Petch description of nano-grain nickel hardness, flow stress and strain rate sensitivity measurements, AIP Adv. 7 (2017) 1–6, https://doi.org/10.1063/1.4996294.

[43] G.E. Dieter, Strengthening from fine particles, Mech. Metall, McGraw-Hill, New York, USA, 1986, pp. 212–220.

[44] J. Gubicza, Correlation between defect structure and mechanical properties of nanocrystalline materials, Defect Struct. Prop. Nanomater, 2012, pp. 167–221.

[45] J. Gubicza, Defect structure and mechanical properties of metal matrix–carbon nanotube composites, Defect Struct. Prop. Nanomater, 2012, pp. 231–257.

Katherine Aristizabal   90   Results and discussion

V. Microstructural evolution during heating of CNT/Metal Matrix Composites processed by Severe Plastic Deformation

Katherine Aristizabal[1], Andreas Katzensteiner[2], Andrea Bachmaier[2], Frank Mücklich[1], Sebastián Suárez[1]

1 Department of Material Science and Engineering, Saarland University,
66123 Saarbrücken, Germany
2 Erich Schmid Institute, Austrian Academy of Sciences, Jahnstrasse 12, 8700 Leoben, Austria

Own Contribution: Project management, sample manufacturing and processing, experimental execution, data analysis, conceptualization of experimental results and calculations, manuscript writing.

Abstract:

Carbon nanotube reinforced nickel matrix composites (Ni/CNT) with different CNT compositions were fabricated by solid state processing and subjected to severe plastic deformation (SPD) by means of high pressure torsion (HPT). A thorough study on the microstructural changes during heating and on the thermal stability was performed using differential scanning calorimetry (DSC), high temperature X-ray diffraction (HT-XRD) and electron backscattered

diffraction (EBSD). Furthermore, the formation and dissolutions of the metastable nickel carbide Ni_3C phase was evidenced by DSC and HT-XRD in composites with sufficient carbon atoms available as a consequence of irreversible damage on the CNT introduced by HPT. Finally, it was shown that the composites exhibited an improved thermal stability with respect to nickel samples processed under the same conditions, with a final grain size dependent on the CNT volume fraction according to a $V_{CNT}^{-1/3}$ relationship and that lied within the ultrafine grained range.

OPEN

Microstructural evolution during heating of CNT/Metal Matrix Composites processed by Severe Plastic Deformation

Katherine Aristizabal[1]*, Andreas Katzensteiner[2], Andrea Bachmaier[2], Frank Mücklich[1] & Sebastian Suárez[1]*

Carbon nanotube reinforced nickel matrix composites (Ni/CNT) with different CNT compositions were fabricated by solid state processing and subjected to severe plastic deformation (SPD) by means of high pressure torsion (HPT). A thorough study on the microstructural changes during heating and on the thermal stability was performed using differential scanning calorimetry (DSC), high temperature X-ray diffraction (HT-XRD) and electron backscattered diffraction (EBSD). Furthermore, the formation and dissolution of the metastable nickel carbide Ni_3C phase was evidenced by DSC and HT-XRD in composites, where sufficient carbon atoms are available, as a consequence of irreversible damage on the CNT introduced by HPT. Finally, it was shown that the composites exhibited an improved thermal stability with respect to nickel samples processed under the same conditions, with a final grain size dependent on the CNT volume fraction according to a $V_{CNT}{}^{-1/3}$ relationship and that lied within the ultrafine grained range.

Ultrafine-grained (UFG) and nanocrystalline (NC) materials obtained by severe plastic deformation (SPD) have been subject of intensive study due to their interesting functional and enhanced mechanical properties[1,2]. However, the high amount of stored energy stemming from a large grain boundary area and a high density of lattice defects makes them thermally unstable at lower temperatures relative to the coarse grained counterparts[2,3], which may be a limiting factor for potential applications. Many studies have been performed on the thermal stability of these materials in order to better understand the mechanisms involved and to develop ways to overcome this drawback[4–7]. It has been shown that the stored energy of defects increases with the imposed strain during SPD, which decreases the temperature for the onset of recovery of such defects[8]. Furthermore, it has been observed that the behavior during heating of NC and UFG materials differs significantly from that of coarse polycrystalline ones. For instance, NC and UFG show usually different behavior during grain growth at low temperatures (typically <300 °C) than at higher ones[9–15]. This is mainly because at low temperatures recovery and recrystallization processes occur, which exhibit different activation energies than grain growth processes taking place at higher temperatures. Additionally, NC and UFG may also exhibit abnormal grain growth[16]. A study from G. K. Rane *et al.* about the grain growth on NC Ni powder produced by ball milling[15], showed that upon annealing, rapid grain growth occurs at the beginning with almost total annihilation of microstrain, where with longer annealing times, the course of grain growth depends on the initial microstructure, exhibiting linear growth in the whole temperature range studied (in the case of samples with the larger microstrain and narrower grain size distributions). Such effects were found to be incompatible with grain-boundary curvature driven growth, including the "generalized parabolic grain growth model", i.e. $D(t)^n - D(0)^n = k_1 t$, (where: D(t) is the grain size at a time t, D(0) is the initial grain size, k_1 is the rate constant proportional to the grain boundary Mobility M and n is the grain growth exponent) and even a grain growth model including a growth retarding contribution from impurities along the grain boundaries (Zener-Drag), did not fit well the studied data[15].

Some efforts to improve the thermal stability have been made, including the addition of alloying elements and second phases to metallic matrices[17–19]. Carbon Nanotubes (CNT) have proven to be promising reinforcing

[1]Chair of Functional Materials, Department of Materials Science, Saarland University, D-66123, Saarbrücken, Germany. [2]Erich Schmid Institute of Materials Science, Austrian Academy of Sciences, Jahnstrasse 12, A-8700, Leoben, Austria. *email: katherine.aristizabal@uni-saarland.de; s.suarez@mx.uni-saarland.de
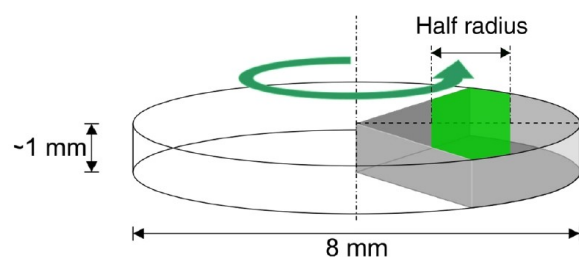
Figure 1. Schematic of DSC and HT-XRD test specimens taken from a HPT disc. Sample size of approximately 2 mm (along the radius ~ 1–3 mm).
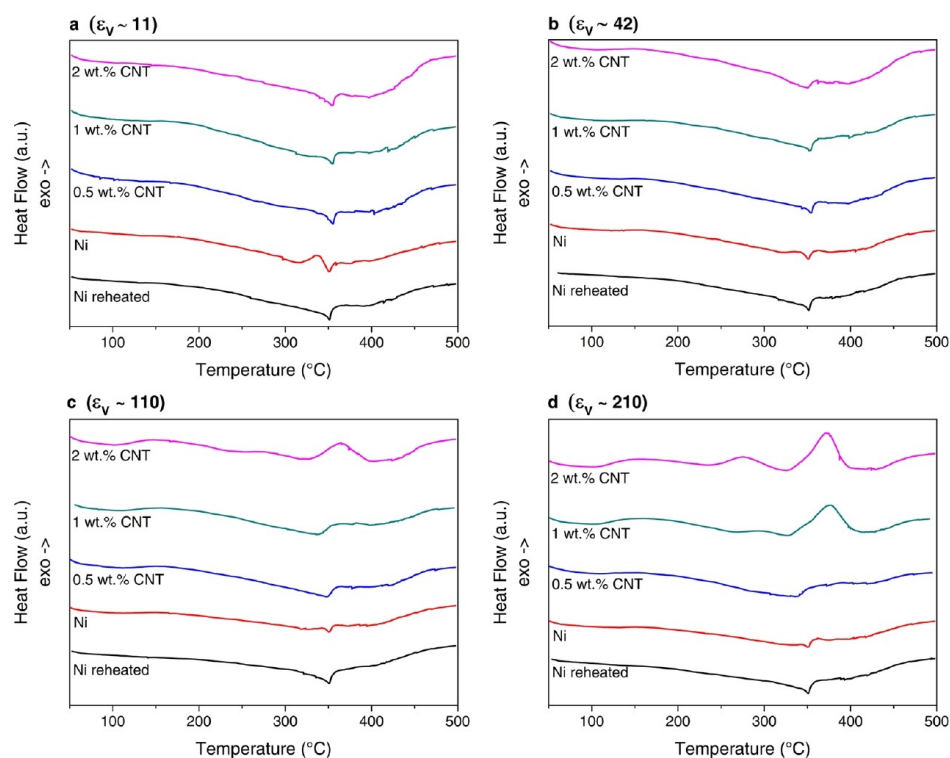

Figure 2. DSC curves recorded for a temperature range of 40–500 °C and a heating rate of 15 °C/min. After HPT at RT with (**a**) 1 T, (**b**) 4 T, (**c**) 10 T and (**d**) 20 T. Respective applied equivalent strains shown in each figure.

phase due to their outstanding physical properties. Therefore, the thermal stability of such composites processed by SPD is expected to increase with respect to their matrix counterparts. Nevertheless, it has been observed that processing CNT-reinforced metal matrix composites (MMC) has some technical limitations. For instance, applying extremely high strains may induce structural damage on the CNT, which might lead to their amorphization[20]. Albeit the technical issues stemming from the difficulty to disperse CNT agglomerates effectively due to strong Van der Waals interaction, this drawback can be solved, to some extent, by SPD of the CNT-MMC. In fact, it was observed that there is a minimum strain that should be applied in order to obtain a homogenous distribution of the CNT[21]. Even though impurities and second phases can improve the thermal stability of MMC processed by SPD, UFG and NC CNT-MMC obtained by high pressure torsion (HPT) of bulk samples, possess a high density of defects and large grain boundary area, and thus, a high stored energy[22], which may render them highly unstable when subjected to heat treatments. It is therefore important to study the evolution of the microstructure during and upon heating of such composites in order to determine to what extent the CNT can stabilize the microstructure against grain growth.

In this work, a thorough study was performed on the microstructural changes during heating and post annealing of CNT/Ni matrix composites, increasing the CNT content and the equivalent strain, comparing the results to bulk Ni samples deformed by HPT with the same parameters. Different characterization techniques were used,
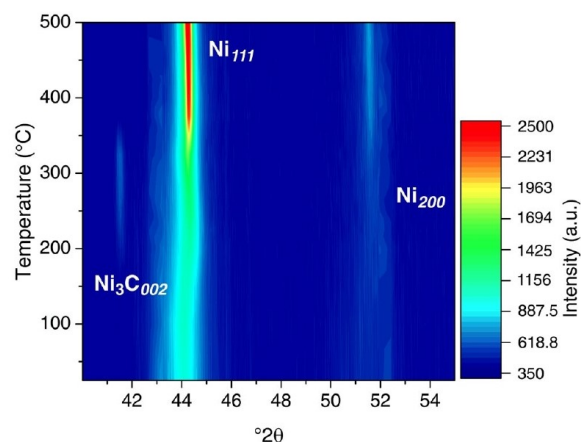
Figure 3. Color-coded plot of the sample 2 wt. %CNT deformed by HPT with an applied equivalent strain of $\varepsilon_v \sim 210$, showing the evolution of the studied 2θ range during HT-XRD.
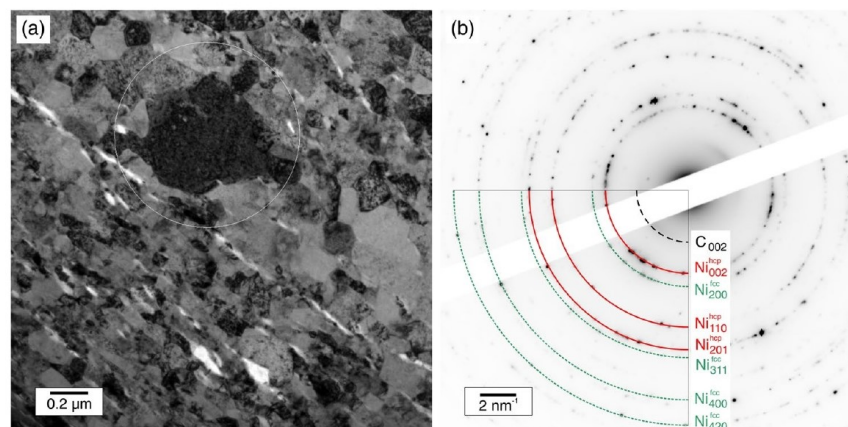

Figure 4. (**a**) TEM micrograph and (**b**) SAED pattern of the region marked in a, performed on the sample 2 wt. %CNT deformed by HPT with an applied equivalent strain of $\varepsilon_v \sim 210$, after DSC.

such as Differential Scanning Calorimetry (DSC), High Temperature X-ray diffraction (HT-XRD), Transmission electron microscopy (TEM) and Electron Backscattered diffraction (EBSD).

Materials and Methods

Materials. By means of colloidal mixing, powder mixtures were obtained from the starting materials (i.e. MWCNT - CCVD grown, Graphene Supermarket, USA density 1.84 g/cm³ and dendritic Ni powder (Alfa Aesar, mesh −325, 99.8% purity). These mixtures were subsequently cold pressed (990 MPa) and sintered under vacuum (2.0×10^{-6} mbar) at 900 °C for 3 h. A thorough description of the colloidal mixing process can be found elsewhere[23].

Sample processing. Sintered samples were further processed by means of HPT. CNT/Ni composites were deformed at room temperature using different number of turns, namely 1, 4, 10 and 20 T applying 4 GPa of pressure and 0.2 rpm. The equivalent strain can be written as $\varepsilon_v = \frac{2\pi Tr}{t\sqrt{3}}$, where T is the number of turns, t is the sample thickness and r is the distance from the center of the sample[24]. Different CNT fractions were used, namely 0.5, 1, and 2 wt. % (2.4, 4.7 and 9 vol. %, respectively). Pure Ni samples were also processed and analyzed as a reference state. Samples for DSC were cut in pieces containing the half radius of the samples (see Fig. 1.) using a high precision diamond wire, in order to adjust the samples to the size of the aluminum pans. The same sample preparation was implemented for the HT-XRD measurements in order to keep consistency.

Differential scanning calorimetry. DSC was carried out using a Q2000 calorimeter (TA Instruments), using a heating rate of 15 °C/min and a Ni/Ar (50 ml/min) controlled environment, measuring the heat flow from 40 to 500 °C.
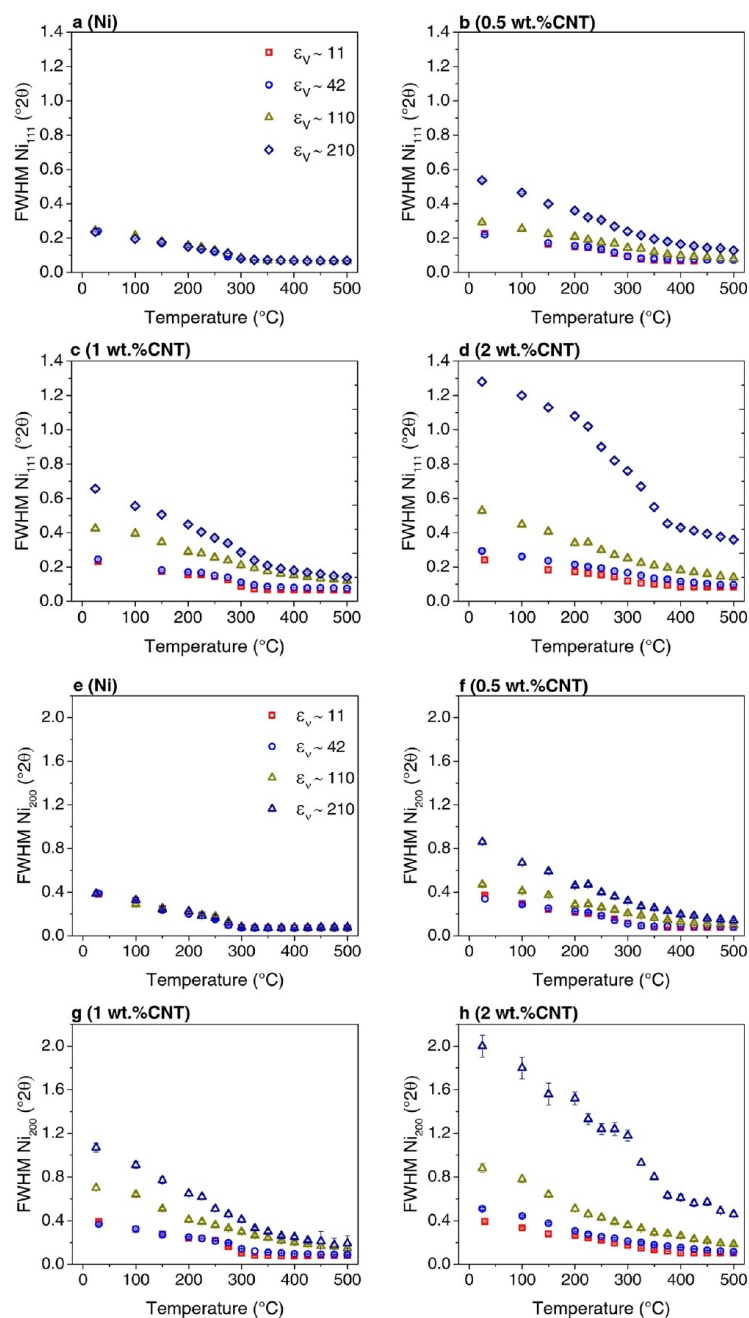
Figure 5. Evolution of the Ni_{111} (**a–d**) and Ni_{200} (**e–h**) reflections during heating by means of HT-XRD, recorded from 25 to 500 °C with a heating rate of 15 °C/min.

High temperature X-ray diffraction. HT-XRD measurements were carried out using an Anton Paar HTK1200 HT-chamber at 10^{-6} mbar mounted in a PANalytical X'Pert MPD X-ray diffractometer. Diffractograms for the Ni_{111} and Ni_{200} reflections were recorded with increasing temperature as follows: room temperature, 150 °C, 200 °C and afterwards every 25 °C after 5 minutes of thermal homogenization up to 500 °C, using a heating rate of 15 °C/min.
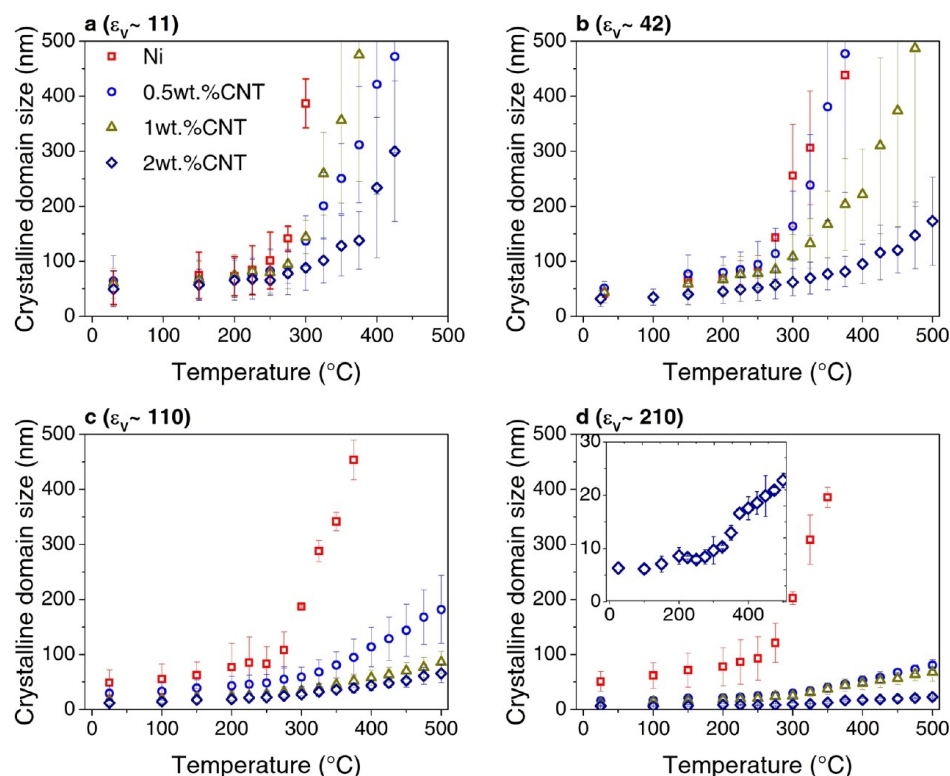
Figure 6. Average crystalline domain size evolution with temperature in samples deformed to (**a**) $\varepsilon_\nu \sim 11$, (**b**) $\varepsilon_\nu \sim 42$, (**c**) $\varepsilon_\nu \sim 110$ and (**d**) $\varepsilon_\nu \sim 210$.

Transmission electron microscopy. TEM was performed by means of a JEOL JEM 2010 using 200 kV on a selected sample after DSC, namely a sample containing 2 wt. % CNT deformed by HPT using 20 T, which had shown the peak related to the decomposition of Ni_3C.

Electron backscattered diffraction. EBSD of the extrema processing conditions (i.e. after 1 and 20 turns) after HT-XRD was performed with a step size of 50 nm, on a dual beam system Helios NanoLab^{TM} 600 (FEI) with an attached EDAX TSL^{TM} module using 20 kV and 22 nA. Moreover, samples after annealing were also analyzed by means of EBSD using the same equipment, where the step size was varied according to the respective grain size, so that at least 6 points were to be measured within a grain. The data were processed using the EBSD data analysis software OIM 7^{TM}, whereby a region of at least two adjacent points with a maximum misorientation angle of 5° was defined as a grain. Furthermore, a confidence index (CI) standardization across grains was performed, and noisy data, using a cut-off of CI = 0.09 were removed. For grain size calculations, edge grains were excluded from the analysis.

Results and Discussion

Differential scanning calorimetry. Figure 2 shows the evolution of the DSC curves for the Ni samples and the composites for the different deformation conditions. Curves of reheated Ni samples are also displayed in order to illustrate the reversible changes occurring during DSC. It can be observed that different thermal events took place during heating. The appearance of two exothermic peaks in the ranges of 100–180 °C and 200–320 °C was reported in DSC curves of Ni processed by HPT[4,5]. The first peak corresponds to the annealing of vacancies and the second to the annihilation of dislocations and activation of recrystallization[4]. Moreover, the peak related to the annihilation of dislocations overlaps with the annihilation of vacancy agglomerates and shifts to lower temperatures while the vacancy peak remains more or less constant with increasing strain[5]. Furthermore, there is an endothermic spike around 350 °C, which corresponds to the magnetic transition of Ni (i.e. the Curie temperature). The composites containing the region deformed to $\varepsilon_\nu \sim 11$ and $\varepsilon_\nu \sim 42$, behaved in a similar manner and in contrast to the corresponding Ni samples (see Fig. 2a,b), the composites showed a much lower energy release regarding the dislocation peak, which evidences their better thermal stability by the presence of CNT. With increasing strain, Ni samples also showed a lower energy release (Fig. 2b–d), which may be related to dynamic recovery processes having taking place during deformation, and/or static recovery taking place upon unloading of the samples.
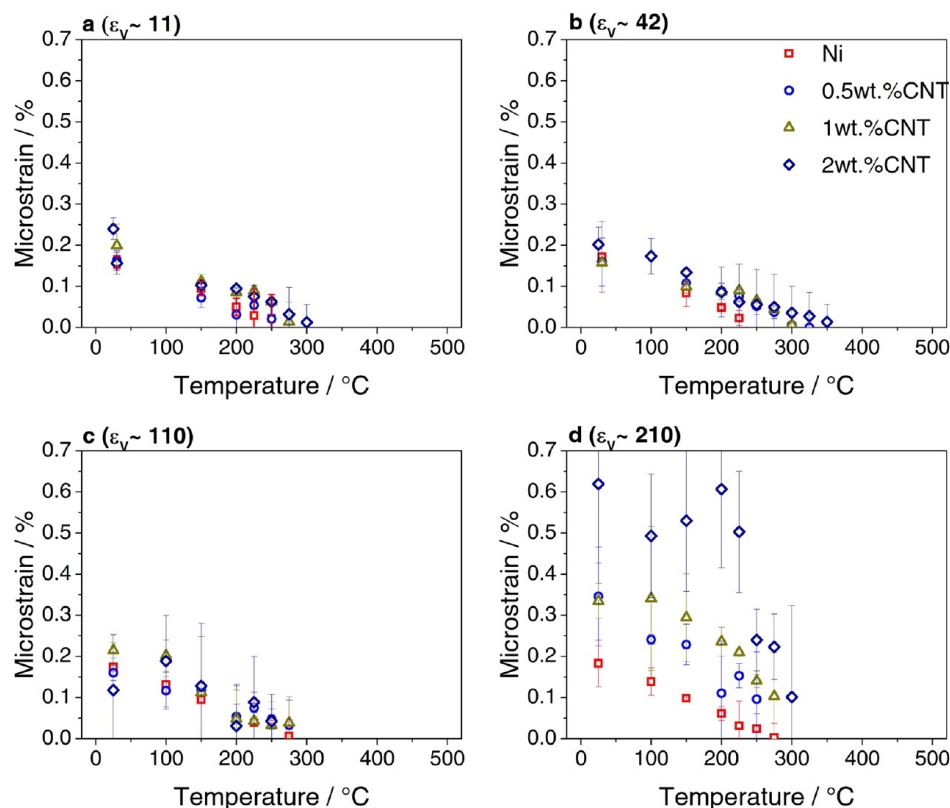
Figure 7. Average microstrain evolution with temperature in samples deformed to (**a**) $\varepsilon_\nu \sim 11$, (**b**) $\varepsilon_\nu \sim 42$, (**c**) $\varepsilon_\nu \sim 110$ and (**d**) $\varepsilon_\nu \sim 210$.

In addition, an exothermic event appears in some composites ($\varepsilon_\nu \sim 110$: 2 wt. % CNT; $\varepsilon_\nu \sim 210$: 1 wt. % CNT and 2 wt. % CNT. see Fig. 2c,d) at around 350 °C. This exothermic peak is attributed to the decomposition of nickel carbide (Ni_3C). Such peak has been previously observed in the course of decomposition of Ni_3C[25,26]. Furthermore, the presence of the metastable Ni_3C was detected between 200 °C and 350 °C during HT-XRD performed in the same samples (see Fig. 3). Since the formation of this metastable carbide is of endothermic nature, it might affect the observation of other exothermic events happening within this temperature range.

High temperature X-ray diffraction. HT-XRD offers the possibility of studying *in-situ* the microstructural changes and phase transitions during heating. One important observation from *in-situ* XRD results is the formation and dissolution of Ni_3C in the corresponding above mentioned composites. The formation of nickel carbide was observed in the course of deformation by ball milling of Ni-C mixtures[27]. Nevertheless, in the present study no carbide signal was detected from XRD in the initial state after HPT[22]. However, it is expected that sufficient C atoms may be available in the composites after HPT as impurities, being a consequence of irreversible damage introduced on the CNT during processing[20]. In the course of heating of the corresponding composites, a peak appears at a 2-Theta of ~41.5° between 200 to 350 °C (see Fig. 3). This XRD peak was assigned to Ni_3C and disappears above 350 °C, which corresponds to the onset temperature of carbide decomposition (see Fig. 2c,d) when it dissolves ($Ni_3C \rightarrow 3Ni + C$). Ni_3C has a metastable nature and decomposes at sufficiently high temperatures probably due to an increase of surface diffusivity and weak nature of Ni-C bond[28]. Further examination by means of TEM (see Fig. 4a,b) enabled the identification of regions containing a stabilized Ni hcp, (whose signal is marked in red in Fig. 4b), which usually acts as a witness phase of the formation and subsequent degradation of the Ni_3C[26].

Another feature in Fig. 3 is the shifting of the Ni_{111} peak. During heating, the XRD lines shift to the left due to lattice thermal expansion. Nevertheless, the initial Ni_{111} peak position was located at a lower angle in the as deformed state, with respect to the theoretical Ni_{111} position, most probably due to residual stresses introduced during the HPT, which are released upon heating while the peak shifts to the right. Moreover, most of the stress is released up to 200 °C and at higher temperatures the peak does not significantly shifts most likely because of stress release and thermal expansion occurring simultaneously.

Furthermore, x-ray line profile analysis (XPA) can be performed in order to extract information about the evolution of the crystalline domain size and the microstrain (See supplementary information for further details).
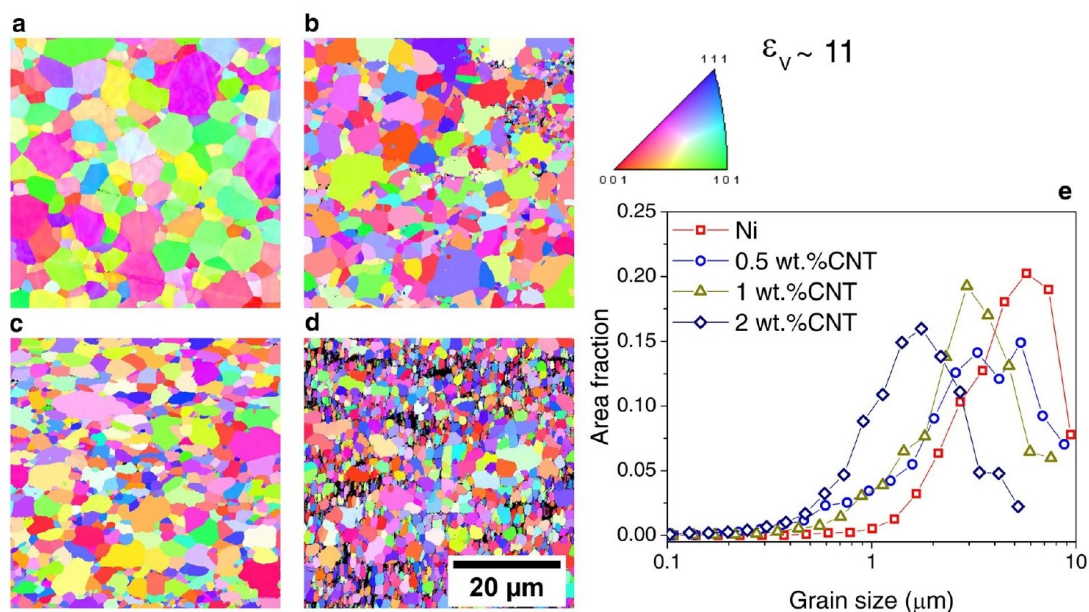
Figure 8. Inverse pole figures of samples deformed by HPT with $\varepsilon_v \sim 11$ after ramp annealing (by HT-XRD in) (**a**) Ni, (**b**) 0.5 wt. %CNT, (**c**) 1 wt. %CNT and (**d**) 2 wt. %CNT; **e**) Grain size distributions of the same samples. Scale shown in d is common to all the images.
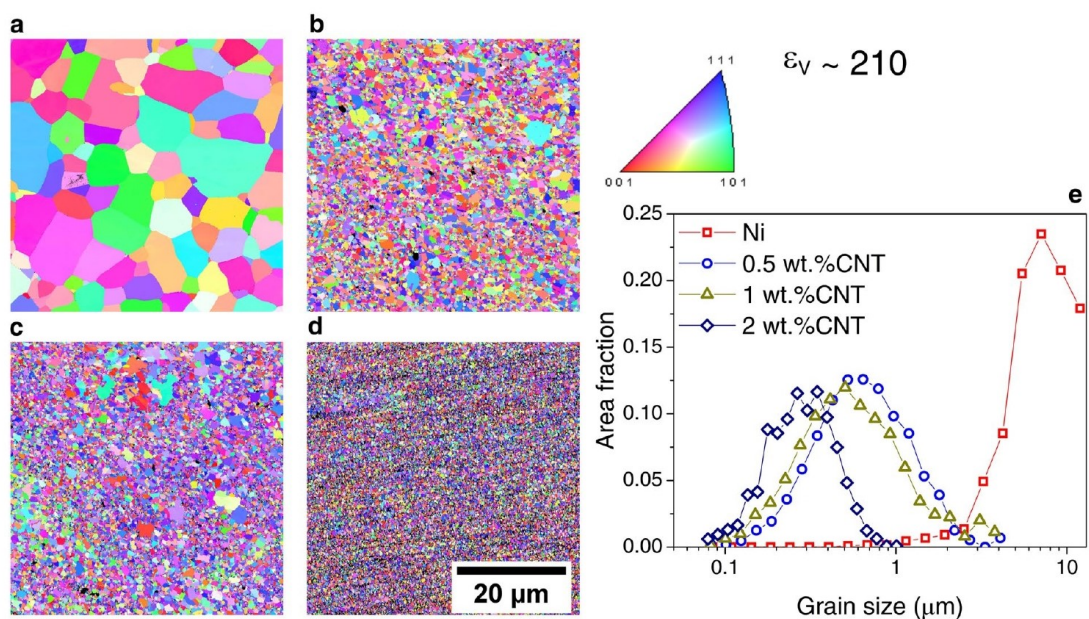

Figure 9. Inverse pole figures of samples deformed by HPT with $\varepsilon_v \sim 210$ after ramp annealing (by HT-XRD) in (**a**) Ni, (**b**) 0.5 wt. %CNT, (**c**) 1 wt. %CNT and (**d**) 2 wt. %CNT; (**e**) Grain size distributions of the same samples. Scale shown in d is common to all the images.

In the present study only the first two Ni reflections were measured (i.e. Ni_{111} and Ni_{200}), because during isothermal holds microstructural changes occur continuously making the time for each XRD measurement very limited. Therefore, line profile analysis using the whole profile, in methods such as Whole Powder Pattern Modelling (WPPM)[29], cannot be used in this case. According to this, the integral breadth method using single-line analysis[30]
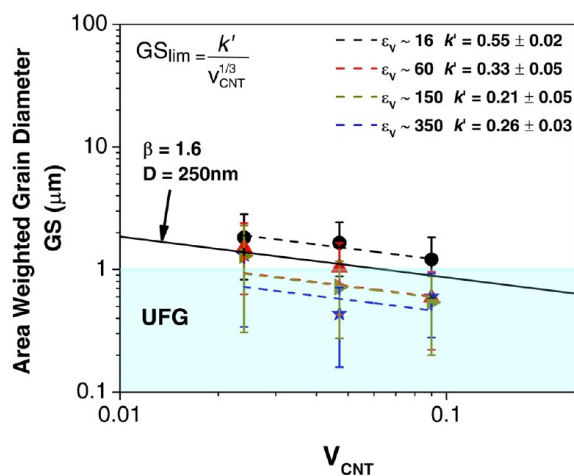
Figure 10. Symbols correspond to the average grain sizes obtained from EBSD after 12 h annealing at 500 °C. The dashed lines correspond to the respective Zener model. The UFG region is shown. The values for k' for the corresponding equivalent strains are presented in the graphic. A reference line is plotted using an average CNT agglomerate size D = 250 nm and a geometric constant of β = 1.6 as in ref. [32].

was used in order to estimate the crystalline domain size and the microstrain changes during heating of the studied composites with respect to the Ni samples. In this regard, Fig. 5a–h shows the evolution with temperature of the measured full width at half maximum (FWHM) for the peaks Ni_{111} and Ni_{200}, respectively. Ni samples behave all in the same manner and reach the minimum FWHM at about 300 °C. These results suggest that regardless of the initial accumulated imposed strain during HPT in bulk Ni samples and of the initial stored energy (see Fig. 2), there is no change in the recovery rate, at least as detected by the changes in the XRD line broadening (see Fig. 5a–e). In fact, grain growth start to happen at 250 °C in all the Ni samples (see Fig. 6). Nevertheless, the minimum microstrain, as estimated by XPA, was reached at higher temperatures in samples containing the region deformed to $\varepsilon_\nu \sim 110$ and $\varepsilon_\nu \sim 210$ (~280 °C), which also had lower energy release (see Fig. 2c,d), with respect to samples $\varepsilon_\nu \sim 11$ and $\varepsilon_\nu \sim 42$, in which the minimum microstrain occurs at ~250 °C (see Fig. 7).

Moreover, it was shown in a previous study that increasing the equivalent strain and the CNT content leads to a decrease in the crystalline domain size and an increase in the dislocation density (associated to microstrain)[22]. Accordingly, the FWHM increases with equivalent strain and CNT content (Fig. 5). In the composites deformed to equivalent strains $\varepsilon_\nu \sim 11$ and $\varepsilon_\nu \sim 42$, the evolution with temperature of the FWHM does not change significantly in samples with the same CNT content. Nevertheless, the grain growth rate (analogous to crystallite size) decreases with increasing CNT content (see Fig. 6), and it takes place when the recovery (as described by the decrease in microstrain with increasing temperature) has finished (see Fig. 7). In other words, the recrystallization and grain coarsening is retarded while the recovery process takes place, i.e. during annealing and rearrangement of dislocations. Furthermore, the carbide formation has an effect on the evolution of both the crystalline domain size and the microstrain. In fact, it can be observed in the insert of Fig. 6d, which is a magnified image on the evolution of crystallite size for the sample 2 wt. % CNT, that between 200–350 °C the growth rate is zero and afterwards increases. Additionally, between 100–200 °C there is a slight increase in the microstrain and after 200 °C the microstrain decreases quickly (also note the respective FWHM changes in Figs. 5,d and 5h). This can be related to an increase in the amount of dislocations, which are being generated during the formation of the carbide probably due to CTE mismatch between the carbide and the nickel matrix, and while the microstrain decreases, the growth rate is retarded.

Samples deformed to $\varepsilon_\nu \sim 11$ (see Fig. 8a–d) and to $\varepsilon_\nu \sim 210$ (see Fig. 9a–d) were analyzed by means of EBSD in order to assess the final grain size and possible characteristic features after annealing by HT-XRD. From the grain size plots, displayed in Figs. 8,e and 9e, it can be observed that the composites resulted in a finer microstructure than the respective Ni samples. This effect is more pronounced in the composites with higher initial equivalent strain, which presented an annealed UFG microstructure. In order to further study the microstructural stability of the composites, isothermal annealings were performed.

Isothermal annealing. *Zener pinning model.* Second-phase particles decrease the maximum grain size obtained after annealing by kinetic stabilization of the grain boundaries[31] (a phenomenon known as "Zener drag"). The limiting grain size can be written as $GS_{lim} = \frac{k'}{f^m}$, where k' and m are constants and f is the volume fraction of pinning particles (i.e. CNT agglomerates). Furthermore, k' comprises a constant β and the particle size D. For large volume fractions (f ~ 0.02) and for particles located mainly at the grain boundaries m = 1/3[32,33]. The composites in the present study were fabricated by powder metallurgy (solid state processing) and consequently, the CNT are expected to be present only along the grain boundaries. The Ni samples and the composites were annealed during 12 h at 500 °C, which corresponds to a homologous temperature of 0.45T_m, and the final grain size was measured

by means of EBSD at 3 mm from the samples' centers along the radial direction. Figure 10 shows the composites' final grain sizes (symbols) together with the respective Zener models $GS_{lim} = \frac{k'}{V_{CNT}^{1/3}}$, where V_{CNT} is the CNT volume fraction used for the fabrication of the composites. Results for Ni samples can be found in Table S1 from the supplementary material. It should be mentioned that the CNT agglomerates are expected to be more uniformly dispersed with higher equivalent strains and their final agglomerate sizes lie within the same range[21]. Within experimental uncertainty, the composites showed a similar behavior with final grain sizes lying rather within the UFG range. Moreover, it can be observed that the curves adjust well to m = 1/3. Nevertheless, there are certain differences in grain size among samples deformed with different equivalent strains, which can be related to several phenomena taking place during annealing. For instance, it is well known that finer microstructures will recrystallize faster but are expected to result in smaller grain sizes. Also, the recrystallization process in SPD materials can be inhomogeneous due to heterogeneity in the as deformed structure being transferred into the annealed samples, for example, because HAGB have higher mobility than LAGB and regions with higher amounts of HAGB recrystallize first. Furthermore, grains located in regions with higher stored energy grow to a larger size. Additionally, the final grain size is also affected by the way how the agglomerates are dispersed and a non-homogeneous distribution could lead to abnormal grain growth with some grains being pinned and not others.

Conclusions

Ni/CNT composites processed by HPT exhibited an improved thermal stability upon annealing for 12 h at a homologous temperature of $0.45T_m$ with final grain sizes dependent on the CNT volume fraction following an $f^{-1/3}$ relationship consistent with theoretical Zener drag models. Furthermore, the microstructural changes during heating and therefore, the final microstructure, were affected by the initial microstructural state of the samples and the CNT after SPD. Thereby, the formation of nickel carbide was detected by DSC and HT-XRD and the evolution of the microstructure was analyzed by means of X-ray line profile analysis. Even though irreversible damage is introduced to the CNT, these are able to pin the grain boundaries during grain growth, and although recovery of defects and grain growth took place during heating, the composites presented a final ultrafine microstructure. It can be thus concluded that the use of CNT in NC and UFG materials processed by SPD successfully stabilizes the microstructure after heating. The present work provides relevant understanding on the assessment of the thermal stability in CNT-MMC and can be useful for further research in the area of SPD of engineering materials.

Data availability

The datasets used in the present study may be made available on reasonable request.

References

1. Valiev, R. Z. & Langdon, T. G. Report of International NanoSPD Steering Committee and statistics on recent NanoSPD activities. *IOP Conf. Ser. Mater. Sci. Eng.* **63** (2014).
2. Valiev, R. Z., Islamgaliev, R. K. & Alexandrov, I. V. Bulk nanostructured materials from severe plastic deformation. *Prog. Mater. Sci.* **45**, 103–189 (2000).
3. Valiev, R. Z. Structure and mechanical properties of ultrafine-grained metals. *Mater. Sci. Eng.* **234–236**, 59–66 (1997).
4. Ditenberg, I. A. *et al.* Nonequilibrium structural states in nickel after large plastic deformation. *Lett. Mater.* **4**, 100–103 (2014).
5. Setman, D., Schafler, E., Korznikova, E. & Zehetbauer, M. J. The presence and nature of vacancy type defects in nanometals detained by severe plastic deformation. *Mater. Sci. Eng. A* **493**, 116–122 (2008).
6. Schafler, E. & Pippan, R. Effect of thermal treatment on microstructure in high pressure torsion (HPT) deformed nickel. *Mater. Sci. Eng. A* **387–389**, 799–804 (2004).
7. Estrin, Y. & Vinogradov, A. Extreme grain refinement by severe plastic deformation: A wealth of challenging science. *Acta Mater.* **61**, 782–817 (2013).
8. Gao, N., Starink, M. J. & Langdon, T. G. Using differential scanning calorimetry as an analytical tool for ultrafine grained metals processed by severe plastic deformation. *Mater. Sci. Technol.* **25**, 687–698 (2009).
9. Yu, T., Hansen, N. & Huang, X. Recovery mechanisms in nanostructured aluminium. *Philos. Mag.* **92**, 4056–4074 (2012).
10. Liu, Y., Liu, L., Shen, B. & Hu, W. A study of thermal stability in electrodeposited nanocrystalline Fe-Ni invar alloy. *Mater. Sci. Eng. A* **528**, 5701–5705 (2011).
11. Liang, N. *et al.* Influence of microstructure on thermal stability of ultrafine-grained Cu processed by equal channel angular pressing. *J. Mater. Sci.* **53**, 13173–13185 (2018).
12. Sharma, G., Varshney, J., Bidaye, A. C. & Chakravartty, J. K. Grain growth characteristics and its effect on deformation behavior in nanocrystalline Ni. *Mater. Sci. Eng. A* **539**, 324–329 (2012).
13. Niu, T., Chen, W., Cheng, H. & Wang, L. Grain growth and thermal stability of nanocrystalline Ni–TiO2 composites. *Trans. Nonferrous Met. Soc. China (English Ed.* **27**, 2300–2309 (2017).
14. Stráská, J. *et al.* Thermal Stability of Ultra-Fine Grained Microstructure in Mg and Ti Alloys. In *Severe Plastic Deformation Techniques* 145–173 (2017).
15. Rane, G. K., Welzel, U. & Mittemeijer, E. J. Grain growth studies on nanocrystalline Ni powder. *Acta Mater.* **60**, 7011–7023 (2012).
16. Jung, S. H., Yoon, D. Y. & Kang, S. J. L. Mechanism of abnormal grain growth in ultrafine-grained nickel. *Acta Mater.* **61**, 5685–5693 (2013).
17. Bachmaier, A., Hohenwarter, A. & Pippan, R. New procedure to generate stable nanocrystallites by severe plastic deformation. *Scr. Mater.* **61**, 1016–1019 (2009).
18. Bachmaier, A. & Motz, C. On the remarkable thermal stability of nanocrystalline cobalt via alloying. *Mater. Sci. Eng. A* **624**, 41–51 (2015).
19. Weissmüller, J., Krauss, W., Haubold, T., Birringer, R. & Gleiter, H. Atomic Structure and Thermal Stability of Nanostructured Y-Fe Alloys. *Nanostructured Mater.* **1**, 439–447 (1992).
20. Aristizabal, K., Katzensteiner, A., Bachmaier, A., Mücklich, F. & Suarez, S. Study of the structural defects on carbon nanotubes in metal matrix composites processed by severe plastic deformation. *Carbon N. Y.* **125** (2017).

21. Aristizabal, K., Katzensteiner, A., Bachmaier, A., Mücklich, F. & Suárez, S. On the reinforcement homogenization in CNT/metal matrix composites during severe plastic deformation. *Mater. Charact.* **136** (2018).
22. Aristizabal, K., Katzensteiner, A., Leoni, M., Mücklich, F. & Suárez, S. Evolution of the lattice defects and crystalline domain size in carbon nanotube metal matrix composites processed by severe plastic deformation. *Mater. Charact.* https://doi.org/10.1016/J.MATCHAR.2019.06.019 (2019).
23. Reinert, L., Zeiger, M., Suárez, S., Presser, V. & Mücklich, F. Dispersion analysis of carbon nanotubes, carbon onions, and nanodiamonds for their application as reinforcement phase in nickel metal matrix composites. *RSC Adv.* **5**, 95149–95159 (2015).
24. Stüwe, H. P. Equivalent strains in severe plastic deformation. *Adv. Eng. Mater.* **5**, 291–295 (2003).
25. Leng, Y., Xie, L., Liao, F., Zheng, J. & Li, X. Kinetic and thermodynamics studies on the decompositions of Ni3C in different atmospheres. *Thermochim. Acta* **473**, 14–18 (2008).
26. Chiang, R. T., Chiang, R. K. & Shieu, F. S. Emergence of interstitial-atom-free HCP nickel phase during the thermal decomposition of Ni3C nanoparticles. *RSC Adv.* **4**, 19488–19494 (2014).
27. Portnoi, V. K., Leonov, A. V., Mudretsova, S. N. & Fedotov, S. A. Formation of nickel carbide in the course of deformation treatment of Ni-C mixtures. *Phys. Met. Metallogr.* **109**, 153–161 (2010).
28. Abrasonis, G. *et al.* Growth regimes and metal enhanced 6-fold ring clustering of carbon in carbon-nickel composite thin films. *Carbon N. Y.* **45**, 2995–3006 (2007).
29. Scardi, P. & Leoni, M. Whole powder pattern modelling. *Acta Crystallogr. Sect. A Found. Crystallogr.* **58**, 190–200 (2002).
30. De Keijser, T., Langford, J. I., Mittemeijer, E. J. & Vogels, A. B. P. Use of the Voigt function in a single-line method for the analysis of X-ray diffraction line broadening. *J. Appl. Crystallogr.* **15**, 308–314 (2002).
31. Smith, C. S. Grains, phases, and interfaces: An interpretation of microstructure. *Trans. Metall. Soc. AIME* **175**, 15–51 (1948).
32. Manohar, P. A., Ferry, M. & Chandra, T. Five Decades of the Zener Equation. *ISIJ Int.* **38**, 913–924 (1998).
33. Humphry-Baker, S. A. & Schuh, C. A. Suppression of grain growth in nanocrystalline Bi2Te3 through oxide particle dispersions. *J. Appl. Phys.* **116** (2014).

Acknowledgements

Author contributions

S. Suarez and A. Bachmaier initiated the concepts and designed the experiments. S. Suarez, A. Bachmaier and F. Mücklich supervised the work. K. Aristizabal and A. Katzensteiner manufacture and processed the samples. K. Aristizabal carried out the experiments. K. Aristizabal and S. Suarez analyzed the data, conceptualized the experimental results and performed calculations. K. Aristizabal wrote the manuscript. All authors reviewed and commented on the manuscript.

Competing interests

The authors declare no competing interests.

Additional information

Supplementary information is available for this paper at https://doi.org/10.1038/s41598-020-57946-3.

Correspondence and requests for materials should be addressed to K.A. or S.S.

Reprints and permissions information is available at www.nature.com/reprints.

Publisher's note Springer Nature remains neutral with regard to jurisdictional claims in published maps and institutional affiliations.

Microstructural evolution during heating of CNT/Metal Matrix Composites processed by Severe Plastic Deformation

Katherine Aristizabal[1, *], Andreas Katzensteiner[2], Andrea Bachmaier[2], Frank Mücklich[1] and Sebastian Suárez[1,*].

[1]Chair of Functional Materials, Department of Materials Science, Saarland University. D-66123, Saarbrücken, Germany.

[2]Erich Schmid Institute of Materials Science, Austrian Academy of Sciences, Jahnstrasse 12, A-8700 Leoben, Austria.

Supplementary information

X-ray single line profile analysis.

Different methods for the determination of the structural parameters by means of X-ray diffraction rely on the analysis of as many reflections available for the determination of the integral breadth (e.g. Williamson-Hall and the respective modified versions), or rely on at least two harmonic reflections (e.g. Warren-Averbach and the respective modified versions). Nevertheless, when only one Bragg peak, for example, is available from experimental results, single line analysis provides an appropriate approach, which is based on experimental observations that crystallite size causes Cauchy-type broadening (i.e. Lorentzian) while strain broadens the peak following a Gauss profile. Thereby, the Cauchy and Gauss fractions of a Bragg reflection represent the size and the strain contributions, respectively[1,2]. By using a Pseudo-Voigt type line profile convolution of the available Bragg peaks, the Cauchy and the Gauss parts of the instrument and the sample are obtained

and after extracting the instrumental contribution, the integral breadths (B) of the sample's profile broadenings are used to calculate the average crystallite size <D>$_V$ and the weighted average strain $\bar{\varepsilon}$ in [%] (mean lattice distortion), according to:

$$< D >_V = K\lambda/B_{Size}cos\theta$$

$$\bar{\varepsilon} = B_{Strain}/4tan\theta$$

Where λ is the X-ray wavelength; K is a shape factor, which changes depending of the assumed shape. Thus, for spheres it is 1.07 and for cubes it ranges between 1 and 1.16. In the present study, a shape factor of 1 was used. Furthermore, the crystalline domain size and the microstrain reported correspond to peak-area weighted averages of the Ni_{111} and Ni_{200} Bragg peaks.

Table S 1

Grain sizes for Ni samples measured by EBSD after 12h annealing at 500°C.

Equivalent strain	Mean grain size in µm
16	8.44 ± 4.68
60	6.69 ± 4.14
150	5.78 ± 3.20
350	5.01 ± 2.48

References

1. De Keijser, T., Langford, J. I., Mittemeijer, E. J. & Vogels, A. B. P. Use of the Voigt function in a single-line method for the analysis of X-ray diffraction line broadening. *J. Appl. Crystallogr.* **15**, 308–314 (2002).

2. De Keijser, T., Mittemeijer, E. J. & Rozendaal, H. C. F. The determination of crystallite-size and lattice-strain parameters in conjunction with the profile-refinement method for the determination of crystal structures. *J. Appl. Crystallogr.* **16**, 309–316 (1983).

VI. Friction and tribo-chemical behavior of SPD-processed CNT-reinforced composites

Katherine Aristizabal[1], Alexandra Tayrac[1], Andreas Katzensteiner[2], Andrea Bachmaier[2], Sebastián Suárez[1]

1 Department of Material Science and Engineering, Saarland University,
66123 Saarbrücken, Germany
2 Erich Schmid Institute, Austrian Academy of Sciences, Jahnstrasse 12, 8700 Leoben, Austria

Own Contribution: Project management, sample manufacturing and processing, experimental execution, data analysis, conceptualization of experimental results and calculations, manuscript writing.

Abstract:

Nickel (Ni) and carbon nanotube (CNT)-reinforced Ni-matrix composites were manufactured by solid state processing and severely deformed by high-pressure torsion (HPT). Micro-tribological testing was performed by reciprocating sliding and the frictional behavior was investigated. Tribochemical and microstructural changes were investigated using energy dispersive x-ray spectroscopy (EDS), scanning electron microscopy (SEM) and focused ion beam (FIB). The CNT lubricity was hindered due to the continuous formation of a stable oxide layer

promoted by a large grain boundary area and by irreversible damage introduced to reinforcement the during HPT, controlling the frictional behavior of the studied samples. The presence of CNT reduced to some extent the tribo-oxidation activity on the contact zone and reduced the wear by significant hardening and stabilization of the micro-structure.

lubricants   **MDPI**

Article

Friction and Tribo-Chemical Behavior of S PD-Processed CNT-Reinforced Composites

Katherine Aristizabal [1,*], Alexandra Tayrac [1], Andreas Katzensteiner [2], Andrea Bachmaier [2] and Sebastian Suarez [1,*]

[1] Chair of Functional Materials, Saarland University, Campus D3.3, 66123 Saarbrücken, Germany
[2] Erich Schmid Institute of Materials Science, Austrian Academy of Sciences, Jahnstrasse 12, 8700 Leoben, Austria
* Correspondence: katherine.aristizabal@uni-saarland.de (K.A.); s.suarez@mx.uni-saarland.de (S.S.)

Abstract: Nickel (Ni) and carbon nanotube (CNT)-reinforced Ni-matrix composites were manufactured by solid state processing and severely deformed by high-pressure torsion (HPT). Micro-tribological testing was performed by reciprocating sliding and the frictional behavior was investigated. Tribo-chemical and microstructural changes were investigated using energy dispersive X-ray spectroscopy (EDS), scanning electron microscopy (SEM) and focused ion beam (FIB). The CNT lubricity was hindered due to the continuous formation of a stable oxide layer promoted by a large grain boundary area and by irreversible damage introduced to the reinforcement during HPT, which controlled the frictional behavior of the studied samples. The presence of CNT reduced, to some extent, the tribo-oxidation activity on the contact zone and reduced the wear by significant hardening and stabilization of the microstructure.

Keywords: carbon nanotubes; metal matrix composites; severe plastic deformation; reciprocating sliding.

1. Introduction

In a tribological system, where two bodies are moving relative to each other with a certain speed under the application of a normal force (F_N) and along a certain distance with certain environmental conditions (e.g., temperature and humidity), there are other aspects, such as the surface finish [1–4] and the microstructure [5–7], that affect the wear, the friction and even the tribo-oxidation on the contact zone. Furthermore, it has been shown that intermittent tribological loading induces plastic deformation in a layer beneath the wear track in the tribologically transformed zone (TTZ) [8], which could result in grain refinement (in initially coarse-grained materials) [4,9] or grain coarsening (in initially nanocrystalline materials) [4,6,7,10,11].

Tribological testing on ultrafine-grained (UFG) and nanocrystalline (NC) materials obtained by severe plastic deformation (SPD) can lead to interesting results, due to the different phenomena that can occur. For instance, despite the increase in hardness due to a finer microstructure that can lead to a decrease in the coefficient of friction (COF) and a decrease in the wear rate, corrosion and oxide formation can be promoted by the high amount of grain boundaries affecting both friction and wear. Accordingly, even though there are studies showing improved wear resistance in materials processed by equal-channel angular pressing (ECAP), high pressure torsion (HPT) and accumulative roll-bonding (ARB), there are studies showing reduced wear resistance and others showing that the processing routes had little influence on the wear behavior [12]. On the one hand, the factors improving the wear resistance in SPD-processed materials are the smaller grain sizes and the higher hardness and strength. On the other hand, factors such as the decreased ductility, the low strain hardening capability, the higher oxidation rate, the non-equilibrium and unstable grain boundaries,

the strain-induced grain coalescence and the strain incompatibility between surface and bulk materials are responsible for the reduction in wear resistance. For further information refer to [12] and the references therein.

Strategies have been proposed to improve the wear resistance in SPD-processed materials, such as heat treatments after processing, the use of hard coatings such as TiO_2, TiN and diamond-like carbon, and the introduction of ceramic reinforcements such as SiC [13] and Al_2O_3 [14]. Furthermore, carbon nanotubes (CNT) have proved to be suitable for their use as solid lubricants and have been used in metal matrix composites (MMC) [15–17]. Providing there is a weak bond between the CNT and the metal and the CNT are uniformly distributed, CNT will continuously move to the tribological contact to roll and slide and even form a lubricating carbon film by degrading the CNT, thus improving both the wear and the COF (see [18] and the references therein). Furthermore, CNT have also been used for the production of lubricating coatings. Reinert et al. [19] studied and compared the tribo-mechanisms of CNT in CNT/Ni matrix composites and CNT-coated bulk Ni; they found that the reduction in COF in the coating lasts as long as there are CNT at the contact zone. After removal, the COF increased, whereas in the composite the COF reduction is pronounced up to 20,000 cycles due to a continuous supply of CNT to the contact zone. Nevertheless, CNT coatings produced on laser-patterned surfaces showed a long-lasting solid lubrication, due to CNT entrapping inside the laser textures serving as lubricant reservoirs [20].

Several studies have been performed regarding the microstructural changes during HPT of CNT/Ni [21–25]. In this work, micro-tribological testing was performed on CNT/Ni matrix composites processed by SPD by means of HPT, a technique in which a cylindrical sample is pressed under high hydrostatic pressure (in this case 4 GPa) while the upper anvil is kept static and the lower anvil is rotated to obtain the desired equivalent strain. The equivalent strain (ε_{vM}) increases with the radius according to: $\varepsilon_{vM} = 2\pi \cdot T \cdot r/(t \cdot \sqrt{3})$, where T is the number of turns, t is the sample thickness and r is the distance from the center of the sample [26]. Furthermore, the wear tracks were analyzed by means of scanning electron microscopy (SEM) and energy dispersive X-ray spectroscopy (EDS) in order to study the tribo-chemistry. Finally, the subsurface was studied by means of focused ion beam (FIB) in order to assess possible microstructural changes under the wear scar.

2. Materials and Methods

For the fabrication of the samples, multi-walled CNT (chemical vapor deposition –CVD- grown, Graphene Supermarket, Ronkonkoma, NY, USA, density 1.84 g/cm³) were mixed in different concentrations (0.5, 1 and 2 wt.%) with dendritic Ni powder (Alfa Aesar, Kandel, Germany, mesh −325) via colloidal mixing [27]. The powder mixtures were then cold pressed (990 MPa) in cylindrical pellets and sintered under vacuum (2 × 10⁻⁶ mbar, 900 °C for 3 h). The cold pressed sintered (CPS) composites and Ni samples of 8 mm diameter and 1 mm thickness were plastically deformed by HPT at room temperature using 1, 10 and 20 T.

The samples were then polished until mirror finish, R_q = (3.9 ± 0.9) µm (with OP-S colloidal silica, Struers, Willich, Germany), and tested using a ball-on-disk tribometer under a linear reciprocating motion using an Al_2O_3 ball (3 mm diameter) as a counter body. Table 1 shows the parameters used for the tribological tests.

Table 1. Parameters of the tribological experiments.

Parameter	Unit	Value
Temperature	°C	25
Relative humidity	%	3.8
Load F_N	N	0.1
Sliding velocity v	mm/s	1
Stroke length	Mm	0.6

The samples were tested three times at 3 mm from the center (see Figure 1) and the results were averaged. Vickers micro hardness ($HV_{0.3}$) measurements were performed at 3 mm from the samples'

centers using an indenter Struers DuraScan 50/70/80 and 15 s of dwell time. Table 2 shows the corresponding average hardness results for the studied samples. Moreover, electron micrographs, FIB cross-sections and EDS analyses were performed on a Helios NanoLab™ 600 dual beam field emission microscope (FEI Company).
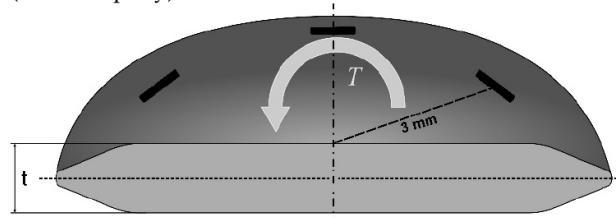

Figure 1. Schematic showing test positions. *T* indicates the direction of torsional rotation and *t* is the sample thickness.

Table 2. Hardness measured at 3 mm from the samples' centers with increasing equivalent strains.

Sample	Tested Equivalent Strain	Hardness/GPa
Ni_1T	14.51 ± 0.75	4.56 ± 0.09
Ni_10T	146.47 ± 4.54	4.78 ± 0.04
Ni_20T	310.67 ± 8.68	4.85 ± 0.10
0.5_1T	15.1 ± 0.65	3.92 ± 0.02
0.5_10T	134.94 ± 8.18	5.56 ± 0.05
0.5_20T	282.44 ± 25.89	6.44 ± 0.14
1_1T	15.76 ± 0.73	3.63 ± 0.02
1_10T	135.71 ± 3.48	6.33 ± 0.03
1_20T	281.86 ± 0	7.58 ± 0.41
2_1T	14.73 ± 1.09	3.58 ± 0.08
2_10T	149.57 ± 2.59	7.62 ± 0.03
2_20T	298.74 ± 14.23	8.01 ± 0.06

3. Results and Discussion

3.1. Friction Analysis

Figure 2 shows the evolution of the COF for the tested samples and the corresponding run-in behavior. Considering the dispersion of results, no significant differences in COF for different concentrations of CNT and deformation states are noticeable (Figure 2a–c). In all cases, the steady state COF value oscillates around 0.3. The same effect has already been reported for SPD-processed Ti [28] where, despite testing two different initial microstructures (ultrafine and coarse-grained), the steady state COF was the same for a wide range of experimental loads.

The main differences are observed during the run-in stage (Figure 2d–f). In all cases, the pure Ni samples show a high initial COF value (between 0.55 and 0.6) that stabilizes after 20–30 cycles. The development of the COF curves for these samples indicates a significant plastic deformation at the beginning, subsequently achieving the steady state after reaching conformality. The CNT-containing sample shows a delayed stabilization, with indications of lower plastic deformation showing a steady state behavior first after 30–40 sliding cycles. The shape of these run-in curves is common in non-lubricated metals, where the COF increases temporarily due to the initial surface roughness and decreases after achieving surface conformality and smoothing [29].
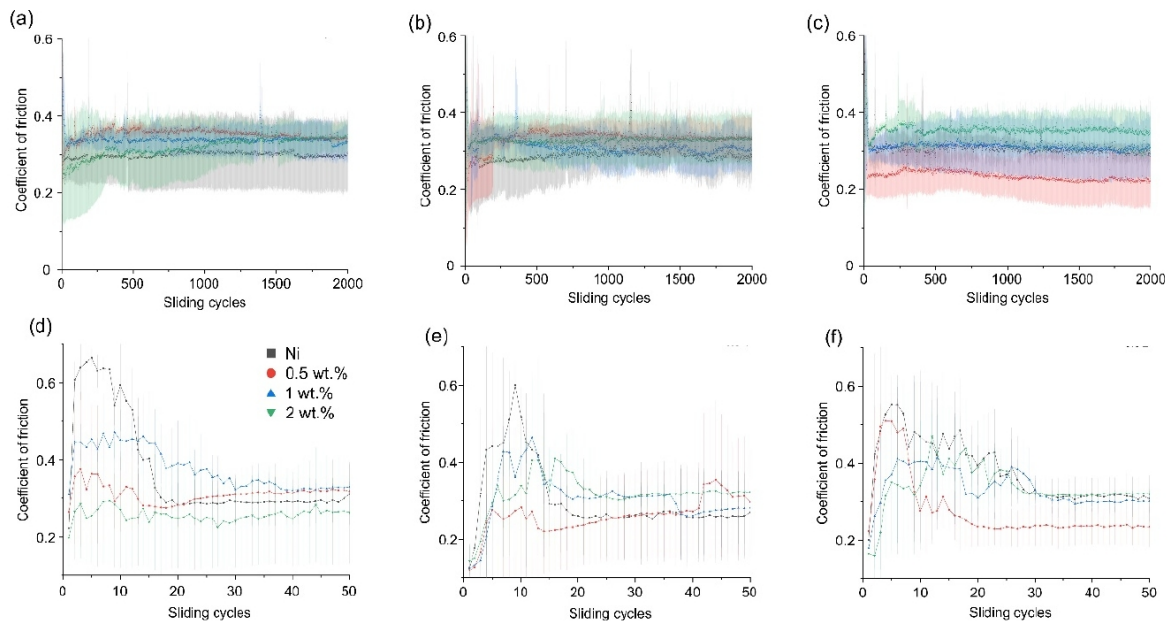
Figure 2. Evolution of the coefficient of friction (COF) versus the sliding cycles for: (**a**) 1 turn; (**b**) 10 turns; (**c**) 20 turns. Run-in behavior of the COF versus the sliding cycles for: (**d**) 1 turn; (**e**) 10 turns; (**f**) 20 turns.

The drop-in COF also takes place due to hardening of the near-surface regions due to shear stresses [29,30]. Furthermore, this slight increase in the COF and subsequent reduction can be attributed to the formation and release of debris (third body particles) into the contact, resulting from the continuous formation and breaking of a thin oxide layer reaching a dynamic balance in the steady state.

3.2. Wear Track Morphology and Tribo-Chemical Mechanisms

Further analysis of the results focuses on the samples subjected to the highest deformation (20 T). Figure 3 displays electron micrographs of the wear tracks. A first qualitative assessment suggests that the scar width is smaller in the composites. This can be attributed to a significantly harder surface in the composites, resulting in a smaller penetration depth of the counter body, which can be confirmed from the wear track profiles shown in Figure 4. Additionally, the characterization of the contact surface of the balls, shown in Figure 5, confirms that the wear activity of the counterpart was mild.

The pure metal sample shows regions of severe wear, indicated by the presence of laminated debris with partial detachment from the surface. This is extensively found within the affected zone and might be related to local thermal effects [31]. Furthermore, the tribologically affected surface shows significant continuity throughout the wear scar. The composite reinforced with 2 wt.% CNT presents evidence of mild wear associated with the development of a discontinuous tribolayer with almost no spallation and some scratch marks, which is typical of an abrasive mechanism [32]. The remaining sample (0.5 wt.% CNT) presents mild wear as well, but with evidence of both previously described cases. Certain regions show signs of galling, typical of a mild adhesive wear mechanism [32], whereas spallation and delamination of the tribolayer is noticed as well.
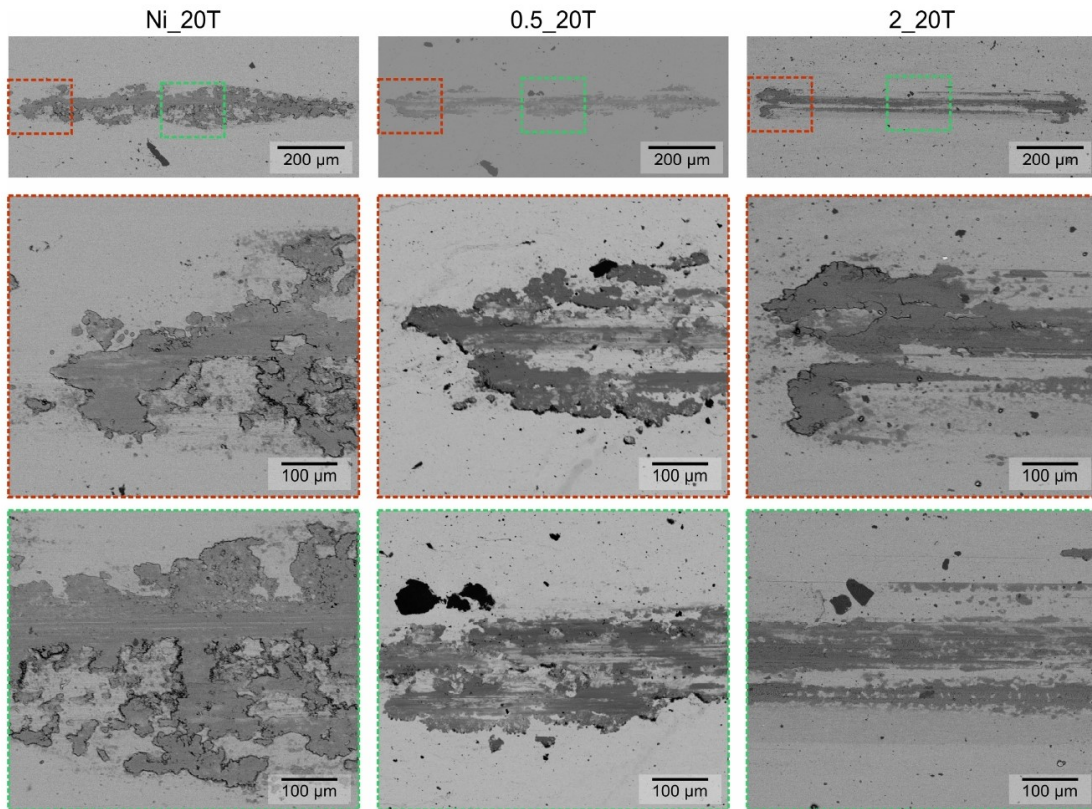
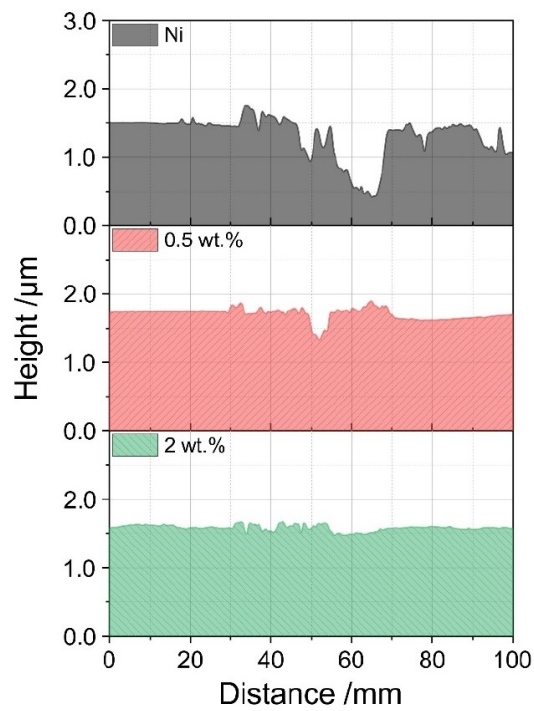**Figure 3.** Electron micrographs on the wear scars.

Figure 4. Wear track profiles for the samples deformed at 20 T obtained from the topographical characterization by means of confocal laser scanning microscopy.
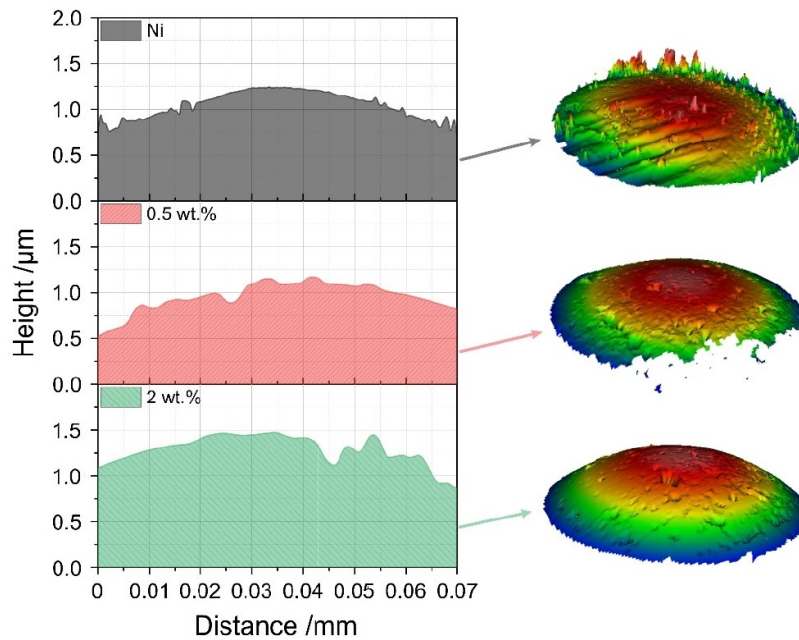
Figure 5. Topographical profile and 3D map of the worn surface of the test counterparts acquired by white light interferometry.

Further morphological characteristics can be observed in detail in Figure 6, obtained with higher magnification from the edge of the central region of the tracks (in the sliding direction, where the maximum sliding velocity is obtained). These regions present indications of ploughing (for the pure metal and the 0.5 wt.% sample) and some wedge formation, which are characteristic of abrasive wear.
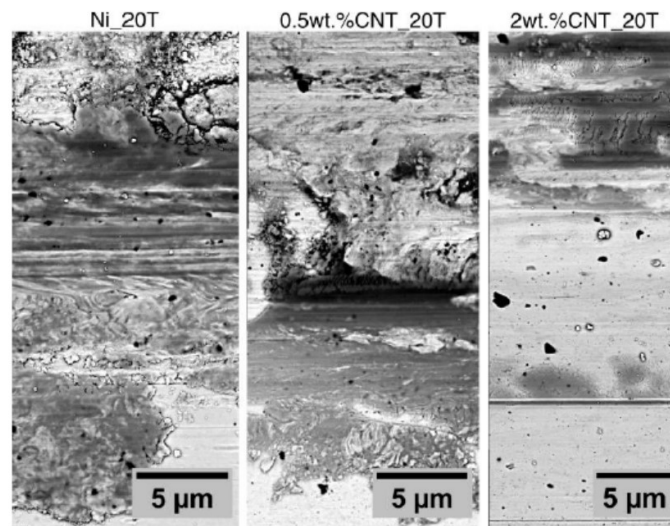

Figure 6. Detailed view of the wear scar edges at the center of the sliding track.

Nevertheless, adhesion and delamination of the oxide layer formed during sliding also occurred along with some intermixing with the metallic matrix. Such intermixing is less pronounced in the harder sample, which has grooves in the sliding direction, likely as a consequence of a reduced ductility [25] complicating the mechanical mixing process.

These observations were further expanded by performing a chemical analysis of the tribolayer to acquire oxygen distribution maps of the wear scar (Figure 7). In all cases, wear debris ejected from

the tribological contact is observed (seen as small oxide particles outside the wear scar). The oxide layer appeared to be more pronounced in the case of pure Ni, which suggests that oxidation is reduced in the CNT-containing samples, at least from the observation of the total affected area. This observation is in agreement with the previously identified wear mechanisms [33]. The CNT brought into contact act as oxygen diffusion barriers, slowing the oxidation of the substrate. This is related to carbon being more prone to reactions with oxygen and its oxide being more stable than that of Ni.
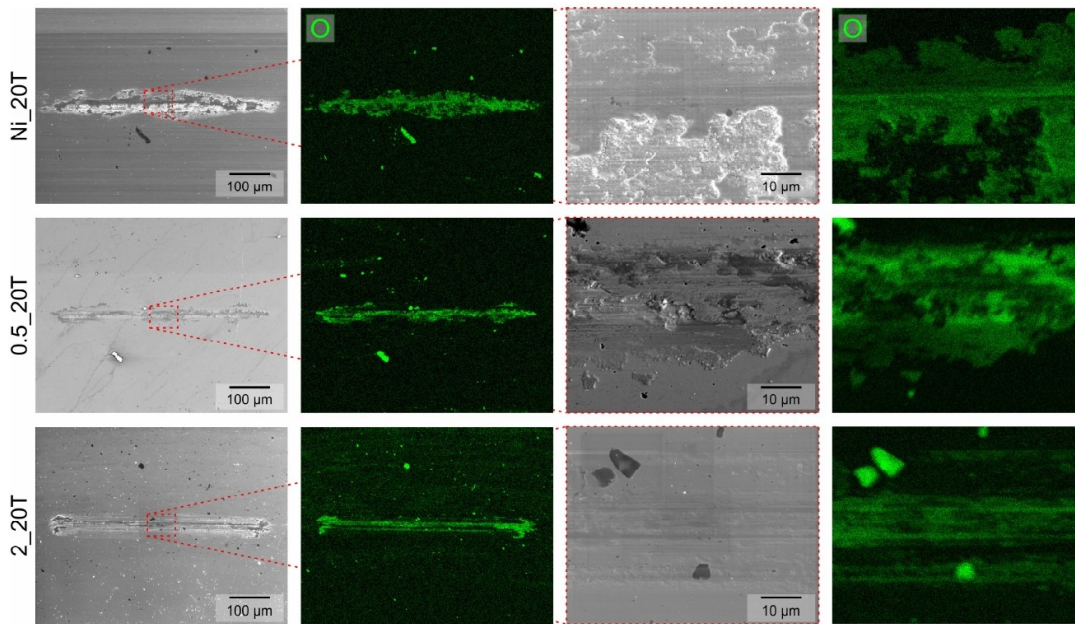

Figure 7. Oxygen distribution maps obtained by energy dispersive X-ray spectroscopy (EDS) from the wear tracks.

The lubrication mechanism of CNT in coarse-grained CNT/Ni matrix composites consists of the CNT being continuously provided to the contact zone, where a mixture between a rolling motion of the multiwall CNT on the surface and particle degradation occurs, including the formation of nanocrystalline graphitic layers [4]. For systems tested under the same experimental conditions, the lubricity of CNT is evidenced by a steady state COF of approximately 0.1, which is considerably below the COF obtained for the HPT-deformed systems. From the discussed results, the ultrafine-grained microstructures increase the oxidation activity of the surface due to a large grain boundary area. Moreover, even though the CNT distribution is significantly improved and the size of the agglomerates is significantly smaller in the deformed samples in comparison to the non-deformed samples [22], irreversible damage to the CNT is introduced by HPT [34] which renders them more susceptible to complete degradation and/or oxygen bonding. According to this, the CNT's ability to act as solid lubricants in the studied composites is strongly hindered. From these results, it can be concluded that in CNT/Ni matrix composites processed by HPT, the microstructure characteristics have a more significant effect on the steady state COF during sliding contact than the presence of CNT, which only slightly decrease the oxidation of the contact zone.

3.3. Microstructure under the Wear Scar

The analysis of the sub-superficial microstructural state was carried out on the same sample set by performing cross-sections in the middle of the wear scar (Figure 8). No significant microstructural gradients beneath the surface are observed in any case, as opposed to what is expected when analyzing initially coarse-grained metals under dry sliding. This can be traced back to the fact that, for the TTZ to be developed, plastic deformation must occur beneath the worn surface due to the application of cyclic shear stresses. In the case of Ni (Figure 8a,b), the deformed sample (20 T of HPT)

already achieved the microstructural steady state, as previously discussed [34]. Therefore, it is expected that no further microstructural changes or strain hardening would take place during strain accumulation.
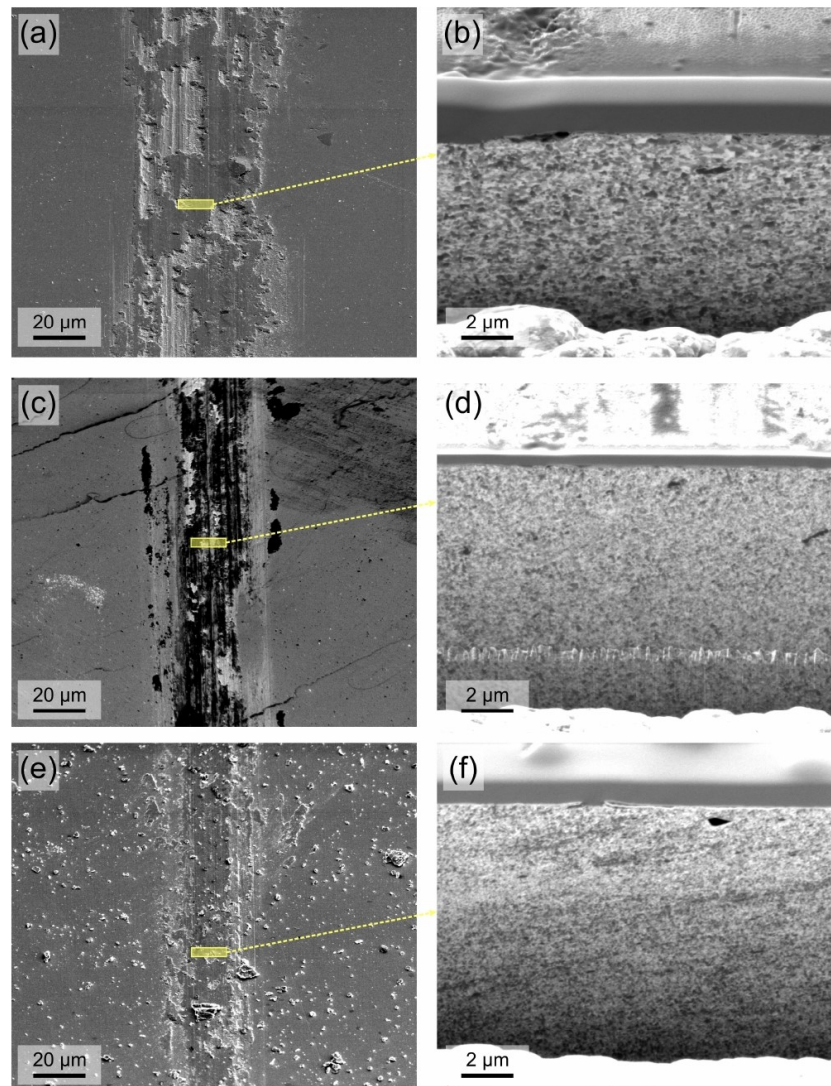

Figure 8. Cross-sections in the center of the wear scars in: (**a**,**b**) nickel; (**c**,**d**) 0.5 wt.% carbon nanotubes (CNT); (**e**,**f**) 2 wt.% CNT processed by high-pressure torsion (HPT) with 20 T.

In the case of the composites, even though the composites do not resemble the steady state hardness (as revealed in Table 2 by the continuously increasing hardness with higher accumulated equivalent strains), a significant reduction in grain size and a high density of defects [24] might be the defining factors. The maximum CNT distribution homogeneity was indeed achieved [22], which vouches for the proper microstructural stabilization, rendering the composites significantly harder and stable against possible microstructural changes induced during the tribological experiment.

To summarize, friction behavior is dominated by the quick formation of a tribologically induced oxide layer, which hinders the lubricity of the CNT. Wear, on the other hand, is reduced in the composites (when compared to the pure metal), resulting from a harder surface. Additionally, the presence of CNT aids in the stabilization of the microstructure during sliding, hence limiting the metal–oxide intermixing.

4. Conclusions

In this paper, Ni and CNT/Ni composites with different CNT contents were processed by HPT with increasing equivalent strains. The resulting ultrafine-grained materials were tested by reciprocating sliding. The frictional, tribo-chemical and microstructural changes were investigated after 2000 sliding cycles. CNT structural defects, stemming from HPT processing and tribological contact, deterred their lubricity. The formation of a stable oxide layer also took place. As a result, the steady state COF stabilized around the same value ($\mu_{steady} \approx 0.3$) for all the tested samples. No significant microstructural changes beneath the wear track were observed as a result of very hard surfaces, especially in the composites in which wear was reduced in comparison to Ni.

Author Contributions: S.S. and A.B. initiated the concepts and designed the experiments. K.A. and A.K. manufactured and processed the samples. K.A. and A. T. carried out the experiments. K.A. and S.S. characterized the samples, analyzed the data and wrote the manuscript. All authors reviewed and commented on the manuscript.

Conflicts of Interest: The authors declare no conflict of interest. The funders had no role in the design of the study; in the collection, analyses, or interpretation of data; in the writing of the manuscript, or in the decision to publish the results.

References

1. Sedlaček, M.; Podgornik, B.; Vižintin, J. Influence of surface preparation on roughness parameters, friction and wear. *Wear* **2009**, *266*, 482–487.
2. Meine, K.; Schneider, T.; Spaltmann, D.; Santner, E. The influence of roughness on friction Part I: The influence of a single step. *Wear* **2002**, *253*, 725–732.
3. Meine, K.; Schneider, T.; Spaltmann, D.; Santner, E. The influence of roughness on friction: Part II. The influence of multiple steps. *Wear* **2002**, *253*, 733–738.
4. Reinert, L.; Schütz, S.; Suárez, S.; Mücklich, F. Influence of surface roughness on the lubrication effect of carbon nanoparticle-coated steel surfaces. *Tribol. Lett.* **2018**, *66*, 45.
5. Mishra, R.; Basu, B.; Balasubramaniam, R. Effect of grain size on the tribological behavior of nanocrystalline nickel. *Mater. Sci. Eng. A* **2004**, *373*, 370–373.
6. Argibay, N.; Chandross, M.; Cheng, S.; Michael, J.R. Linking microstructural evolution and macro-scale friction behavior in metals. *J. Mater. Sci.* **2017**, *52*, 2780–2799.
7. Grützmacher, P.G.; Rammacher, S.; Rathmann, D.; Motz, C.; Mücklich, F.; Suarez, S. Interplay between microstructural evolution and tribo-chemistry during dry sliding of metals. *Friction* **2019**, doi.org/10.1007/s40544-019-0259-5.
8. Hutchings, I. Tribology: Friction and wear of engineering materials, 2nd ed.; Elsevier: Oxford, UK, 2017.
9. Rigney, D.A.; Fu, X.Y.; Hammerberg, J.E.; Holian, B.L.; Falk, M.L. Examples of structural evolution during sliding and shear of ductile materials. *Scr. Mater.* **2003**, *49*, 977–983.
10. Prasad, S. V.; Battaile, C.C.; Kotula, P.G. Friction transitions in nanocrystalline nickel. *Scr. Mater.* **2011**, *64*, 729–732.
11. Wasekar, N.P.; Haridoss, P.; Seshadri, S.K.; Sundararajan, G. Sliding wear behavior of nanocrystalline nickel coatings: Influence of grain size. *Wear* **2012**, *296*, 536-546.
12. Gao, N.; Wang, C.T.; Wood, R.J.K.; Langdon, T.G. Tribological properties of ultrafine-grained materials processed by severe plastic deformation. *J. Mater. Sci.* **2012**, *47*, 4779–4797.
13. Darmiani, E.; Danaee, I.; Golozar, M.A.; Toroghinejad, M.R.; Ashrafi, A.; Ahmadi, A. Reciprocating wear resistance of Al-SiC nano-composite fabricated by accumulative roll bonding process. *Mater. Des.* **2013**, *50*, 497–502.
14. Edalati, K.; Ashida, M.; Horita, Z.; Matsui, T.; Kato, H. Wear resistance and tribological features of pure aluminum and Al-Al$_2$O$_3$ composites consolidated by high-pressure torsion. *Wear* **2014**, *310*, 83–89.

15. Rajkumar, K.; Aravindan, S. Tribological studies on microwave sintered copper-carbon nanotube composites. *Wear* **2011**, *270*, 613–621.
16. Bastwros, M.M.H.; Esawi, A.M.K.; Wifi, A. Friction and wear behavior of Al-CNT composites. *Wear* **2013**, *307*, 164–173.
17. Abdullahi, U.; Maleque, M.A.; Nirmal, U. Wear mechanisms map of CNT-Al nano-composite. *Procedia Eng.* **2013**, *68*, 736–742.
18. Dorri Moghadam, A.; Omrani, E.; Menezes, P.L.; Rohatgi, P.K. Mechanical and tribological properties of self-lubricating metal matrix nanocomposites reinforced by carbon nanotubes (CNTs) and graphene - A review. *Compos. Part B Eng.* **2015**, *77*, 402–420.
19. Reinert, L.; Suárez, S.; Rosenkranz, A. Tribo-Mechanisms of Carbon Nanotubes: Friction and Wear Behavior of CNT-Reinforced Nickel Matrix Composites and CNT-Coated Bulk Nickel. *Lubricants* **2016**, *4*, 11.
20. Reinert, L.; Lasserre, F.; Gachot, C.; Grützmacher, P.; Maclucas, T.; Souza, N.; Mücklich, F.; Suarez, S. Long-lasting solid lubrication by CNT-coated patterned surfaces. *Sci. Reports* **2017**, *7*, 42873.
21. Aristizabal, K.; Suárez, S.; Katzensteiner, A.; Bachmaier, A.; Mücklich, F. Evolution of the microstructure in carbon nanotube reinforced Nickel matrix composites processed by high-pressure torsion. In Proceedings of the IOP Conference Series: Materials Science and Engineering; Bristol, UK, 2017; Volume 258, No. 1, p. 012008.
22. Aristizabal, K.; Katzensteiner, A.; Bachmaier, A.; Mücklich, F.; Suárez, S. On the reinforcement homogenization in CNT/metal matrix composites during severe plastic deformation. *Mater. Charact.* **2018**, *136*, 375–381.
23. Katzensteiner, A.; Aristizabal, K.; Suarez, S.; Pippan, R.; Bachmaier, A. Temperature dependent structural evolution in nickel/carbon nanotube composites processed by high-pressure torsion. In Proceedings of the IOP Conference Series: Materials Science and Engineering; Bristol, UK, 2017; Volume 194, No. 1, p. 01201.
24. Aristizabal, K.; Katzensteiner, A.; Leoni, M.; Mücklich, F.; Suárez, S. Evolution of the lattice defects and crystalline domain size in carbon nanotube metal matrix composites processed by severe plastic deformation. *Mater. Charact.* **2019**, *154*, 344–352.
25. Katzensteiner, A.; Müller, T.; Kormout, K.; Aristizabal, K.; Suarez, S.; Pippan, R.; Bachmaier, A. Influence of Processing Parameters on the Mechanical Properties of HPT-Deformed Nickel/Carbon Nanotube Composites. *Adv. Eng. Mater.* **2019**, *21*, 1800422.
26. Stüwe, H.P. Equivalent strains in severe plastic deformation. *Adv. Eng. Mater.* **2003**, *5*, 291–295.
27. Reinert, L.; Zeiger, M.; Suárez, S.; Presser, V.; Mücklich, F. Dispersion analysis of carbon nanotubes, carbon onions, and nanodiamonds for their application as reinforcement phase in nickel metal matrix composites. *RSC Adv.* **2015**, *5*, 95149–95159.
28. La, P.; Ma, J.; Zhu, Y.T.; Yang, J.; Liu, W.; Xue, Q.; Valiev, R.Z. Dry-sliding tribological properties of ultrafine-grained Ti prepared by severe plastic deformation. *Acta Mater.* **2005**, *53*, 5167–5173.
29. Blau, P.J. On the nature of running-in. *Tribol. Int.* **2005**, *38*, 1007–1012.
30. Blau, P.J. Running-in: Art or engineering? *J. Mater. Eng.* **1991**, *13*, 47–53.
31. Wilson, S.; Alpas, A.T. Thermal effects on mild wear transitions in dry sliding of an aluminum. *Wear* **1999**, *225*, 440–449.
32. Stachowiak, G. *Wear - Materials, mechanisms and practice*, 1st ed.; John Wiley & Sons: Hoboken, NJ, USA, 2005.
33. Scharf, T.W.; Neira, A.; Hwang, J.Y.; Tiley, J.; Banerjee, R. Self-lubricating carbon nanotube reinforced nickel matrix composites. *J. Appl. Phys.* **2009**, *106*, 013508.
34. Aristizabal, K.; Katzensteiner, A.; Bachmaier, A.; Mücklich, F.; Suarez, S. Study of the structural defects on carbon nanotubes in metal matrix composites processed by severe plastic deformation. *Carbon* **2017**, *125*, 156–161.

5. Conclusions

The present dissertation investigated the SPD by HPT at room temperature of CNT-reinforced Ni-MMC fabricated by solid state processing. Special focus was set on the following aspects:

- The microstructural evolution of the composites during HPT.

- The effect of HPT on the structural features of CNT and their degradation.

- The optimization of the reinforcement distribution homogeneity.

- The effect of increasing the CNT content and the applied equivalent strain on the crystalline domain size and the dislocation density. Also, the strengthening mechanisms of the composites were estimated.

- The microstructural stability of the SPD composites during heating and after annealing, with particular attention on the limiting grain size by means of Zener pinning relationship.

- The friction and tribo-chemical behaviour of the SPD composites related to the microstructural stability during tribo-tests.

All studies were also performed on pure Ni samples, which served as reference material.

Different amounts of CNT (i.e. 0.5 wt. % (2.4 vol. %), 1 wt. % (4.7 vol. %), 2 wt. % (9 vol. %) and 3 wt. % (13 vol. %)) were mixed by means of *colloidal mixing* with dendritic Ni powder. The powder mixtures were *cold pressed*

(990 MPa) and sintered by *hot uniaxial pressing* (2×10^{-6} mbar) at 750 °C for 2.5 h with a 264 MPa axial pressure. The composites with a diameter of 8 mm and approximately 1 mm of thickness were processed by HPT at room temperature using 1, 4, 10 and 20 T using 4 GPa of pressure. The respective equivalent strains measured at 3 mm from the samples' centers were ~ 18, ~ 70, ~ 190 and ~ 370. It should be noted that samples with 3 wt. % CNT harden prematurely (<4 T) during HPT at room temperature, which, together with the lubricity effect of the CNT, caused slippage of the anvils and made it impossible to further process them.

The structural damage undergone by the CNT during HPT was studied by means of *Raman spectroscopy*. The analysis of the <u>defect index I_D/I_G</u> was conventionally performed in the available literature, but based on the results, this was found to be insufficient for the analysis of CNT subjected to highly energetic processing such as HPT. According to this, a complementary analysis of the <u>shift of the G-band</u> was implemented. The apparent maximum damage, as studied by the <u>shift of the G-band</u>, was found to be reached at early stages of deformation by HPT, where the CNT follow an amorphization trajectory related to their capacity to withstand the applied strain during HPT, resulting in loss of order.

HPT proved to be highly effective not only for the microstructural refinement but also for the distribution homogenization of CNT in CNT-reinforced Ni-

MMC. CNT agglomerates were found to debond by relative sliding and to elongate in the shear direction at early stages of deformation. This is in contrast to ceramic particles that are hard and brittle and do not deform when debonding. Furthermore, a thorough characterization of the CNT spatial distribution was performed and an analytical model was proposed for the prediction of the minimum required strain ε_{min}^{hom} for a homogeneous distribution of the reinforcement, which only requires the initial grain size of the composites and the second phase volume fraction. It should be noted that the procedure applied in the present work and the respective analytical model can be also applied to other types of MMC. The calculated ε_{min}^{hom} for the studied CNT/MMC were 126.5, 96.31, 73.71 and 63.16, for the respective CNT volume fractions V_{CNT} used, i.e. 0.024, 0.047, 0.09 and 0.13. Accordingly, larger strains should be applied for lower V_{CNT} since inhomogeneity can rise from reinforcement-depleted regions.

The composites showed a significant decrease in grain size and increase in hardness with respect to pure Ni samples processed by HPT under the same experimental conditions. Nevertheless, the saturation in the microstructural refinement was not reached in any case in the composites, as demonstrated by a microstructural and hardness gradient along the radial direction. Results show that increasing the applied strain increased the dislocation density, where a higher amount of screw dislocations was measured by WPPM. This was attributed to the assumption that edge dislocations arrange, for instance in GB,

and contribute predominantly to the grain refinement and are therefore "seen" by XRD mostly as crystalline domains, whereas the screw dislocations are mainly located at the grain interiors. Moreover, CNT were found to promote a significant grain refinement, as a result of their interaction with dislocations and grain boundaries. It was concluded that the presence of CNT in CNT-MMC processed by HPT mainly assists the contribution of strengthening mechanisms due to work hardening and grain refinement. However, the contribution due to particle strengthening is only marginal.

A thorough study was performed on the microstructural evolution during heating and the thermal stability of the CNT-reinforced Ni-MMC processed by HPT. The formation and dissolution of the metastable Ni_3C phase between 200-350°C was evidenced by DSC and HT-XRD in composites, where sufficient carbon atoms were available as a consequence of irreversible damage suffered by the CNT during HPT. Nevertheless, it could be shown that the composites exhibit an improved thermal stability with respect to Ni samples processed under the same conditions. The composites presented a final grain size, which is dependent on the CNT volume fraction according to a $V_{CNT}^{-1/3}$ relationship and that lied within the UFG range.

Regarding the friction and tribo-chemical behavior of the SPD composites, micro-tribological testing was performed by reciprocating dry sliding. It was observed that the frictional behavior was controlled by a continuous formation

of a stable oxide layer, whose formation was promoted by a large grain boundary area. There, the CNT lubricity was hindered also due to irreversible damage induced during HPT. Nevertheless, in comparison to the tested Ni samples, the CNT reduce -to some extent- the tribo-oxidation activity in the contact zone as well as the wear in the composites. This was related to the microstructural stabilization and hardening of the composites, where no significant microstructural changes were observed under the wear track.

Further improvements in terms of the mechanical properties of the composites can be achieved by thermomechanical processing, by which a microstructural steady state with small grain sizes can be obtained, with both high strength and high ductility. In addition to that, the use of lower amounts of CNT can also lead to reduction of crack formation during processing, since less amount of agglomerates would be available for dislocation hindrance, avoiding a premature hardening during HPT.

HPT is a technique that, despite the technical difficulties involved in upscaling it to an industrial level, presents the possibility of manufacturing new material systems, either composites or alloys, with certain microstructures and physical properties, which are difficult to obtain by other processing methods.

Finally, it can be stated that CNT were successfully used for the stabilization of the microstructure in NC and UFG composites processed by HPT. Additionally,

their use can be extended to other metallic matrices, as long as a proper distribution of the CNT is provided and the CNT retain their structural features. Nevertheless, dissolution of CNT occurs when used as reinforcement in a metallic matrix with the tendency to form carbides (e.g. that contain Fe, Al, Cr or Ti), which would require the application of a protective coating on the CNT (nonreactive with C, e.g. with Ni). This protective coating would also improve the bonding between the CNT and the matrix. The application of such coatings has been barely studied in the literature.

Summarizing, all these findings relate to the understanding of the materials' structure/properties relationships and allow for a better comprehension of the mechanisms involved during SPD by HPT of CNT Ni-MMC, for the minimization of particle degradation and the improvement of reinforcement homogenization, as well as the composites' performance and microstructural stability under heating and tribological testing. These results can be useful for further research in this area using different types of matrices and reinforcements, and provides useful insights on the evaluation of MMC, as suitable candidates for mechanical applications.

Further peer-review collaborations in CNT and SPD of Ni/CNT composites

- A. Katzensteiner, **K. Aristizabal**, S. Suarez, R. Pippan, A. Bachmaier, Temperature dependent structural evolution in nickel/carbon nanotube composites processed by high-pressure torsion, in: IOP Conf. Ser. Mater. Sci. Eng., 2017. doi:10.1088/1757-899X/194/1/012019.

- J. Lee, P. Srimuk, **K. Aristizabal**, C. Kim, S. Choudhury, Y.-C. Nah, F. Mücklich, V. Presser, Pseudocapacitive Desalination of Brackish Water and Seawater with Vanadium-Pentoxide-Decorated Multiwalled Carbon Nanotubes, ChemSusChem. 10 (2017) 3611–3623. doi:10.1002/cssc.201701215.

- A. Katzensteiner, T. Müller, K. Kormout, **K. Aristizabal**, S. Suarez, R. Pippan, A. Bachmaier, Influence of Processing Parameters on the Mechanical Properties of HPT-Deformed Nickel/Carbon Nanotube Composites, Adv. Eng. Mater. 21 (2019) 1–9. doi:10.1002/adem.201800422.

References

[1]   Y.T. Zhu, T.C. Lowe, T.G. Langdon, Performance and applications of nanostructured materials produced by severe plastic deformation, Scr. Mater. 51 (2004) 825–830. doi:10.1016/j.scriptamat.2004.05.006.

[2]   M.J. Zehetbauer, R.Z. Valiev, Mechanical properties and Thermostability of Nanocrystalline Structures, in: Nanomater. by Sev. Plast. Deform., 2005: p. 597. doi:10.1002/3527602461.

[3]   A. Bachmaier, A. Hohenwarter, R. Pippan, New procedure to generate stable nanocrystallites by severe plastic deformation, Scr. Mater. 61 (2009) 1016–1019. doi:10.1016/j.scriptamat.2009.08.016.

[4]   A. Bachmaier, R. Pippan, Effect of oxide particles on the stabilization and final microstructure in aluminium, Mater. Sci. Eng. A. 528 (2011) 7589–7595. doi:10.1016/j.msea.2011.06.071.

[5]   A. Bachmaier, G.B. Rathmayr, M. Bartosik, D. Apel, Z. Zhang, R. Pippan, New insights on the formation of supersaturated solid solutions in the Cu – Cr system deformed by high-pressure torsion, Acta Mater. 69 (2014) 301–313. doi:10.1016/j.actamat.2014.02.003.

[6]   C. He, N. Zhao, C. Shi, X. Du, J. Li, H. Li, Q. Cui, An Approach to Obtaining Homogeneously Dispersed Carbon Nanotubes in Al Powders for Preparing Reinforced Al-Matrix Composites, Adv. Mater. 19 (2007) 1128–1132. doi:10.1002/adma.200601381.

[7]   T. Laha, A. Agarwal, T. Mckechnie, S. Seal, Synthesis and characterization

of plasma spray formed carbon nanotube reinforced aluminum composite, Mater. Sci. Eng. A. 381 (2004) 249–258. doi:10.1016/j.msea.2004.04.014.

[8]   T. Laha, Y. Chen, D. Lahiri, A. Agarwal, Tensile properties of carbon nanotube reinforced aluminum nanocomposite fabricated by plasma spray forming, Compos. Part A Appl. Sci. Manuf. 40 (2009) 589–594. doi:10.1016/j.compositesa.2009.02.007.

[9]   T. Kuzumaki, K. Miyazawa, H. Ichinose, K. Ito, Processing of carbon nanotube reinforced aluminum composite, J. Mater. Res. 13 (1998) 2445–2449.

[10] K. Balani, S.R. Bakshi, Y. Chen, T. Laha, A. Agarwal, Role of Powder Treatment and Carbon Nanotube Dispersion in the Fracture Toughening of Plasma-Sprayed Aluminum Oxide — Carbon Nanotube Nanocomposite, J. Nanosci. Nanotechnol. 7 (2007) 1–10. doi:10.1166/jnn.2007.851.

[11] C. Deng, X. Zhang, Y. Ma, D. Wang, Fabrication of aluminum matrix composite reinforced with carbon nanotubes, Rare Met. 26 (2007) 450–455. doi:10.1016/S1001-0521(07)60244-7.

[12] S.I. Cha, K.T. Kim, S.N. Arshad, C.B. Mo, S.H. Hong, Extraordinary Strengthening Effect of Carbon Nanotubes in Metal-Matrix Nanocomposites Processed by Molecular-Level Mixing, Adv. Mater. 17 (2005) 1377–1381. doi:10.1002/adma.200401933.

[13] M. Yu, O. Lourie, M.J. Dyer, K. Moloni, T.F. Kelly, R.S. Ruoff, Strength and Breaking Mechanism of Multiwalled Carbon Nanotubes Under Tensile Load, Science (80-.). 287 (2000) 637–640.

[14]   S.R. Dong, J.P. Tu, X.B. Zhang, An investigation of the sliding wear behavior of Cu-matrix composite reinforced by carbon nanotubes, Mater. Sci. Eng. A. 313 (2001) 83–87.

[15]   K.T. Kim, K.H. Lee, S. Il Cha, C.-B. Mo, S.H. Hong, Characterization of Carbon Nanotubes/Cu Nanocomposites Processed by Using Nano-sized Cu Powders, MRS Proc. 821 (2004). doi:10.1557/PROC-821-P3.25.

[16]   K.T. Kim, S. Il Cha, S.H. Hong, S.H. Hong, Microstructures and tensile behavior of carbon nanotube reinforced Cu matrix nanocomposites, Mater. Sci. Eng. A. 430 (2006) 27–33. doi:10.1016/j.msea.2006.04.085.

[17]   G.G. Zhao, F.M. Deng, Electroless Plating of Ni-P-CNTs Composite Coating, Key Eng. Mater. 280–283 (2007) 1445–1448. doi:10.4028/www.scientific.net/KEM.280-283.1445.

[18]   T. Chao, G. Shen, Y.T. Cheng, Comparative Study of Ni–P–Diamond and Ni–P–CNT Nanocomposite Films, J. Electrochem. Soc. 153 (2006) G98. doi:10.1149/1.2133324.

[19]   C. Chen, X. Chen, ZhiYang, W. Li, L. Xu, B. Yi, Effect of multi-walled carbon nanotubes as reinforced fibres on tribological behaviour of Ni–P electroless coatings, Diam. Relat. Mater. 15 (2006) 151–156. doi:10.1016/j.diamond.2005.09.004.

[20]   X. Chen, G. Zhang, C. Chen, L. Zhou, S. Li, X. Li, Carbon Nanotube Composite Deposits with High Hardness and High Wear Resistance, Adv. Eng. Mater. 5 (2003) 514–518. doi:10.1002/adem.200300348.

[21]   S. Suarez, F. Lasserre, F. Soldera, R. Pippan, F. Mücklich, Microstructural

thermal stability of CNT-reinforced composites processed by severe plastic deformation, Mater. Sci. Eng. A. 626 (2015) 122–127. doi:10.1016/j.msea.2014.12.065.

[22] S. Suárez, E. Ramos-Moore, B. Lechthaler, F. Mücklich, Grain growth analysis of multiwalled carbon nanotube-reinforced bulk Ni composites, Carbon N. Y. 70 (2014) 173–178. doi:10.1016/j.carbon.2013.12.089.

[23] S. Suarez, F. Lasserre, F. Mücklich, Mechanical properties of MWNT/Ni bulk composites: Influence of the microstructural refinement on the hardness, Mater. Sci. Eng. A. 587 (2013) 381–386. doi:10.1016/j.msea.2013.08.058.

[24] B.R. Pippan, F. Wetscher, M. Hafok, A. Vorhauer, The Limits of Refinement by Severe Plastic Deformation, Adv. Eng. Mater. 8 (2006) 1046–1056. doi:10.1002/adem.200600133.

[25] T. Tokunaga, K. Kaneko, Z. Horita, Production of aluminum-matrix carbon nanotube composite using high pressure torsion, Mater. Sci. Eng. A. 490 (2008) 300–304. doi:10.1016/j.msea.2008.02.022.

[26] H. Asgharzadeh, S. Joo, H.S. Kim, Consolidation of Carbon Nanotube Reinforced Aluminum Matrix Composites by High-Pressure Torsion, Metall. Mater. Trans. A. 45 (2014) 4129–4137. doi:10.1007/s11661-014-2354-6.

[27] S. Iijima, Helical microtubules of graphitic carbon, Nature. 354 (1991) 56. https://doi.org/10.1038/354056a0.

[28] H.O. Pierson, Handbook of Carbon, Graphite, Diamonds and Fullerenes,

Noyes Publications, 1993.

[29] O. V. Kharissova, B.I. Kharisov, Variations of interlayer spacing in carbon nanotubes, RSC Adv. 4 (2014) 30807–30815. doi:10.1039/c4ra04201h.

[30] J.H. Lehman, M. Terrones, E. Mansfield, K.E. Hurst, V. Meunier, Evaluating the characteristics of multiwall carbon nanotubes, Carbon N. Y. 49 (2011) 2581–2602. doi:10.1016/j.carbon.2011.03.028.

[31] P.G. Collins, Defects and disorder in carbon nanotubes, Oxford University Press, 2017. doi:10.1093/oxfordhb/9780199533053.013.2.

[32] M. Terrones, A.R. Botello-Méndez, J. Campos-Delgado, F. López-Urías, Y.I. Vega-Cantú, F.J. Rodríguez-Macías, A.L. Elías, E. Muñoz-Sandoval, A.G. Cano-Márquez, J.-C. Charlier, Graphene and graphite nanoribbons: Morphology, properties, synthesis, defects and applications, Nano Today. 5 (2010) 351–372. doi:10.1016/j.nantod.2010.06.010.

[33] N. Souza, Laser and Carbon: nanotube synthesis and annealing, Saarland University, 2017.

[34] S. Frank, P. Poncharal, Z.L. Wang, W.A. De Heer, Carbon Nanotube Quantum Resistors, Science (80-.). 280 (1988) 1744–1746. doi:10.1126/science.280.5370.1744.

[35] A. Bachtold, C. Strunk, J. Salvetat, J.-M. Bonard, L. Forró, T. Nussbaumer, C. Schönenberger, Aharonov - Bohm oscillations in carbon nanotubes, Nature. 397 (1999) 673–675.

[36] P. Kim, L. Shi, A. Majumdar, P.L. McEuen, Thermal transport measurements of individual multiwalled nanotubes, Phys. Rev. Lett. 87

(2001) 215502-1-215502–4. doi:10.1103/PhysRevLett.87.215502.

[37]   S. Berber, Y.-K. Kwon, D. Tománek, Unusually hight thermal conductivity of arbon nanotubes, Phys. Rev. Lett. 84 (2000) 4613–4616. doi:10.4324/9780203995280.

[38]   T. Ji, Y. Feng, M. Qin, W. Feng, Thermal conducting properties of aligned carbon nanotubes and their polymer composites, Compos. Part A Appl. Sci. Manuf. 91 (2016) 351–369. doi:10.1016/j.compositesa.2016.10.009.

[39]   H. Dai, J.H. Hafner, A.G. Rinzler, D.T. Colbert, R.E. Smalley, Nanotubes as nanoprobes in scanning probe microscopy, Nature. 384 (1996) 147–150. doi:10.1038/384147a0.

[40]   N. Grobert, Carbon nanotubes - becoming clean, Mater. Today. 10 (2007) 28–35. doi:10.1016/S1369-7021(06)71789-8.

[41]   M.M.J. Treacy, T.W. Ebbesen, J.M. Gibson, Exceptionally high Young's modulus observed for individual carbon nanotubes, Nature. 381 (1996) 678–680.

[42]   A. Krishnan, E. Dujardin, T.W. Ebbesen, P.N. Yianilos, M.M.J. Treacy, Young's modulus of single-walled nanotubes, Phys. Rev. B - Condens. Matter Mater. Phys. 58 (1998) 14013–14019. doi:10.1103/PhysRevB.58.14013.

[43]   E.W. Wong, P.E. Sheehan, C.M. Lieber, Nanobeam mechanics: Elasticity, strength, and toughness of nanorods and nanotubes, Science (80-.). 277 (1997) 1971–1975. doi:10.1126/science.277.5334.1971.

[44]   J.-P. Salvetat, J.-M. Bonard, N.H. Thomson, A.J. Kulik, L. Forró, W. Benoit,

L. Zuppiroli, Mechanical properties of carbon nanotubes, Appl. Phys. A Mater. Sci. Process. 69 (1999) 255–260. doi:10.1007/s003390050999.

[45]   J.-P. Salvetat, A.J. Kulik, J.-M. Bonard, G.A.D. Briggs, T. Stöckli, K. Méténier, S. Bonnamy, F. Béguin, N.A. Burnham, L. Forró, Elastic Modulus of Ordered and Disordered Multiwalled Carbon Nanotubes, Adv. Mater. 11 (1999) 161–165. doi:10.1002/(SICI)1521-4095(199902)11:2<161::AID-ADMA161>3.0.CO;2-J.

[46]   B.G. Demczyk, Y.M. Wang, J. Cumings, M. Hetman, W. Han, A. Zettl, R.O. Ritchie, Direct mechanical measurement of the tensile strength and elastic modulus of multiwalled carbon nanotubes, Mater. Sci. Eng. A. A334 (2002) 173–178.

[47]   M.M.H. Bastwros, A.M.K. Esawi, A. Wifi, Friction and wear behavior of Al-CNT composites, Wear. 307 (2013) 164–173. doi:10.1016/j.wear.2013.08.021.

[48]   U. Abdullahi, M.A. Maleque, U. Nirmal, Wear mechanisms map of CNT-Al nano-composite, Procedia Eng. 68 (2013) 736–742. doi:10.1016/j.proeng.2013.12.247.

[49]   A. Dorri Moghadam, E. Omrani, P.L. Menezes, P.K. Rohatgi, Mechanical and tribological properties of self-lubricating metal matrix nanocomposites reinforced by carbon nanotubes (CNTs) and graphene – A review, Compos. Part B Eng. 77 (2015) 402–420. doi:10.1016/j.compositesb.2015.03.014.

[50]   K. Rajkumar, S. Aravindan, Tribological studies on microwave sintered

copper-carbon nanotube composites, Wear. 270 (2011) 613–621. doi:10.1016/j.wear.2011.01.017.

[51] G. Hatipoglu, M. Kartal, M. Uysal, T. Cetinkaya, H. Akbulut, The effect of sliding speed on the wear behavior of pulse electro Co-deposited Ni/MWCNT nanocomposite coatings, Tribol. Int. 98 (2016) 59–73. doi:10.1016/j.triboint.2016.02.003.

[52] K.T. Kim, S. Il Cha, S.H. Hong, Hardness and wear resistance of carbon nanotube reinforced Cu matrix nanocomposites, Mater. Sci. Eng. A. 448–451 (2007) 46–50. doi:10.1016/j.msea.2006.02.310.

[53] S. Suárez, A. Rosenkranz, C. Gachot, F. Mücklich, Enhanced tribological properties of MWCNT/Ni bulk composites - Influence of processing on friction and wear behaviour, Carbon N. Y. 66 (2014) 164–171. doi:10.1016/j.carbon.2013.08.054.

[54] T.W. Scharf, A. Neira, J.Y. Hwang, J. Tiley, R. Banerjee, Self-lubricating carbon nanotube reinforced nickel matrix composites, J. Appl. Phys. 106 (2009). doi:10.1063/1.3158360.

[55] C. Guiderdoni, E. Pavlenko, V. Turq, A. Weibel, P. Puech, C. Estournès, A. Peigney, W. Bacsa, C. Laurent, The preparation of carbon nanotube (CNT)/copper composites and the effect of the number of CNT walls on their hardness, friction and wear properties, Carbon N. Y. 58 (2013) 185–197. doi:10.1016/j.carbon.2013.02.049.

[56] S.T. Selvamani, S. Premkumar, M. Vigneshwar, P. Hariprasath, K. Palanikumar, Influence of carbon nano tubes on mechanical, metallurgical

and tribological behavior of magnesium nanocomposites, J. Magnes. Alloy. 5 (2017) 326–335. doi:10.1016/j.jma.2017.08.006.

[57] M. Mansoor, M. Shahid, Tribological Properties of MWCNTs Strengthened Aluminum Composite Fabricated by Induction Melting, Adv. Mater. Res. 1101 (2015) 62–65. doi:10.4028/www.scientific.net/amr.1101.62.

[58] L. Reinert, S. Suárez, A. Rosenkranz, Tribo-Mechanisms of Carbon Nanotubes: Friction and Wear Behavior of CNT-Reinforced Nickel Matrix Composites and CNT-Coated Bulk Nickel, Lubricants. 4 (2016) 11. doi:10.3390/lubricants4020011.

[59] L. Reinert, F. Lasserre, C. Gachot, P. Grützmacher, T. Maclucas, N. Souza, F. Mücklich, S. Suarez, Long-lasting solid lubrication by CNT-coated patterned surfaces, Sci. Rep. (2017). doi:10.1038/srep42873.

[60] L. Reinert, Advanced self-lubricating surfaces based on carbon nanoparticles, Saarland University, 2018.

[61] T. Belin, F. Epron, Characterization methods of carbon nanotubes: A review, Mater. Sci. Eng. B Solid-State Mater. Adv. Technol. 119 (2005) 105–118. doi:10.1016/j.mseb.2005.02.046.

[62] C. V. Raman, K.S. Krishnan, A New Type of Secondary Radiation, Nature. 121 (1928) 501. https://doi.org/10.1038/121501c0.

[63] M.S. Dresselhaus, G. Dresselhaus, R. Saito, A. Jorio, Raman spectroscopy of carbon nanotubes, Phys. Rep. 409 (2005) 47. doi:10.1016/j.physrep.2004.10.006.

[64]   R.A. DiLeo, B.J. Landi, R.P. Raffaelle, Purity assessment of multiwalled carbon nanotubes by Raman spectroscopy, J. Appl. Phys. 101 (2007). doi:10.1063/1.2712152.

[65]   A. Ferrari, J. Robertson, Interpretation of Raman spectra of disordered and amorphous carbon, Phys. Rev. B - Condens. Matter Mater. Phys. 61 (2000) 14095–14107. doi:10.1103/PhysRevB.61.14095.

[66]   F. Tuinstra, J.L. Koenig, Raman Spectrum of Graphite, J. Chem. Phys. 53 (1970) 1126–1130. doi:10.1063/1.1674108.

[67]   R. Loudon, The Raman effect in crystals, Adv. Phys. 13 (1964) 423–482. doi:10.1080/00018736400101051.

[68]   S.R. Sails, D.J. Gardiner, M. Bowden, J. Savage, D. Rodway, Monitoring the quality of diamond films using Raman spectra excited at 514.5 nm and 633 nm, Diam. Relat. Mater. 5 (1996) 589–591. doi:10.1016/0925-9635(96)90031-X.

[69]   V.I. Merkulov, J.S. Lannin, C.H. Munro, S.A. Asher, V.S. Veerasamy, W.I. Milne, uv Studies of Tetrahedral Bonding in Diamondlike Amorphous Carbon, Phys. Rev. Lett. 78 (1997) 4869–4872. doi:10.1103/PhysRevLett.78.4869.

[70]   M.A. Pimenta, G. Dresselhaus, M.S. Dresselhaus, L.G. Cançado, A. Jorio, R. Saito, Studying disorder in graphite-based systems by Raman spectroscopy, Phys. Chem. Chem. Phys. 9 (2007) 1276–1290. doi:10.1039/B613962K.

[71]   N. Chawla, K.K. Chawla, Metal Matrix Composites, Springer US, 2006.

[72] D.. Miracle, S.. Donaldson, ASM Handbook volume 21 - Composites, ASM International, 2001.

[73] F.L. Matthews, R.D. Rawlings, Composite Materials, Elsevier, 1999. doi:10.1016/C2013-0-17714-8.

[74] A. Bachmaier, R. Pippan, Generation of metallic nanocomposites by severe plastic deformation, Int. Mater. Rev. 58 (2013) 41–62. doi:10.1179/1743280412Y.0000000003.

[75] R. Grierson, R.H. Krock, Techniques for Fabrication of Composite Materials, Techniques of Metals Research, Vol. VII, Interscience Publishers, 1972.

[76] A.L. Geiger, J.A. Walker, The processing and properties of discontinuously reinforced aluminum composites, JOM. 43 (1991) 8–15. doi:10.1007/BF03221097.

[77] Y. Wu, E.J. Lavernia, Spray-atomized and codeposited 6061 Al/SiCp composites, JOM. 43 (1991) 16–23. doi:10.1007/BF03221098.

[78] F. Avilés, J.V. Cauich-Rodríguez, L. Moo-Tah, A. May-Pat, R. Vargas-Coronado, Evaluation of mild acid oxidation treatments for MWCNT functionalization, Carbon N. Y. 47 (2009) 2970–2975. doi:10.1016/j.carbon.2009.06.044.

[79] S. Suárez, L. Reinert, F. Mücklich, Carbon Nanotube (CNT)-Reinforced Metal Matrix Bulk Composites: Manufacturing and Evaluation, in: Diam. Carbon Compos. Nanocomposites, InTech, 2016. doi:10.5772/63886.

[80] K.T. Kim, J. Eckert, G. Liu, J.M. Park, B.K. Lim, S.H. Hong, Influence of

embedded-carbon nanotubes on the thermal properties of copper matrix nanocomposites processed by molecular-level mixing, Scr. Mater. 64 (2011) 181–184. doi:10.1016/j.scriptamat.2010.09.039.

[81] H.J. Choi, B.H. Min, J.H. Shin, D.H. Bae, Strengthening in nanostructured 2024 aluminum alloy and its composites containing carbon nanotubes, Compos. Part A Appl. Sci. Manuf. 42 (2011) 1438–1444. doi:10.1016/j.compositesa.2011.06.008.

[82] H.J. Choi, J.H. Shin, D.H. Bae, Grain size effect on the strengthening behavior of aluminum-based composites containing multi-walled carbon nanotubes, Compos. Sci. Technol. 71 (2011) 1699–1705. doi:10.1016/j.compscitech.2011.07.013.

[83] O. Carvalho, G. Miranda, D. Soares, F.S. Silva, Carbon nanotube dispersion in aluminum matrix composites—Quantification and influence on strength, Mech. Adv. Mater. Struct. 23 (2016) 66–73. doi:10.1080/15376494.2014.929766.

[84] J. Hilding, E.A. Grulke, Z. George Zhang, F. Lockwood, Dispersion of Carbon Nanotubes in Liquids, J. Dispers. Sci. Technol. 24 (2003) 1–41. doi:10.1081/DIS-120017941.

[85] L. Reinert, M. Zeiger, S. Suárez, V. Presser, F. Mücklich, Dispersion analysis of carbon nanotubes, carbon onions, and nanodiamonds for their application as reinforcement phase in nickel metal matrix composites, RSC Adv. 5 (2015) 95149–95159. doi:10.1039/C5RA14310A.

[86] S. Suarez, F. Lasserre, O. Prat, F. Mücklich, Processing and interfacial

reaction evaluation in MWCNT/Ni composites, Phys. Status Solidi Appl. Mater. Sci. 211 (2014) 1555–1561. doi:10.1002/pssa.201431018.

[87]   S.J.L. Kang, Sintering: Densification, Grain Growth, and Microstructure, Elsevier, 2005. doi:10.1016/B978-0-7506-6385-4.X5000-6.

[88]   D.D. Phuong, P. Van Trinh, N. Van An, N. Van Luan, P.N. Minh, R.K. Khisamov, K.S. Nazarov, L.R. Zubairov, R.R. Mulyukov, A.A. Nazarov, Effects of carbon nanotube content and annealing temperature on the hardness of CNT reinforced aluminum nanocomposites processed by the high pressure torsion technique, J. Alloys Compd. 613 (2014) 68–73. doi:10.1016/j.jallcom.2014.05.219.

[89]   H. Biermann, O. Hartmann, Mechanical Behavior and Fatigue Properties of Metal-matrix Composites, in: K.U. Kainer (Ed.), Met. Matrix Compos. Cust. Mater. Automot. Aerosp. Eng., WILEY-VCH Verlag, Weinheim, 2006: p. 314.

[90]   A. Rollett, F. Humphreys, G.S. Rohrer, M. Hatherly, Recrystallization and Related Annealing Phenomena, Elsevier, 2004. doi:10.1016/B978-0-08-044164-1.X5000-2.

[91]   P.A. Manohar, M. Ferry, T. Chandra, Five Decades of the Zener Equation, ISIJ Int. 38 (1998) 913–924.

[92]   R. Armstrong, I. Codd, R.M. Douthwaite, N.J. Petch, The plastic deformation of polycrystalline aggregates, Philos. Mag. A J. Theor. Exp. Appl. Phys. 7 (1962) 45–58. doi:10.1080/14786436208201857.

[93]   Alamusi, N. Hu, B. Jia, M. Arai, C. Yan, J. Li, Y. Liu, S. Atobe, H. Fukunaga,

Prediction of thermal expansion properties of carbon nanotubes using molecular dynamics simulations, Comput. Mater. Sci. 54 (2012) 249–254. doi:10.1016/j.commatsci.2011.10.015.

[94]   K. Shirasu, G. Yamamoto, I. Tamaki, T. Ogasawara, Y. Shimamura, Y. Inoue, T. Hashida, Negative axial thermal expansion coefficient of carbon nanotubes: Experimental determination based on measurements of coefficient of thermal expansion for aligned carbon nanotube reinforced epoxy composites, Carbon N. Y. 95 (2015) 904–909. doi:10.1016/j.carbon.2015.09.026.

[95]   B. Chen, S. Li, H. Imai, L. Jia, J. Umeda, M. Takahashi, K. Kondoh, Load transfer strengthening in carbon nanotubes reinforced metal matrix composites via in-situ tensile tests, Compos. Sci. Technol. 113 (2015) 1–8. doi:10.1016/j.compscitech.2015.03.009.

[96]   S. Dong, J. Zhou, H. Liu, Y. Wu, D. Qi, The strengthening effect of carbon nanotube in metal matrix composites considering interphase, Mech. Mater. 91 (2015) 1–11. doi:10.1016/j.mechmat.2015.07.003.

[97]   B. Chen, J. Shen, X. Ye, H. Imai, J. Umeda, M. Takahashi, K. Kondoh, Solid-state interfacial reaction and load transfer efficiency in carbon nanotubes (CNTs)-reinforced aluminum matrix composites, Carbon N. Y. 114 (2017) 198–208. doi:10.1016/j.carbon.2016.12.013.

[98]   S.R. Bakshi, A. Agarwal, An analysis of the factors affecting strengthening in carbon nanotube reinforced aluminum composites, Carbon N. Y. 49 (2011) 533–544. doi:10.1016/j.carbon.2010.09.054.

[99] Z.Y. Liu, B.L. Xiao, W.G. Wang, Z.Y. Ma, Modelling of carbon nanotube dispersion and strengthening mechanisms in Al matrix composites prepared by high energy ball milling-powder metallurgy method, Compos. Part A Appl. Sci. Manuf. 94 (2017) 189–198. doi:10.1016/j.compositesa.2016.11.029.

[100] Z. Du, M.J. Tan, J.F. Guo, J. Wei, Aluminium-carbon nanotubes composites produced from friction stir processing and selective laser melting, Materwiss. Werksttech. 47 (2016) 539–548. doi:10.1002/mawe.201600530.

[101] D. Singla, K. Amulya, Q. Murtaza, CNT Reinforced Aluminium Matrix Composite-A Review, Mater. Today Proc. 2 (2015) 2886–2895. doi:10.1016/j.matpr.2015.07.248.

[102] M.T.Z. Hassan, A.M.K. Esawi, S. Metwalli, Effect of carbon nanotube damage on the mechanical properties of aluminium–carbon nanotube composites, J. Alloys Compd. 607 (2014) 215–222. doi:10.1016/j.jallcom.2014.03.174.

[103] B. Guo, M. Song, J. Yi, S. Ni, T. Shen, Y. Du, Improving the mechanical properties of carbon nanotubes reinforced pure aluminum matrix composites by achieving non-equilibrium interface, Mater. Des. 120 (2017) 56–65. doi:10.1016/j.matdes.2017.01.096.

[104] Z.W. Xue, L.D. Wang, P.T. Zhao, S.C. Xu, J.L. Qi, W.D. Fei, Microstructures and tensile behavior of carbon nanotubes reinforced Cu matrix composites with molecular-level dispersion, Mater. Des. 34 (2012) 298–301. doi:10.1016/j.matdes.2011.08.021.

[105] Z.Y. Liu, S.J. Xu, B.L. Xiao, P. Xue, W.G. Wang, Z.Y. Ma, Effect of ball-milling time on mechanical properties of carbon nanotubes reinforced aluminum matrix composites, Compos. Part A Appl. Sci. Manuf. 43 (2012) 2161–2168. doi:10.1016/j.compositesa.2012.07.026.

[106] M. Paramsothy, J. Chan, R. Kwok, M. Gupta, Addition of CNTs to enhance tensile/compressive response of magnesium alloy ZK60A, Compos. Part A Appl. Sci. Manuf. 42 (2011) 180–188. doi:10.1016/j.compositesa.2010.11.001.

[107] T. Borkar, J. Hwang, J.Y. Hwang, T.W. Scharf, J. Tiley, S.H. Hong, R. Banerjee, Strength versus ductility in carbon nanotube reinforced nickel matrix nanocomposites, J. Mater. Res. 29 (2014) 761–769. doi:10.1557/jmr.2014.53.

[108] K.S. Munir, P. Kingshott, C. Wen, Carbon Nanotube Reinforced Titanium Metal Matrix Composites Prepared by Powder Metallurgy—A Review, Crit. Rev. Solid State Mater. Sci. 40 (2015) 38–55. doi:10.1080/10408436.2014.929521.

[109] F. Ostovan, K. Matori, M. Toozandehjani, A. Oskoueian, H. Yusoff, R. Yunus, A. Mohamed Ariff, Nanomechanical Behavior of Multi-Walled Carbon Nanotubes Particulate Reinforced Aluminum Nanocomposites Prepared by Ball Milling, Materials (Basel). 9 (2016) 140. doi:10.3390/ma9030140.

[110] S.R. Bakshi, D. Lahiri, A. Agarwal, Carbon nanotube reinforced metal matrix composites - a review, Int. Mater. Rev. 55 (2010) 41–64. doi:10.1179/095066009X12572530170543.

[111] S.M. Uddin, T. Mahmud, C. Wolf, C. Glanz, I. Kolaric, C. Volkmer, H. Höller, U. Wienecke, S. Roth, H.-J. Fecht, Effect of size and shape of metal particles to improve hardness and electrical properties of carbon nanotube reinforced copper and copper alloy composites, Compos. Sci. Technol. 70 (2010) 2253–2257. doi:10.1016/j.compscitech.2010.07.012.

[112] G. Faraji, H.S. Kim, H.T. Kashi, Severe Plastic Deformation Methods, Processing and Properties, Elsevier, 2018. doi:10.1016/C2016-0-05256-7.

[113] Y. Estrin, A. Vinogradov, Extreme grain refinement by severe plastic deformation: A wealth of challenging science, Acta Mater. 61 (2013) 782–817. doi:10.1016/j.actamat.2012.10.038.

[114] V.M. Segal, Materials processing by simple shear, Mater. Sci. Eng. A. 197 (1995) 157–164. doi:10.1016/0921-5093(95)09705-8.

[115] Y. Saito, H. Utsunomiya, N. Tsuji, T. Sakai, Novel ultra-high straining process for bulk materials-development of the accumulative roll-bonding (ARB) process, Acta Mater. 47 (1999).

[116] P.W. Bridgman, Flow Phenomena in Heavily Stressed Metals, J. Appl. Phys. 8 (1937) 328–336. doi:10.1063/1.1710301.

[117] N.A. Smirnova, V.I. Levit, V.I. Pilyugin, R.I. Kuznetsov, L.S. Davydova, V.A. Sazonova, Evolution of the fcc single-crystal structure during severe plastic-deformations, Fiz. Met. I Metalloved. 61 (1986) 1170–1177.

[118] A.P. Zhilyaev, T.G. Langdon, Using high-pressure torsion for metal processing: Fundamentals and applications, Prog. Mater. Sci. 53 (2008) 893–979. doi:10.1016/j.pmatsci.2008.03.002.

[119] A.. Zhilyaev, G.. Nurislamova, B.-K. Kim, M.. Baró, J.. Szpunar, T.. Langdon, Experimental parameters influencing grain refinement and microstructural evolution during high-pressure torsion, Acta Mater. 51 (2003) 753–765. doi:10.1016/S1359-6454(02)00466-4.

[120] V. Segal, Review : Modes and Processes of Severe Plastic, Materials (Basel). 11 (2018) 1175. doi:10.3390/ma11071175.

[121] S. Ferrasse, V.M. Segal, F. Alford, S. Strothers, J. Kardokus, S. Grabmeier, J. Evans, Scale up and commercialization of ECAE sputtering products with submicrocrystalline structure., in: B.S. Altan (Ed.), Sev. Plast. Deform. Towar. Bulk Prod. Nanostructured Mater., Nova, New York, USA, 2005: pp. 585–601.

[122] V.M. Segal, P.J. Young, L.J. Kecskes, Fabrication of High-Strength Lightweight Metals for Armor and Structural Applications : Large-Scale Equal Channel Angular Extrusion Processing of Aluminum 5083 Alloy, 2017.

[123] R.Z. Valiev, T.G. Langdon, Principles of equal-channel angular pressing as a processing tool for grain refinement, Prog. Mater. Sci. 51 (2006) 881–981. doi:10.1016/j.pmatsci.2006.02.003.

[124] Y. Huang, T.G. Langdon, Advances in ultrafine-grained materials, Mater. Today. 16 (2013) 85–93. doi:10.1016/j.mattod.2013.03.004.

[125] N. Tsuji, Y. Saito, S.-H. Lee, Y. Minamino, ARB (Accumulative Roll-Bonding) and other new Techniques to Produce Bulk Ultrafine Grained Materials, Adv. Eng. Mater. 5 (2003) 338–344. doi:10.1002/adem.200310077.

[126] H.P. Stüwe, Equivalent Strains in Severe Plastic Deformation, Adv. Eng. Mater. 5 (2003) 291–295. doi:10.1002/adem.200310085.

[127] A.P. Zhilyaev, B.K. Kim, J.A. Szpunar, M.D. Bar, T.G. Langdon, The microstructural characteristics of ultrafine-grained nickel, Mater. Sci. Eng. A. 391 (2005) 377–389. doi:10.1016/j.msea.2004.09.030.

[128] R. Pippan, S. Scheriau, A. Hohenwarter, M. Hafok, Advantages and Limitations of HPT: A Review, Mater. Sci. Forum. 584–586 (2008) 16–21. doi:10.4028/www.scientific.net/MSF.584-586.16.

[129] G. Faraji, H.S. Kim, H.T. Kashi, Severe Plastic Deformation for Industrial Applications, in: G. Faraji, H.S. Kim, H.T. Kashi (Eds.), Sev. Plast. Deform., Elsevier, 2018: pp. 165–186. doi:10.1016/B978-0-12-813518-1.00005-9.

[130] K. Edalati, Z. Horita, Scaling-Up of High Pressure Torsion Using Ring Shape, Mater. Trans. 50 (2009) 92–95. doi:10.2320/matertrans.MD200822.

[131] A.E. Romanov, A.L. Kolesnikova, Application of disclination concept to solid structures, Prog. Mater. Sci. 54 (2009) 740–769. doi:10.1016/j.pmatsci.2009.03.002.

[132] L.S. Tóth, Y. Estrin, R. Lapovok, C. Gu, A model of grain fragmentation based on lattice curvature, Acta Mater. 58 (2010) 1782–1794. doi:10.1016/j.actamat.2009.11.020.

[133] O. Renk, R. Pippan, Saturation of Grain Refinement during Severe Plastic Deformation of Single Phase Materials: Reconsiderations, Current Status and Open Questions, Mater. Trans. 60 (2019) 1270–1282. doi:10.2320/matertrans.MF201918.

[134] S. Scheriau, Z. Zhang, S. Kleber, R. Pippan, Deformation mechanisms of a modified 316L austenitic steel subjected to high pressure torsion, Mater. Sci. Eng. A. 528 (2011) 2776–2786. doi:10.1016/j.msea.2010.12.023.

[135] S. Asgari, E. El-Danaf, S.R. Kalidindi, R.D. Doherty, Strain hardening regimes and microstructural evolution during large strain compression of low stacking fault energy fcc alloys that form deformation twins, Metall. Mater. Trans. A. 28 (1997) 1781–1795. doi:10.1007/s11661-997-0109-3.

[136] M. Hafok, R. Pippan, Influence of stacking fault energy and alloying on stage V hardening of HPT-deformed materials, Int. J. Mater. Res. 101 (2010) 1097–1104. doi:10.3139/146.110389.

[137] K. Edalati, D. Akama, A. Nishio, S. Lee, Y. Yonenaga, J.M. Cubero-Sesin, Z. Horita, Influence of dislocation-solute atom interactions and stacking fault energy on grain size of single-phase alloys after severe plastic deformation using high-pressure torsion, Acta Mater. 69 (2014) 68–77. doi:10.1016/j.actamat.2014.01.036.

[138] E. Bruder, P. Braun, H. ur Rehman, R.K.W. Marceau, A.S. Taylor, R. Pippan, K. Durst, Influence of solute effects on the saturation grain size and rate sensitivity in Cu-X alloys, Scr. Mater. 144 (2018) 5–8. doi:10.1016/j.scriptamat.2017.09.031.

[139] M. Hafok, R. Pippan, High-pressure torsion applied to nickel single crystals, Philos. Mag. 88 (2008) 1857–1877. doi:10.1080/14786430802337071.

[140] X.Z. Liao, A.R. Kilmametov, R.Z. Valiev, H. Gao, X. Li, A.K. Mukherjee, J.F.

Bingert, Y.T. Zhu, High-pressure torsion-induced grain growth in electrodeposited nanocrystalline Ni, Appl. Phys. Lett. 88 (2006) 021909. doi:10.1063/1.2159088.

[141]   B. Yang, H. Vehoff, A. Hohenwarter, M. Hafok, R. Pippan, Strain effects on the coarsening and softening of electrodeposited nanocrystalline Ni subjected to high pressure torsion, Scr. Mater. 58 (2008) 790–793. doi:10.1016/j.scriptamat.2007.12.039.

[142]   S. Ni, Y.B. Wang, X.Z. Liao, S.N. Alhajeri, H.Q. Li, Y.H. Zhao, E.J. Lavernia, S.P. Ringer, T.G. Langdon, Y.T. Zhu, Grain growth and dislocation density evolution in a nanocrystalline Ni–Fe alloy induced by high-pressure torsion, Scr. Mater. 64 (2011) 327–330. doi:10.1016/j.scriptamat.2010.10.027.

[143]   R. Pippan, S. Scheriau, A. Taylor, M. Hafok, A. Hohenwarter, A. Bachmaier, Saturation of Fragmentation During Severe Plastic Deformation, Annu. Rev. Mater. Res. 40 (2010) 319–343. doi:10.1146/annurev-matsci-070909-104445.

[144]   A. Vorhauer, R. Pippan, On the Onset of a Steady State in Body-Centered Cubic Iron during Severe Plastic Deformation at Low Homologous Temperatures, Metall. Mater. Trans. A. 39 (2008) 417–429. doi:10.1007/s11661-007-9413-1.

[145]   M.J. Starink, Dislocation versus grain boundary strengthening in SPD processed metals: Non-causal relation between grain size and strength of deformed polycrystals, Mater. Sci. Eng. A. 705 (2017) 42–45.

doi:10.1016/j.msea.2017.08.069.

[146] C.J. Youngdahl, P.G. Sanders, J.A. Eastman, J.R. Weertman, Compressive yield strengths of nanocrystalline Cu and Pd, Scr. Mater. 37 (1997) 809–813. doi:10.1016/S1359-6462(97)00157-7.

[147] P. Zhang, S.X. Li, Z.F. Zhang, General relationship between strength and hardness, Mater. Sci. Eng. A. 529 (2011) 62–73. doi:10.1016/j.msea.2011.08.061.

[148] M.A. Meyers, A. Mishra, D.J. Benson, Mechanical properties of nanocrystalline materials, Prog. Mater. Sci. 51 (2006) 427–556. doi:10.1016/j.pmatsci.2005.08.003.

[149] C. Koch, Optimization of strength and ductility in nanocrystalline and ultrafine grained metals, Scr. Mater. 49 (2003) 657–662. doi:10.1016/S1359-6462(03)00394-4.

[150] R.Z. Valiev, I. V. Alexandrov, Y.T. Zhu, T.C. Lowe, Paradox of Strength and Ductility in Metals Processed Bysevere Plastic Deformation, J. Mater. Res. 17 (2002) 5–8. doi:10.1557/JMR.2002.0002.

[151] I.A. Ovid, R.Z. Valiev, Y.T. Zhu, Review on superior strength and enhanced ductility of metallic nanomaterials, Prog. Mater. Sci. 94 (2018) 462–540. doi:10.1016/j.pmatsci.2018.02.002.

[152] C.E. Carlton, P.J. Ferreira, What is behind the inverse Hall–Petch effect in nanocrystalline materials?, Acta Mater. 55 (2007) 3749–3756. doi:10.1016/j.actamat.2007.02.021.

[153] C.A. Schuh, T.G. Nieh, H. Iwasaki, The effect of solid solution W additions

on the mechanical properties of nanocrystalline Ni, Acta Mater. 51 (2003) 431–443. doi:10.1016/S1359-6454(02)00427-5.

[154] E.N. Hahn, M.A. Meyers, Grain-size dependent mechanical behavior of nanocrystalline metals, Mater. Sci. Eng. A. 646 (2015) 101–134. doi:10.1016/j.msea.2015.07.075.

[155] H. Zhang, D. Du, D.J. Srolovitz, Effects of boundary inclination and boundary type on shear-driven grain boundary migration, Philos. Mag. 88 (2008) 243–256. doi:10.1080/14786430701810764.

[156] J.C.M. Li, Grain boundary impurity and porosity effects on the yield strength of nanocrystalline materials, Appl. Phys. Lett. 90 (2007) 041912. doi:10.1063/1.2430491.

[157] X.L. Wu, Y.T. Zhu, Y.G. Wei, Q. Wei, Strong Strain Hardening in Nanocrystalline Nickel, Phys. Rev. Lett. 103 (2009) 205504. doi:10.1103/PhysRevLett.103.205504.

[158] L. Wang, J. Teng, P. Liu, A. Hirata, E. Ma, Z. Zhang, M. Chen, X. Han, Grain rotation mediated by grain boundary dislocations in nanocrystalline platinum, Nat. Commun. 5 (2014) 4402. doi:10.1038/ncomms5402.

[159] J.R. Greer, J.T.M. De Hosson, Plasticity in small-sized metallic systems: Intrinsic versus extrinsic size effect, Prog. Mater. Sci. 56 (2011) 654–724. doi:10.1016/j.pmatsci.2011.01.005.

[160] A.J. Barnes, Superplastic Forming 40 Years and Still Growing, J. Mater. Eng. Perform. 16 (2007) 440–454. doi:10.1007/s11665-007-9076-5.

[161] A. Sergueeva, A. Mukherjee, Superplastic deformation in nanocrystalline

metals and alloys, in: Nanostructured Met. Alloy. Process. Microstruct. Mech. Prop. Appl., 2011: pp. 542–593. doi:10.1533/9780857091123.3.542.

[162] T.G. Langdon, Seventy-five years of superplasticity: historic developments and new opportunities, J. Mater. Sci. 44 (2009) 5998–6010. doi:10.1007/s10853-009-3780-5.

[163] R.Z. Valiev, R.K. Islamgaliev, I. V. Alexandrov, Bulk nanostructured materials from severe plastic deformation, Prog. Mater. Sci. 45 (2000) 103–189. doi:10.1016/S0079-6425(99)00007-9.

[164] R.Z. Valiev, Structure and mechanical properties of ultrafine-grained metals, Mater. Sci. Eng. 234–236 (1997) 59–66. doi:https://doi.org/10.1016/S0921-5093(97)00183-4.

[165] A. Bachmaier, C. Motz, On the remarkable thermal stability of nanocrystalline cobalt via alloying, Mater. Sci. Eng. A. 624 (2015) 41–51. doi:10.1016/j.msea.2014.11.062.

[166] M. Kawasaki, T.G. Langdon, Review: achieving superplasticity in metals processed by high-pressure torsion, J. Mater. Sci. 49 (2014) 6487–6496. doi:10.1007/s10853-014-8204-5.

[167] P. Scherrer, Bestimmung der Größe und der inneren Struktur von Kolloidteilchen mittels Röntgenstrahlen, Nachrichten von Der Gesellschaft Der Wissenschaften Zu Göttingen, Math. Klasse. (1918) 98–100. http://resolver.sub.uni-goettingen.de/purl?GDZPPN002505045.

[168] B.E. Warren, B.L. Averbach, The effect of cold-work distortion on x-ray patterns, J. Appl. Phys. 21 (1950) 595–599. doi:10.1063/1.1699713.

[169] G.K. Williamson, W.H. Hall, X-ray line broadening from filed aluminium and wolfram, Acta Metall. 1 (1953) 22–31. doi:10.1016/0001-6160(53)90006-6.

[170] J. Gubicza, N.H. Nam, L. Balogh, R.J. Hellmig, V. V. Stolyarov, Y. Estrin, T. Ungár, Microstructure of severely deformed metals determined by X-ray peak profile analysis, J. Alloys Compd. 378 (2004) 248–252. doi:10.1016/j.jallcom.2003.11.162.

[171] T. Ungár, I. Dragomir, Á. Révész, A. Borbély, The contrast factors of dislocations in cubic crystals: The dislocation model of strain anisotropy in practice, J. Appl. Crystallogr. 32 (1999) 992–1002. doi:10.1107/S0021889899009334.

[172] T. Ungár, J. Gubicza, P. Hanák, I. Alexandrov, Densities and character of dislocations and size-distribution of subgrains in deformed metals by X-ray diffraction profile analysis, Mater. Sci. Eng. A. 319–321 (2001) 274–278. doi:10.1016/S0921-5093(01)01025-5.

[173] G.K. Williamson, R.E. Smallman, III. Dislocation densities in some annealed and cold-worked metals from measurements on the X-ray Debye-Scherrer spectrum, Philos. Mag. 1 (1956) 34–46. doi:10.1080/14786435608238074.

[174] Z. Yang, U. Welzel, Microstructure-microhardness relation of nanostructured Ni produced by high-pressure torsion, Mater. Lett. 59 (2005) 3406–3409. doi:10.1016/j.matlet.2005.05.077.

[175] A.R. Kil'mametov, R.Z. Valiev, R.K. Islamgaliev, G. V Nurislamova,

Structural features of nanocrystalline nickel subjected to high-pressure torsion, Phys. Met. Metallogr. 101 (2006) 75–82. doi:10.1134/s0031918x06010108.

[176] P. Scardi, M. Leoni, Whole powder pattern modelling, Acta Crystallogr. Sect. A Found. Crystallogr. 58 (2002) 190–200. doi:10.1107/S0108767301021298.

[177] N. Gao, M.J. Starink, T.G. Langdon, Using differential scanning calorimetry as an analytical tool for ultrafine grained metals processed by severe plastic deformation, Mater. Sci. Technol. 25 (2009) 687–698. doi:10.1179/174328409X408901.

[178] D. Setman, E. Schafler, E. Korznikova, M.J. Zehetbauer, The presence and nature of vacancy type defects in nanometals detained by severe plastic deformation, Mater. Sci. Eng. A. 493 (2008) 116–122. doi:10.1016/j.msea.2007.06.093.

[179] M.B. Bever, D.L. Holt, A.L. Titchener, The stored energy of cold work, Prog. Mater. Sci. 17 (1973) 5–177. doi:10.1016/0079-6425(73)90001-7.

[180] H.E. Kissinger, Reaction Kinetics in Differential Thermal Analysis, Anal. Chem. 29 (1957) 1702–1706. doi:10.1021/ac60131a045.

[181] J. Gubicza, Thermal Stability of Defect Structures in Nanomaterials, in: Defect Struct. Prop. Nanomater., Elsevier, 2017: pp. 317–371. doi:10.1016/B978-0-08-101917-7.00012-8.

[182] H. Li, A. Misra, Z. Horita, C.C. Koch, N.A. Mara, P.O. Dickerson, Y. Zhu, Strong and ductile nanostructured Cu-carbon nanotube composite, Appl.

Phys. Lett. 95 (2009) 071907. doi:10.1063/1.3211921.

[183] H. Li, A. Misra, Y. Zhu, Z. Horita, C.C. Koch, T.G. Holesinger, Processing and characterization of nanostructured Cu-carbon nanotube composites, Mater. Sci. Eng. A. 523 (2009) 60–64. doi:10.1016/j.msea.2009.05.031.

[184] P. Jenei, E.Y. Yoon, J. Gubicza, H.S. Kim, J.L. Lábár, T. Ungár, Microstructure and hardness of copper–carbon nanotube composites consolidated by High Pressure Torsion, Mater. Sci. Eng. A. 528 (2011) 4690–4695. doi:10.1016/j.msea.2011.02.066.

[185] P. Quang, Y.G. Jeong, S.C. Yoon, S.H. Hong, H.S. Kim, Consolidation of 1vol.% carbon nanotube reinforced metal matrix nanocomposites via equal channel angular pressing, J. Mater. Process. Technol. 187–188 (2007) 318–320. doi:10.1016/j.jmatprotec.2006.11.116.

[186] Q. Pham, Y.G. Jeong, S.C. Yoon, S.I. Hong, S.H. Hong, H.S. Kim, Carbon Nanotube Reinforced Metal Matrix Nanocomposites via Equal Channel Angular Pressing, Mater. Sci. Forum. 534–536 (2007) 245–248. doi:10.4028/www.scientific.net/MSF.534-536.245.

[187] J. Nguyen, T.B. Holland, H. Wen, M. Fraga, A. Mukherjee, E. Lavernia, Mechanical behavior of ultrafine-grained Ni-carbon nanotube composite, J. Mater. Sci. 49 (2014) 2070–2077. doi:10.1007/s10853-013-7897-1.

[188] A. Katzensteiner, K. Aristizabal, S. Suarez, R. Pippan, A. Bachmaier, Temperature dependent structural evolution in nickel/carbon nanotube composites processed by high-pressure torsion, in: IOP Conf. Ser. Mater. Sci. Eng., 2017. doi:10.1088/1757-899X/194/1/012019.

[189] A. Katzensteiner, T. Müller, K. Kormout, K. Aristizabal, S. Suarez, R. Pippan, A. Bachmaier, Influence of Processing Parameters on the Mechanical Properties of HPT-Deformed Nickel/Carbon Nanotube Composites, Adv. Eng. Mater. 21 (2019) 1–9. doi:10.1002/adem.201800422.

[190] P. Jenei, J. Gubicza, E.Y. Yoon, H.S. Kim, J.L. Lábár, High temperature thermal stability of pure copper and copper-carbon nanotube composites consolidated by High Pressure Torsion, Compos. Part A Appl. Sci. Manuf. 51 (2013) 71–79. doi:10.1016/j.compositesa.2013.04.007.

[191] H.J. Choi, S.J. Nam, J. Hofstetter, T. Buonassisi, D.H. Bae, High-temperature diffusion processes in ultrafine-grained aluminum and its composites containing multi-walled carbon nanotubes, J. Compos. Mater. 49 (2015) 2705–2711. doi:10.1177/0021998314554118.

[192] E. Darmiani, I. Danaee, M.A. Golozar, M.R. Toroghinejad, A. Ashrafi, A. Ahmadi, Reciprocating wear resistance of Al-SiC nano-composite fabricated by accumulative roll bonding process, Mater. Des. 50 (2013) 497–502. doi:10.1016/j.matdes.2013.03.047.

[193] K. Edalati, M. Ashida, Z. Horita, T. Matsui, H. Kato, Wear resistance and tribological features of pure aluminum and Al-Al2O3 composites consolidated by high-pressure torsion, Wear. 310 (2014) 83–89. doi:10.1016/j.wear.2013.12.022.

[194] M.Y. Gutkin, Elastic and plastic deformation in nanocrystalline metals, Nanostructured Met. Alloy. Process. Microstruct. Mech. Prop. Appl. (2011) 329–374. doi:10.1533/9780857091123.3.329.

[195] F. Mokdad, D.L. Chen, Z.Y. Liu, B.L. Xiao, D.R. Ni, Z.Y. Ma, Deformation and strengthening mechanisms of a carbon nanotube reinforced aluminum composite, Carbon N. Y. 104 (2016) 64–77. doi:10.1016/j.carbon.2016.03.038.

[196] B. Chen, J. Shen, X. Ye, L. Jia, S. Li, J. Umeda, M. Takahashi, K. Kondoh, Length effect of carbon nanotubes on the strengthening mechanisms in metal matrix composites, Acta Mater. 140 (2017) 317–325. doi:10.1016/j.actamat.2017.08.048.

[197] S. Dong, J. Zhou, D. Hui, Y. Wang, S. Zhang, Size dependent strengthening mechanisms in carbon nanotube reinforced metal matrix composites, Compos. Part A Appl. Sci. Manuf. 68 (2015) 356–364. doi:10.1016/j.compositesa.2014.10.018.

[198] A. Agarwal, S.R. Bakshi, D. Lahiri, Carbon Nanotubes reinforced metal matrix composites, CRC Press, Taylor and Francis, 2011.

List of Figures